

**Surface Modification by Filtered Cathodic Vacuum Arc  
and Nanomechanical Properties of Thin-Film Media, Cu-Al-Ni Shape-  
Memory Alloy, and Surface-Textured Silicon**

by

Hanshen Zhang

B.Eng. (City University of Hong Kong) 2003  
M.S. (University of California, Berkeley) 2005

A dissertation submitted in partial satisfaction of the  
requirements for the degree of

Doctor of Philosophy

in

Engineering-Mechanical Engineering

in the

Graduate Division

of the

UNIVERSITY of CALIFORNIA, BERKELEY

Committee in charge:

Professor Kyriakos Komvopoulos, Chair  
Professor Lisa A. Pruitt  
Professor Robert O. Ritchie

Fall 2009

The dissertation of Hanshen Zhang is approved:

---

Professor Kyriakos Komvopoulos, Chair

Date

---

Professor Lisa A. Pruitt

Date

---

Professor Robert O. Ritchie

Date

University of California, Berkeley

Surface Modification by Filtered Cathodic Vacuum Arc  
and Nanomechanical Properties of Thin-Film Media, Cu-Al-Ni Shape-  
Memory Alloy, and Surface-Textured Silicon

©2009

by Hanshen Zhang

## **ABSTRACT**

### **Surface Modification by Filtered Cathodic Vacuum Arc and Nanomechanical Properties of Thin-Film Media, Cu-Al-Ni Shape- Memory Alloy, and Surface-Textured Silicon**

by

Hanshen Zhang

Doctor of Philosophy in Engineering-Mechanical Engineering

University of California, Berkeley

Professor Kyriakos Komvopoulos, Chair

The objective of this dissertation was twofold: (1) investigation of the effects of different surface modifications on the surface microstructure, nanomechanical properties and friction characteristics of silicon and a cobalt-based alloy, and (2) analysis of the pseudoelastic behavior of a shape-memory alloy due to cyclic nanoindentation loading.

Filtered cathodic vacuum arc (FCVA) is a novel film deposition method in which the film precursors are energetic ions, as opposed to neutral atoms or clusters of atoms in traditional deposition techniques like sputtering and chemical vapor deposition. FCVA exhibits two important advantages, i.e., the flow direction and energy of the film precursors can be independently controlled by magnetic and electrical fields, respectively, and the absence of a working gas enables film deposition over a wide temperature range. However, there are also important challenges in FCVA treatments, such as arcing spot instabilities and plasma fluctuations.

A customer-made direct-current FCVA system is presented in this dissertation that uses a special magnetic-field mechanism to stabilize the plasma. The effectiveness of this FCVA system to produce high-quality films is examined in the context of results of the microstructure and nanomechanical properties of amorphous carbon films synthesized under different FCVA deposition conditions. The ion implantation mechanism and surface treatment of the FCVA system were investigated both theoretically and experimentally. Single-crystal silicon and a cobalt-based alloy (magnetic recording media) were modified by FCVA treatments. Silicon has many applications in the semiconductor industry and micro-electro-mechanical systems (MEMS), while cobalt-based alloy is the magnetic recording medium of hard disks. The present FCVA system was used to form an ultrathin overcoat on silicon and an overcoat-free magnetic medium with its surface modified by the FCVA technique to enhance the surface corrosion and wear resistance. Particular attention was given to the surface chemistry, morphology, and nanomechanical properties of the FCVA-treated surfaces.

A second main objective of this dissertation was the investigation of the microstructure and nanomechanical properties of a Cu-Al-Ni shape-memory alloy, known as the shape-memory alloy with the largest reversible strain (~17%). Transmission electron microscopy (TEM) and Rutherford backscattering spectroscopy (RBS) studies were carried out to study the microstructure of this alloy. The pseudoelastic behavior of Cu-Al-Ni at the nanoscale was demonstrated by cyclic nanoindentation experiments. This behavior is associated with the stabilization of the martensite phase with the increase of the indentation cycles.

Nanoscale surface topography modification of silicon by ion beam bombardment was also investigated in this dissertation. Nanoindentation and nanoscratching tests performed with diamond tips of radius close to the size of the surface features (ripples) produced by ion-beam texturing revealed scale-dependent nanomechanical properties and anisotropic friction behavior.

---

Professor Kyriakos Komvopoulos  
Dissertation Committee Chair

# TABLE OF CONTENTS

TABLE OF CONTENTS.....	i
LIST OF FIGURES.....	iii
ACKNOWLEDGEMENT.....	vii
Chapter 1 Filtered Cathodic Vacuum Arc System.....	1
1.1 Cathodic Vacuum Arc Discharging.....	1
1.1.1 Cathodic Vacuum Arc Discharging Mechanism.....	1
1.1.2 Two Modes of FCVA.....	2
1.2 Implementation of a ‘Cusp-Configuration’ of Magnetic Field For Direct-Current (DC) Plasma Stabilization.....	3
1.3 Substrate Bias Effect and Ion Implantation.....	6
Chapter 2 Amorphous Carbon Films Deposited by FCVA.....	9
2.1 Carbon Film Deposition by DC FCVA.....	9
2.2 Characterization of FCVA Deposited Carbon Films.....	11
2.2.1 Microanalysis.....	11
2.2.2 Mechanical Testing.....	16
2.3 Summary.....	19
Chapter 3 FCVA Treatment of Silicon Surfaces.....	20
3.1 Subplantation Mechanism of Energetic Carbon Ion Bombardment.....	21
3.1.1 T-DYN Simulations of Ion Implantation.....	21
3.1.2 FCVA Deposition of Ultrathin Carbon Films.....	24
3.2 Chemical Bonding Analysis by X-Ray Photoelectron Spectroscopy (XPS).....	26
3.3 Surface Roughness Evolution Due To FCVA Treatment.....	30
3.4 Nanomechanical Properties of the FCVA-Treated Silicon Surfaces.....	32
3.5 Summary.....	35
Chapter 4 FCVA Treatment of the Magnetic Medium Surface.....	36
4.1 Overcoat-Free Magnetic Medium for Ultrahigh Magnetic Recording.....	36
4.2 Sputter-Etching of Preexisting Carbon Overcoat.....	37
4.3 FCVA Treatment of the Magnetic Medium.....	39
4.4 Surface Chemical Analysis of the FCVA-Treated Magnetic Medium.....	42
4.4.1 Oxidization Behavior.....	42
4.4.2 Carbon Bonding Evolution With Treatment Time.....	43
4.5 Surface Roughness of FCVA-Treated Magnetic Medium.....	46
4.6 Nanomechanical Properties of FCVA-Treated Magnetic Medium.....	47
Chapter 5 Nanomechanical Response of Single-Crystal Cu-Al-Ni Shape-Memory Alloy.....	51
5.1 Phase Transformation Scheme of Cu-Al-Ni Shape-Memory Alloy.....	51
5.2 Processing and Characterization of Single-Crystal Cu-Al-Ni Shape-Memory Alloy.....	52
5.2.1 Fabrication of Specimens.....	52
5.2.2 Chemical Composition Analysis by Rutherford Backscattering and Particle-Induced X-ray Emission.....	53

5.2.3	Microstructure Characterization by Transmission Electron Microscopy (TEM).....	54
5.3	Nanoscale Pseudoelasticity Due to Cyclic Indentation.....	58
5.3.1	Reference Tensile Test.....	58
5.3.2	Correlation of Macroscale and Nanoscale Deformation Behaviors.....	59
Chapter 6	Scale-Dependent Nanomechanical Behavior and Anisotropic Friction of Nanotextured Silicon Surfaces.....	66
6.1	Ion Beam-Assisted Surface Nanotexturing.....	67
6.2	Scale-Dependent Nanomechanical Properties of Nanotextured Silicon Surfaces.....	69
6.3	Anisotropic Friction Behavior.....	71
Chapter 7	Conclusions.....	75
	BIBLIOGRAPHY.....	79

## LIST OF FIGURES

Figure 1.1 Schematics of (a) top and (b) front view of the FCVA system. Four raster coils attached to the outside of the downstream coil (not shown for clarity) are used to direct the plasma toward the substrate holder.....	4
Figure 1.2 Schematic of the plasma stabilizing mechanism during dc arc discharge. The magnetic field lines produced by the cathode coil and the upstream coil are shown only at the left side of the coil cross section. The opposite directions of the magnetic fields of the two coils generate a “cusp” configuration in the magnetic field around the anode that maintains a stable arc current flow during the dc arc discharge.....	5
Figure 1.3 Waveform of pulsed substrate bias of –100 V time-average magnitude and 25 kHz frequency.....	7
Figure 2.1 XRD spectrum of film A synthesized under zero substrate bias. ....	11
Figure 2.2 RBS spectra of <i>a</i> -C films synthesized under (a) zero substrate bias (film A) and (b) –100 V time-average magnitude and 25 kHz frequency pulsed substrate bias (film B). The RBS spectrum of bare Si is also shown in each plot for comparison. The C and Si edge positions are shown in (a), and the shift of the Si edge position due to the <i>a</i> -C film is shown in (b).....	12
Figure 2.3 Raman spectra of <i>a</i> -C films synthesized under (a) zero substrate bias (film A) and (b) –100 V time-average magnitude and 25 kHz frequency pulsed substrate bias (film B). The spectra were acquired after performing linear background subtraction.....	14
Figure 2.4 C1s XPS spectra (black curves) of <i>a</i> -C films synthesized under (a) zero substrate bias (film A) and (b) –100 V time-average magnitude and 25 kHz frequency pulsed substrate bias (film B) with fits (red curves) obtained from six Gaussian distributions (green curves). The spectra were acquired after performing inelastic background subtraction.....	15
Figure 2.5 Nanoindentation curves of <i>a</i> -C films synthesized under (a) zero substrate bias (film A) and (b) –100 V time-average magnitude and 25 kHz frequency pulsed substrate bias (film B) for a maximum load of 150 μN and loading/unloading times equal to 2 s.....	17
Figure 2.6 Maximum contact pressure and reduced modulus of <i>a</i> -C films synthesized under (a) zero substrate bias (film A) and (b) –100 V time-average magnitude and 25 kHz frequency pulsed substrate bias (film B).....	18
Figure 3.1 Carbon depth profiles simulated with the T-DYN code for 120 eV kinetic energy of carbon ions impinging perpendicular to a silicon substrate surface.....	22
Figure 3.2 Carbon depth profiles simulated with the T-DYN code for 20–320 eV kinetic energy of carbon ions impinging perpendicular to a silicon substrate surface and carbon ion fluence equal to (a) $3.6 \times 10^{16}$ and (b) $1.8 \times 10^{16}$ ions/cm <sup>2</sup> corresponding to 0.4 and 0.2 min process time.....	23

Figure 3.3 XRR results for 0.2–3 min process time, ~120 eV carbon ion kinetic energy (–100 V bias voltage of 25 kHz frequency) and $\sim 1.48 \times 10^{15}$ ions/cm <sup>2</sup> ·s ion flux.....	25
Figure 3.4 C1s XPS spectrum of C1s core level peak for ~170 eV carbon ion kinetic energy (–150 V bias voltage of 25 kHz frequency) and 0.4 min process time ( $3.6 \times 10^{16}$ ions/cm <sup>2</sup> ion fluence). The spectrum was fitted by six Gaussian curves after inelastic background subtraction.....	27
Figure 3.5 (a) Binding energies of characteristic Gaussian fits of C1s core level peak and (b) fraction of carbon constituents of deconvoluted C1s core level peak vs process time for ~120 eV carbon ion kinetic energy (–100 V bias voltage of 25 kHz frequency).....	28
Figure 3.6 Carbon constituents of deconvoluted C1s core level peak vs substrate bias voltage of 25 kHz frequency for (a) 0.4 and (b) 0.2 min process time corresponding to $3.6$ and $1.8 \times 10^{16}$ ions/cm <sup>2</sup> ion fluence.....	29
Figure 3.7 (a) Surface roughness vs process time for ~120 eV ion kinetic energy (–100 V bias voltage of 25 kHz frequency) and (b) surface roughness vs substrate bias voltage of 25 kHz frequency for 0.4 and 0.2 min process time corresponding to $3.6$ and $1.8 \times 10^{16}$ ions/cm <sup>2</sup> ion fluence. The zero-time data point in (a) corresponds to the roughness of the Ar <sup>+</sup> sputter-cleaned Si(100) substrate surface.....	31
Figure 3.8 (a) Representative nanoindentation curve and (b) maximum contact pressure vs maximum displacement for a sample processed at ~120 eV ion kinetic energy (–100 V bias voltage of 25 kHz frequency) and 3 min process time.....	33
Figure 3.9 (a) Effective hardness vs process time for ~120 eV ion kinetic energy (–100 V bias voltage of 25 kHz frequency), and (b) effective hardness vs substrate bias voltage of 25 kHz frequency for 0.4 and 0.2 min process time corresponding to $3.6$ and $1.8 \times 10^{16}$ ions/cm <sup>2</sup> ion fluence.....	34
Figure 4.1 T-DYN simulation of etch thickness of graphitic carbon vs incidence angle of Ar <sup>+</sup> ion beam (ion energy = 500 eV; ion dose = $1 \times 10^{16}$ ions/cm <sup>2</sup> ).....	38
Figure 4.2 XPS spectrum of a hard-disk specimen with a ~4-nm-thick carbon overcoat obtained (a) before and (b) after sputter etching for 8 min with an Ar <sup>+</sup> ion beam at a 60° incidence angle.....	39
Figure 4.3 Carbon depth profiles due to C <sup>+</sup> ion impingement perpendicular to a cobalt surface simulated with the T-DYN code for (a) 0 and (b) –100 V/25 kHz pulse frequency substrate bias (ion flux $\approx 1.5 \times 10^{15}$ ions/cm <sup>2</sup> ·s).....	40
Figure 4.4 Surface elevation determined from surface profilometry measurements vs treatment time (substrate bias = 0 and –100 V/25 kHz pulse frequency; ion flux $\approx 1.5 \times 10^{15}$ ions/cm <sup>2</sup> ·s).....	41

Figure 4.5 Co2p XPS spectra of magnetic medium obtained (a) before and (b) after FCVA treatment (substrate bias = 0 V; ion flux $\approx 1.5 \times 10^{15}$ ions/cm <sup>2</sup> ·s; treatment time = 6 s).....	42
Figure 4.6 C1s XPS spectrum of FCVA-treated magnetic medium (substrate bias = 0 V; ion flux $\approx 1.5 \times 10^{15}$ ions/cm <sup>2</sup> ·s; treatment time = 12 s). After inelastic background subtraction, the spectrum was fitted with six Gaussian distributions at characteristic binding energies.....	43
Figure 4.7 Binding energies of $sp^1$ , $sp^2$ , and $sp^3$ Gaussian fits to C1s XPS spectra vs treatment time for (a) 0 and (b) -100 V/25 kHz pulse frequency substrate bias (ion flux $\approx 1.5 \times 10^{15}$ ions/cm <sup>2</sup> ·s).....	44
Figure 4.8 Fractions of carbon constituents obtained from the deconvoluted C1s XPS spectra vs treatment time for (a) 0 and (b) -100 V/25 kHz pulse frequency substrate bias (ion flux $\approx 1.5 \times 10^{15}$ ions/cm <sup>2</sup> ·s).....	45
Figure 4.9 Surface roughness vs treatment time (substrate bias = 0 and -100 V/25 kHz pulse frequency; ion flux $\approx 1.5 \times 10^{15}$ ions/cm <sup>2</sup> ·s).....	47
Figure 4.10 (a) Nanoindentation load vs displacement response and (b) maximum contact pressure and reduced modulus vs maximum displacement of FCVA-treated magnetic medium (substrate bias = 0 V; ion flux $\approx 1.5 \times 10^{15}$ ions/cm <sup>2</sup> ·s; treatment time = 48 s).....	48
Figure 4.11 (a) Effective hardness, (b) reduced modulus, and (c) effective depth vs treatment time of FCVA-treated magnetic medium (substrate bias = 0 and -100 V/25 kHz pulse frequency; ion flux $\approx 1.5 \times 10^{15}$ ions/cm <sup>2</sup> ·s).....	50
Figure 5.1 (a) PIXE and (b) RBS spectra of single-crystal Cu-Al-Ni alloy.....	54
Figure 5.2 TEM selected area diffraction patterns for zone axis (a) [001], (b) [03 $\bar{1}$ ], (c) [0 $\bar{2}$ 1], and (d) [011].....	55
Figure 5.3 (a) Dark-field TEM image obtained under two-beam condition of [011] zone axis and (1 $\bar{1}$ 1) imaging beam showing antiphase boundaries with different patterns, (b) bright-field TEM image obtained by tilting the sample from the [011] zone axis to the (400) plane axis showing closed-loop antiphase boundaries and strain modulation manifested by a tweed microstructure, and (c) dark-field TEM image from the [011] zone axis to the (400) plane axis showing the tweed microstructure.....	57
Figure 5.4 Stress-strain response of single-crystal Cu-Al-Ni alloy at -30°C produced from cyclic tensile loading. The first cycle consists of loading up to point A and then unloading to point B. All three consecutive loading cycles begin and end at point B, attaining their corresponding maximum stresses at points D, E and F. These cycles demonstrate the occurrence of a stable pseudoelastic behavior after the first cycle (training period). The arrows indicate the loading and unloading paths of each stress-strain cycle.....	59

Figure 5.5 Nanoindentation curves of single-crystal Cu-Al-Ni alloy at room temperature illustrating a stable pseudoelastic behavior after three nanoindentation cycles (training period) for a maximum load of 150 $\mu\text{N}$ .....	60
Figure 5.6 Stress-strain responses of single-crystal Cu-Al-Ni alloy at room temperature derived from cyclic nanoindentation results: (a) first-cycle response for a maximum load of 100 and 450 $\mu\text{N}$ revealing changes in the dominant deformation mechanism(s) and (b) stress-strain hysteresis of the stable pseudoelastic behavior obtained after six nanoindentation cycles (training period) for a maximum load of 450 $\mu\text{N}$ . The arrows indicate the loading and unloading paths of each stress-strain cycle.....	62
Figure 6.1 AFM image ( $1 \times 1 \mu\text{m}^2$ ) of the topography of a Si(100) surface nanotextured by oblique $\text{Ar}^+$ ion beam bombardment revealing the formation of dense arrays of periodically ordered ripples.....	68
Figure 6.2 Nanoindentation responses of (a) nanotextured and (b) original (untextured) silicon surface for tip radius $R \approx 1$ and 20 $\mu\text{m}$ .....	70
Figure 6.3 Friction coefficient due to sliding of a diamond tip parallel ( $r_{\parallel}$ ) and perpendicular ( $r_{\perp}$ ) to the main ripple direction of a nanotextured silicon surface for tip radius (a) $R \approx 1 \mu\text{m}$ and (b) $R \approx 20 \mu\text{m}$ .....	72

## ACKNOWLEDGEMENT

Pursuing Ph.D studies at University of California, Berkeley over the past six years has been the most memorable and significant experience in my life. I am deeply indebted to many people who have guided, helped and supported me along this arduous but incredibly far-reaching journey.

My foremost gratitude and appreciation go to my Ph.D advisor Professor K. Komvopoulos, for being a constant source of inspiration and encouragement. What I learnt from him was much more than the work documented in this dissertation, but the qualities that makes a good researcher – the passion, endurance, dedication and respect for the scholastic endeavors of other people. Without his mentorship, I would not have reached this far.

I am grateful to Dr. A. Anders in the Lawrence Berkeley National Laboratory for his guidance and generous help of my work with the FCVA system. The Plasma Applications Group under his leadership is a pioneer team in plasma physics; I benefited tremendously from the insightful discussions with him and the collaborative work with his group.

I am grateful to Dr. D. Johnson. I have participated in numerous collaborative projects with his company, TiNi Alloy Ltd about shape memory alloy research; I started my work of Cu-Al-Ni shape memory alloy when I was a summer intern in his company. I regard working with him as very good experience of scientific exploration.

I am also grateful to Professor D. Bogy in my department and Dr. C. S. Bhatia who was at Hitachi Ltd and now is a faculty member at the National University of Singapore. I thank them for their consistent help to me on applying FCVA technique to the magnetic

storage devices. Through the Computer Mechanics Laboratory (CML) Sponsors' Meeting which is organized by Professor D. Bogy, I have maintained a close collaboration with magnetic storage device companies and was able to apply my FCVA research to the computer industry.

I thank K. Orvek, P. She-Jin, T. Liang and many other scientists, engineers in Intel Ltd for the financial support and delivery of many sample materials for surface studies.

I benefited enormously from my qualifying examination. I spent several months to prepare for it with my committee members: Professor T. Zohdi, Professor T. Keaveny, Professor D. Dornfeld and Professor R. Ritchie. I thank them for not just holding my qualifying examination as a test but utilizing that as a chance to broaden my knowledge scope and to prepare me better for the future research work.

My research works documented in this dissertation were mostly experimental studies. I thank those people who have helped in the experiments: Dr. J. W. Ager III and I. Sharp for Raman Spectra; Dr. K. M. Yu for RBS and PIXE spectra; V. Atloe and Dr. F. Ogletree for XPS; F. Wong and Professor Y. Suzuki for AFM; Professor R. Ramesh and L. Martin for XRR; E. Saiz for XRD; Dr. V. Radmilovic, Dr. T. Radetic and D. Ah-Tye for TEM; Prof. N. W. Cheung for ion beam; Dr. X. Meng for profilometer; Professor N. Balsara for DSC. Without these talented scholars my research work could not achieve this much.

For her companionship and encouragement till the journey's end, I thank Lingyan Jin.

Last but not least, I thank my parents. I am forever indebted to their unfailing love and support; I could not have done any of these without them.

# **Chapter 1**

## **Filtered Cathodic Vacuum Arc System**

Filtered cathodic vacuum arc (FCVA) is a low-temperature thin-film deposition technique that enables plasma beam manipulation [1-5]; its film precursors are energetic ions, as opposed to neutral atoms or clusters of atoms in the case of traditional deposition techniques, such as sputtering and chemical vapor deposition. Thus, the main advantage of FCVA is that the flow direction and energy of the film precursors can be independently controlled by magnetic and electrical fields, respectively. Moreover, the absence of a working gas enables FCVA depositions to be performed in a wide temperature range, which is critical to the growth of temperature-sensitive thin films. During arc discharging, the cathode (target material) undergoes complex solid-plasma phase transitions. The ions generated by the vacuum arc discharge exhibit element-specific intrinsic energies.

### **1.1 CATHODIC VACUUM ARC DISCHARGING**

#### **1.1.1 Cathodic Vacuum Arc Discharging Mechanism**

The plasma source in FCVA systems consists of an anode, one or multiple cathodes, an electrical control circuit and a trigger. When the anode and the cathode are biased with an electrical difference by the circuit, the trigger strikes to ignite the vacuum current of electron flow between the anode and the cathode. Electrons flow out of the cathode during the arc discharging which leads to high pressure and electrical potential gradient on the cathode surface. Pressure and electrical potential effects cause the arc current to be focused onto non-stationary tiny spots on the cathode surface, resulting in very high

pressure gradients within a distance of 1 mm from the cathode surface [3, 4]. This leads to the expulsion of the cathode material in the form of plasma of certain energy distribution and angle of flight. Plasma formation involves complex transitions of the cathode material from the solid state to equilibrium, dense, liquid states and, subsequently, to non-equilibrium expanding plasma [3, 6]. A magnetic field is needed at the cathode surface where the plasma is first generated to stabilize the arcing spots and orient the plasma flow [7]. Besides the desirable plasma, unwanted macroparticles of the cathode material are also formed by the arc discharging; therefore a magnetic or electrical plasma filter must be installed [8-12]. Plasma instabilities, difficulties with macroparticle filtering, and low deposition efficiency are the limiting factors of FCVA.

### **1.1.2 Two Modes of FCVA**

Pulsed arc and direct-current (dc) arc are two common modes of cathodic vacuum arc discharge. Pulsed arc was designed to reduce the plasma instability during the arc discharging. It was observed that, after plasma ignition, the arcing spots tend to migrate toward the cathode edge and change the arc discharge configuration, resulting in plasma fluctuations, irregular erosion of the cathode, and excessive formation of macroparticles [13, 14]. By reducing the arc discharging time for each cycle, high-frequency pulsed arc with short duration generates less plasma instabilities than dc arc systems [14, 15]. However, pulsed arc mode FCVA systems are limited by low deposition rates. In addition, pulsed arc systems are more complex than dc arc systems because of the need for in-phase coupling of the arc pulse and the substrate bias pulse during deposition and the high-frequency repetitions of plasma ignition.

Alternatively, the dc arc yields higher deposition rates [12, 16] but its inherent plasma instabilities are a major problem [13, 15, 16]. Plasma fluctuations in dc arc discharges occur due to the migration of the arcing spots toward the edge of the cathode surface [13-15]. The design of a simple, stable, and efficient dc FCVA system for high-quality film deposition has been a challenge.

## **1.2 IMPLEMENTATION OF A ‘CUSP-CONFIGURATION’ OF MAGNETIC FIELD FOR DIRECT-CURRENT (DC) PLASMA STABILIZATION**

The main theme of this study was to explore the efficacy of a special configuration of the magnetic field to stabilize the dc arc discharge and, hence, take advantage of the high deposition rates that characterize the dc arc to synthesize high-quality films. Therefore, the main objective of this chapter is to present a dc arc plasma-stabilizing mechanism incorporated in a three-dimensional magnetic filter.

Figure 1.1 shows schematics of the dc FCVA system used in this study. The plasma generated by arcing at the cathode situated between the cathode coil and the upstream coil is guided through the upstream, auxiliary, and downstream coils toward the substrate holder. For film uniformity, the 5-inch-diameter substrate holder is rotating during processing. Outside the downstream coil, four orthogonally mounted raster coils are used to raster the plasma beam (not shown in Figure 1.1 for clarity). The temperature of the cathode and the substrate holder is controlled by water cooling. A base chamber pressure of less than  $3 \times 10^{-7}$  Torr is achieved by a cryo-pump, while a 64-mm Kaufman ion source is used to sputter-clean the substrate surface by  $\text{Ar}^+$  ion bombardment prior to film deposition.

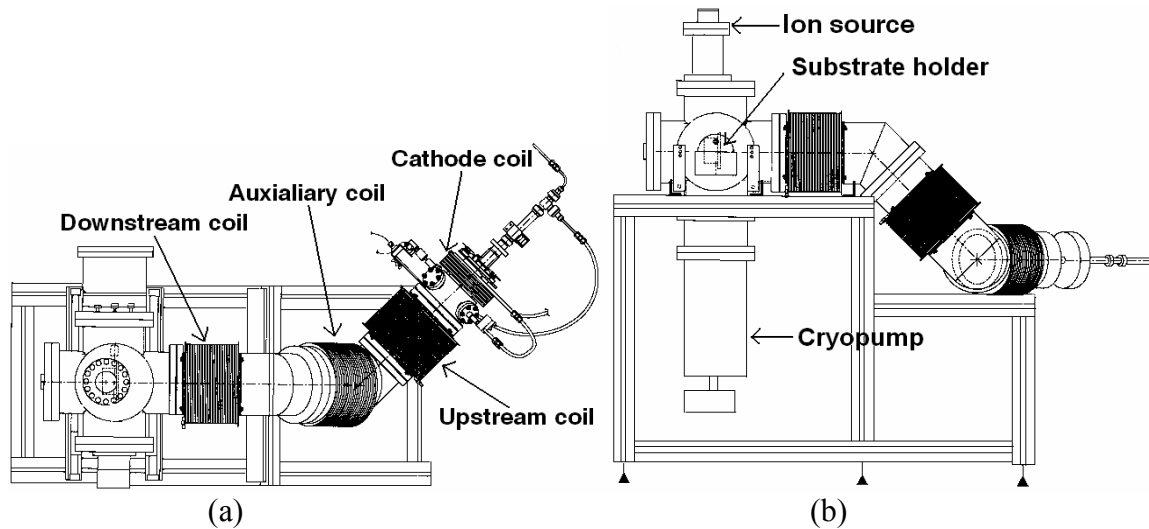


Figure 1.1 Schematics of (a) top and (b) front view of the FCVA system. Four raster coils attached to the outside of the downstream coil (not shown for clarity) are used to direct the plasma toward the substrate holder.

The magnetic field during dc arc discharge is shown schematically in Figure 1.2. The cathode consisting of a conductive solid material is mounted onto a cylindrical shaft used to move the cathode relative to the tubular copper anode such that to maintain a fixed cathode-to-anode distance. A mechanical trigger strikes the cathode while it is biased at  $-50\text{ V}$  relative to the anode to ignite the plasma. The current due to the arc discharge is kept constant by an electrical control circuit. Because the magnetic field generated by the cathode coil is opposite to that produced from the upstream coil, the magnetic field lines around the anode form a “cusp” configuration that stabilizes the arc current by maintaining a continuous electron flow from the cathode to the anode. The current through the cathode coil can be varied up to a maximum of  $25.9\text{ A}$ . The dense wire winding (106–203 mm wiring diameter) of the cathode coil produces a strong magnetic field ( $2.17\text{ mT/A}$  at the cathode solenoid center) that enhances the ion current and improves the arc discharge [7, 17]. In the present system, the superposition of the magnetic fields of the cathode coil (operated at its maximum current) and the upstream coil at the center of the cathode surface produces a field intensity of  $34.1\text{ mT}$ . The

relatively high strength and special configuration of the magnetic field maintain both the arc discharge configuration and the arc discharge current. Although this magnetic field configuration stabilizes the plasma, most of the plasma is lost to the anode, and only a small fraction travels parallel to the filter centerline toward the substrate. For a cathode consisting of pure carbon and a total arc discharge current of 70 A, the carbon ion flux rate at the substrate holder was measured to be  $\sim 1.48 \times 10^{15}$  ions/cm<sup>2</sup>·s.

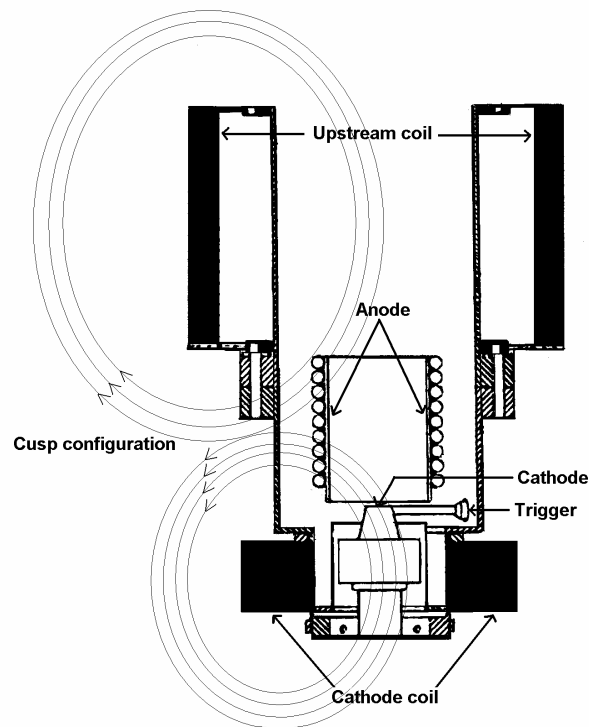


Figure 1.2 Schematic of the plasma stabilizing mechanism during dc arc discharge. The magnetic field lines produced by the cathode coil and the upstream coil are shown only at the left side of the coil cross section. The opposite directions of the magnetic fields of the two coils generate a “cusp” configuration in the magnetic field around the anode that maintains a stable arc current flow during the dc arc discharge.

The magnetic fields of the upstream, auxiliary, and downstream coils are of the same direction and are continuous within the filter space. To enhance the filtering effect and guide the plasma along the coil centerlines toward the substrate surface, the currents in the upstream, auxiliary, and downstream coils are usually set to their peak values (i.e.,

30.5, 30.9, and 29.6 A, respectively) using 233 mm-diameter wiring. The intensity of the magnetic field at the center of the upstream and downstream coils (normalized by the coil current) was measured to be 1.32 and 1.23 mT/A, respectively. The three-dimensional out-of-plane assembly configuration of these coils provides an effective means of depositing macro-particle-free thin films. Depending on the cathode material and the arc discharge current, the currents in the four raster coils must be adjusted to maintain the plasma at the substrate surface.

A three-dimensional out-of-plane configuration of the magnetic filter is used to prevent macro-particle and/or droplet deposition onto the growing film surface. The strong magnetic field of this filter focuses the plasma and preserves its energy distribution. Because of a neutralizing effect, ions travel close to the electrons guided by the magnetic field lines. Even though the net electrical charge in a given chamber volume is neutralized by the same spatial density of the ions and the electrons, the electrons move much faster than the ions, producing much higher electron currents [11]. For example, for a 70 A arc discharge current produced from a graphite cathode, the electron and ion currents were found to be equal to  $\sim 77$  and  $\sim 7$  A, respectively [11]. Because the ion-to-electron current ratio affects electric sheath formation, high-frequency pulsed biasing of the substrate is essential for preventing the build-up of a thick sheath due to the excess of electrons [18].

### **1.3 SUBSTRATE BIAS EFFECT AND ION IMPLANTATION**

In the absence of substrate biasing, ion bombardment onto the growing film surface occurs under intrinsic ion energy distributions. Ion energies in arc discharges have been measured for different elements [4, 7]. The energy of bombarding ions can be modulated

by applying a pulsed bias voltage to the substrate to regulate the plasma sheath. Substrate pulsed biasing with a negative voltage induces ion acceleration through the plasma sheath, resulting in energetic ion bombardment and ion implantation of the film. The film density, roughness, hardness, corrosion resistance, and biocompatibility are also strongly affected by substrate biasing. Substrate immersion into the plasma ball and acceleration of energetic ions in the direction of the local surface normal are additional intrinsic features of FCVA with substrate bias, resulting in conformal film deposition on three-dimensional objects.

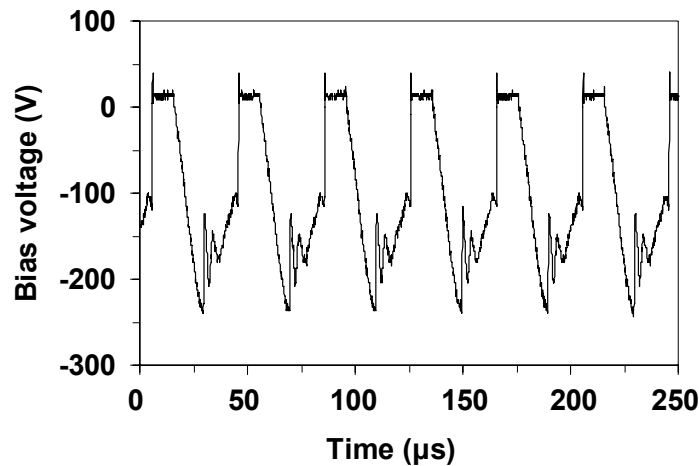


Figure 1.3 Waveform of pulsed substrate bias of  $-100$  V time-average magnitude and  $25$  kHz frequency.

A pulsed bias voltage was designed and applied to the substrate holder by a dc voltage source and an electrical chopper (Spark-le V, Advanced Energy Industries). Both the magnitude and the frequency of the pulsed bias can be adjusted by the dc voltage source and the electrical chopper. Figure 1.3 shows a bias waveform of  $-100$  V time-average magnitude and  $25$  kHz frequency recorded during film deposition in the present study. Excess electrons are discharged during the off period of the pulse cycle when zero or slightly positive voltage is applied to the substrate. Pulsed biasing also prevents the

expansion of the high-voltage plasma sheath and, in turn, electrical breakdown and substrate arcing [18, 19]. The ion energy at the substrate can be determined from the bias waveform and the intrinsic ion energy distribution. In the dc mode, the substrate ion bombardment is not in-phase with the pulsed substrate bias waveform, yielding a broader ion energy distribution (larger statistical deviation) than that obtained with the pulsed mode.

High-energy ions can knock-off atoms from the film surface, resulting in re-sputtering of the deposited material. Since film growth depends on the densities of both arriving ions and knocked-off film-forming atoms, substrate biasing decreases the film growth rate by increasing the re-sputtering yield. However, as shown in Chapter 2, the optimum deposition conditions are usually achieved with certain biasing, resulting in the enhancement of density, smoothness, and nanomechanical properties of the deposited films.

## Chapter 2

### Amorphous Carbon Films Deposited by FCVA

High demand for durable carbon films in various leading technologies, such as hard-disk drives, dynamic microdevices, and bioimplants, has generated increased interest in deposition of carbon films exhibiting uniformity, low roughness, high content of tetrahedral carbon atom hybridization ( $sp^3$ ), and good adhesion to substrates. Among various techniques for synthesizing carbon films, the most common are radio frequency sputtering [20-24], ion-beam deposition [25-30], laser ablation [31], and filtered cathodic vacuum arc (FCVA) [2, 6, 19, 27, 32, 33]. FCVA is a particularly promising technique for depositing continuous carbon films of high  $sp^3$  contents and excellent mechanical properties [2, 34-38]. For example, hydrogen-free carbon films synthesized by FCVA have been reported to exhibit hardness approaching that of diamond [19, 36, 39].

The efficacy of the FCVA system described in Chapter 1 is demonstrated in this chapter by findings revealing the microstructure and nano-mechanical properties of the deposited amorphous carbon ( $a$ -C) films. Results for the thickness, mass density, carbon bonding, and nano-mechanical properties of the deposited  $a$ -C films obtained with various microanalysis techniques are presented to illustrate the effectiveness of the magnetic field plasma-stabilizing mechanism to produce high-quality thin films.

#### 2.1 CARBON FILM DEPOSITION BY DC FCVA

Although the pulsed arc is characterized by the same discharge mechanism as the dc arc [15, 16], the film growth mechanisms in pulsed arc deposition differ from those in dc

arc deposition due to on/off plasma switching that may affect the subplantation process [25, 27] and the coupling of the plasma ion energy with the pulsed substrate bias. In addition, the ionization rate of the carbon plasma generated from a dc arc is slightly lower than that produced by a pulsed arc [14, 18]. The results presented below demonstrate that *a*-C films of good quality can also be synthesized by dc arc deposition.

A high-purity (99.999%) graphite cathode was used to deposit *a*-C films on 4-inch-diameter Si(100) wafers. The silicon wafer was mounted on the substrate holder that was rotated at 60 rpm during deposition to maintain the film uniformity. Both the cathode and the substrate holder were cooled off continuously during deposition by flowing water of a temperature equal to  $\sim 10^{\circ}\text{C}$ . Prior to film deposition, the wafer surface was sputter-cleaned *in-situ* by an  $\text{Ar}^+$  ion beam of 500 eV energy, 16 mA current, and  $60^{\circ}$  incident angle. The dc arc discharge current was set at 70 A, and the voltage between the cathode and the anode during film deposition was maintained at 24 V. Earlier studies have revealed a correlation between high hardness and high  $sp^3$  content of carbon films [2, 19, 34, 35, 39]. It was shown that the optimum ion energy for *a*-C film deposition is equal to  $\sim 120$  eV [2, 19, 35, 39-41], implying substrate bias voltage of  $-100$  V and original (intrinsic) ion energy of  $\sim 20$  eV. To demonstrate the significance of substrate biasing, two *a*-C films were deposited within 5 min – one without substrate biasing (film A) and one with a pulsed substrate bias of  $-100$  V time-average magnitude and 25 kHz frequency (film B). The film thickness was obtained as the height of the step created by masking a portion of the wafer surface during deposition, measured with a laser interferometer (NewView 100, ZYGO) equipped with a 632.9-nm wavelength He-Ne

laser beam. The thickness of films A and B was found equal to 68 and 38 nm, respectively.

## 2.2 CHARACTERIZATION OF FCVA-DEPOSITED CARBON FILMS

### 2.2.1 Microanalysis

Figure 2.1 shows a representative X-ray diffraction (XRD) spectrum of film A obtained with a conventional X-ray beam of 0.15406 nm wavelength generated by a Cu-K $\alpha$  X-ray tube (D500, Siemens) under conditions of 30 mA generator current, 40 kV generator voltage, 0.05 $^\circ$  step size, and 2 s step time. The absence of any significant crystalline reflections indicates that the synthesized carbon film is amorphous. The small peak at  $2\theta = 38.8^\circ$  may be an indication of the existence of SiC nanocrystallites at the interface between the *a*-C film and the Si(100) substrate. The formation of SiC is attributed to C and Si atom interdiffusion across the interface during film deposition due to the bombardment of energetic carbon ions.

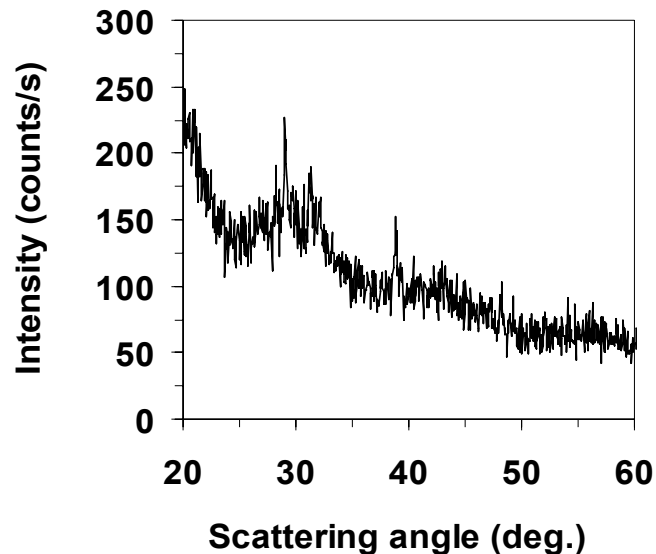


Figure 2.1 XRD spectrum of film A synthesized under zero substrate bias.

Figure 2.2 shows Rutherford backscattering spectrometry (RBS) spectra of films A and B and bare Si(100) obtained with a custom-made RBS system that uses an energetic  $\text{He}^+$  ion beam generated from a 2.5 MeV Van de Graaff electrostatic accelerator.

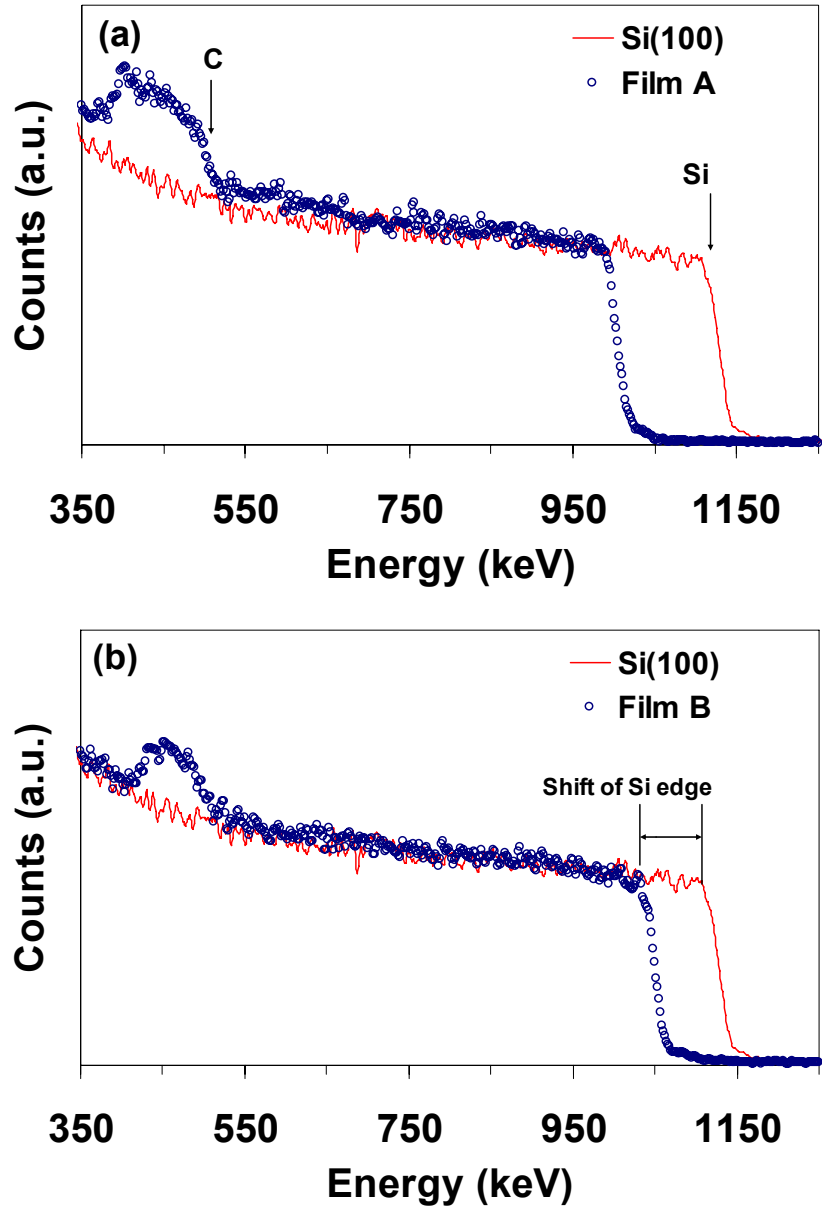


Figure 2.2 RBS spectra of *a*-C films synthesized under (a) zero substrate bias (film A) and (b) – 100 V time-average magnitude and 25 kHz frequency pulsed substrate bias (film B). The RBS spectrum of bare Si is also shown in each plot for comparison. The C and Si edge positions are shown in (a), and the shift of the Si edge position due to the *a*-C film is shown in (b).

Backscattered ions were collected by two Si detectors positioned at an angle of  $165^\circ$  with respect to the incident beam. The samples were tilted by an angle of  $55^\circ$  from the incident beam direction. The carbon atom density was determined from the shift of the Si edge and the C peak area on top of the Si signal background. Both methods yielded very similar C atom densities, i.e.,  $9.9 \times 10^{17}$  atoms/cm<sup>2</sup> for film A and  $6.3 \times 10^{17}$  atoms/cm<sup>2</sup> for film B. Using these results and the film thickness measurements, the density of films A and B was found equal to 2.92 and 3.33 g/cm<sup>3</sup>, respectively. A comparison of these density values with those of graphite ( $\sim 2.15$  g/cm<sup>3</sup>) and diamond ( $\sim 3.51$  g/cm<sup>3</sup>) shows a much higher  $sp^3$  fraction in film B ( $-100$  V bias) than film A ( $0$  V bias). In fact, earlier studies [9, 37, 42, 43] have shown that the  $sp^3$  fraction in *a*-C films deposited under  $0$  and  $-100$  V substrate bias voltage was approximately equal to 50 and 70 at%, respectively.

Figure 2.3 shows Raman spectra of films A and B obtained with the 488-nm line of an Ar<sup>+</sup> laser (model 85, Lexel Laser) operated at 150 mW and a macroscopic optical setup. The refracted light was collected by a spectrometer (model 1877, SPEX) using an exposure time of 30 s in each scan. The spectra from two samples were aligned with the second Si peak at  $991.2$  cm<sup>-1</sup>, as in a previous study [2]. After background subtraction, the Raman spectra of Figure 2.3 were deconvoluted into two Gaussian peaks. The dominant peak (G band) at  $1589.8$  and  $1584.8$  cm<sup>-1</sup> in the spectra of films A and B, respectively, corresponds to the in-plane Raman mode of graphite [44, 45]. The small peak (D band) at  $1372.2$  and  $1349.2$  cm<sup>-1</sup> in the spectra of films A and B, respectively, is assigned to small graphitic domains [41, 44]. The D-to-G band area ratio of films A and B is equal to 0.246 and 0.207, respectively, suggesting relatively high  $sp^3$  content for both films [41, 45]. Since Raman is sensitive to  $sp^2$  hybridization and largely insensitive to  $sp^3$

hybridization [41, 44, 45], the lower intensity of the Raman spectrum of film B compared to that of film A is attributed to the higher  $sp^3$  content of film B, consistent with the RBS results.

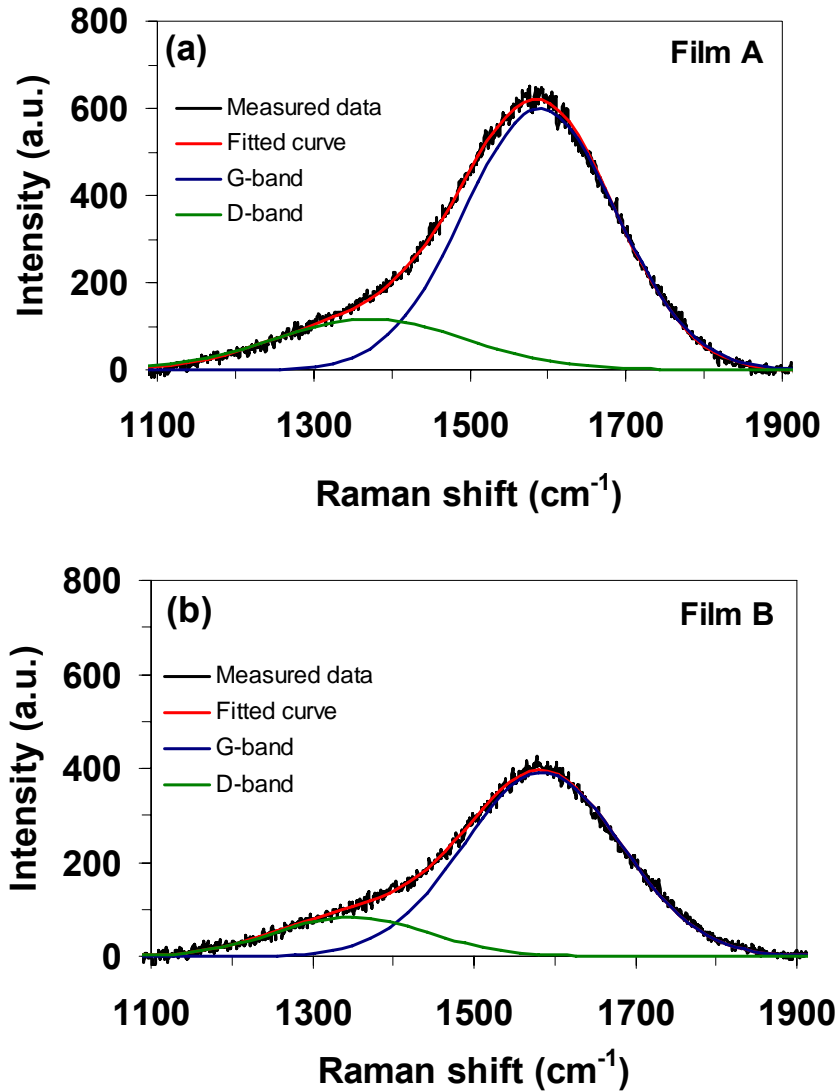


Figure 2.3 Raman spectra of  $a$ -C films synthesized under (a) zero substrate bias (film A) and (b) – 100 V time-average magnitude and 25 kHz frequency pulsed substrate bias (film B). The spectra were acquired after linear background subtraction.

Figure 2.4 shows the X-ray photoelectron spectroscopy (XPS) C1s spectra of films A and B obtained with an XPS system (PHI 5400, Physical Electronics) equipped with a monochromatic Al-K $\alpha$  (1486.6 eV) X-ray source and a spectrometer operated at pass

energy of 35.75 eV. The C1s spectra were acquired in 50-ms steps of energy equal to 0.05 eV and were deconvoluted after performing a Shirley inelastic background subtraction [46]. A detailed description of the deconvolution method can be found elsewhere [24].

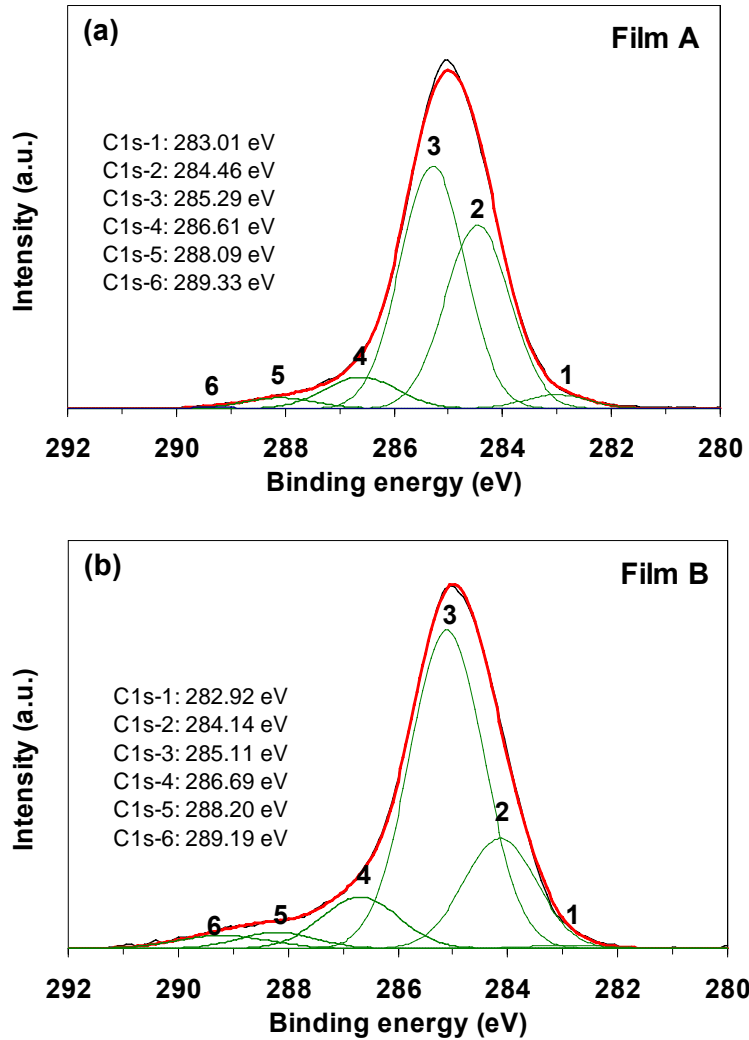


Figure 2.4 C1s XPS spectra (black curves) of *a*-C films synthesized under (a) zero substrate bias (film A) and (b)  $-100$  V time-average magnitude and 25 kHz frequency pulsed substrate bias (film B) with fits (red curves) obtained from six Gaussian distributions (green curves). The spectra were acquired after performing inelastic background subtraction.

Six Gaussian distributions of characteristic binding energies associated with certain carbon chemical states were fitted to each C1s envelope. The C1s-1, C1s-2, and C1s-3 distributions correspond to  $sp^1$ ,  $sp^2$ , and  $sp^3$  carbon hybridizations, respectively. The  $sp^3$

carbon fractions in the amorphous phases of the films, estimated from the deconvolution of the C1s XPS spectra by the method proposed by Jackson and Nuzzo [47] and Diaz et al. [48], were found to be >50 and >70 at%, respectively. The C1s-4, C1s-5, and C1s-6 distributions are attributed to different bonding states of C and O atoms from the ambient chemisorbed at the film surface [20, 24]. It has been reported that a dc arc produces *a*-C films of slightly lower  $sp^3$  contents than those synthesized by a pulsed arc [16]. This difference can be partially attributed to plasma discontinuities in pulsed arc systems that affected subplantation [25, 27], i.e., fluctuations in ion bombardment may influence surface relaxation, diffusion, and thermal spike processes. A more important reason for the lower  $sp^3$  content of the dc-arc-deposited *a*-C films is the broader distribution of the ion bombardment energy delivered to the substrate in the absence of in-phase coupling of the plasma intensity with the pulsed substrate bias.

### 2.2.2 Mechanical Testing

Figure 2.5 shows representative nanoindentation curves of films A and B obtained with a surface force microscope (SFM) [49] consisting of an atomic force microscope (Nanoscope II, Digital Instruments) retrofitted with a capacitive force transducer (Triboscope, Hysitron) having a cubic-corner diamond tip of nominal radius equal to ~67 nm. The tip was calibrated with an ultrasoft fused quartz sample of in-plane modulus (reduced modulus)  $E/(1-\nu^2) = 69.6$  GPa, where  $E$  is the elastic modulus and  $\nu$  is the Poisson's ratio. The small hysteresis area between the loading and unloading curves of the nanoindentation responses yield a dissipation energy of ~0.127 pJ (film A) and ~0.135 pJ (film B) and negligibly small residual indentation depths (~88% elastic recovery for each film). This implies that indentation depths >20% of the thickness of

these  $a$ -C films (or maximum indentation load equal to  $150 \mu\text{N}$ ) resulted in predominantly elastic deformation.

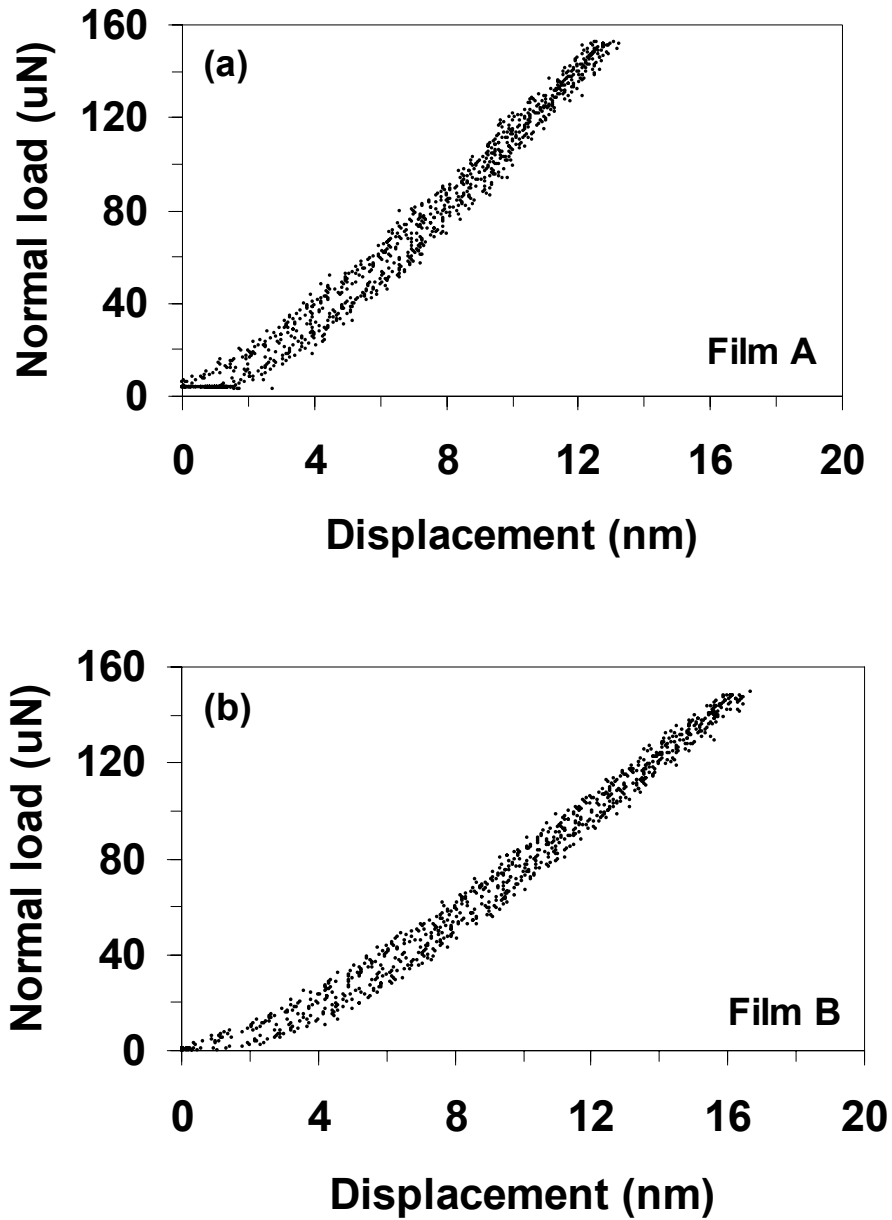


Figure 2.5 Nanoindentation curves of  $a$ -C films synthesized under (a) zero substrate bias (film A) and (b)  $-100 \text{ V}$  time-average magnitude and  $25 \text{ kHz}$  frequency pulsed substrate bias (film B) for a maximum load of  $150 \mu\text{N}$  and loading/unloading times equal to  $2 \text{ s}$ .

Figure 2.6 shows the mean contact pressure and in-plane elastic modulus of films A and B versus maximum displacement for a triangular loading function with loading and

unloading times both equal to 2 s. The mean contact pressure was calculated as the ratio of the maximum load to the projected contact area of the diamond tip, and the

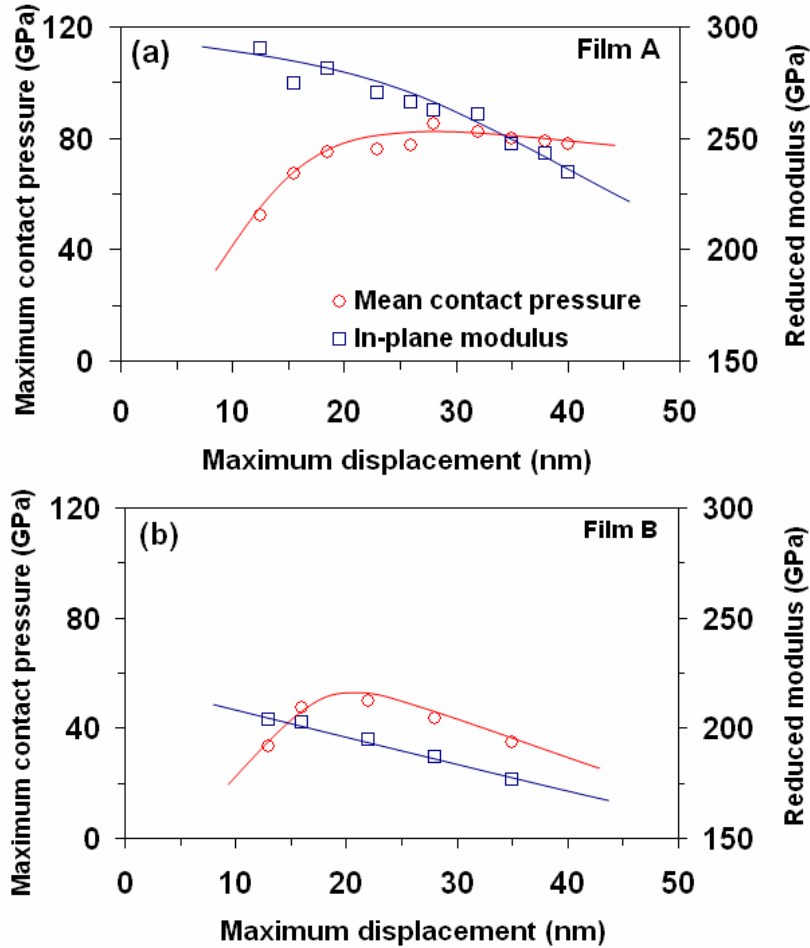


Figure 2.6 Maximum contact pressure and reduced modulus of *a*-C films synthesized under (a) zero substrate bias (film A) and (b)  $-100$  V time-average magnitude and 25 kHz frequency pulsed substrate bias (film B).

reduced modulus from the stiffness estimated at the maximum displacement point of the unloading curve [49, 50]. The initial increase in the mean pressure with the maximum displacement is due to the evolution of subsurface plasticity. By definition, the maximum mean pressure (reached at a displacement of  $\sim 20$  nm for both films) corresponds to the effective hardness of the film-substrate medium [49, 51]. For films A and B, the effective hardness is equal to  $\sim 80$  and  $\sim 55$  GPa, respectively. Despite the higher  $sp^3$  content of film B, the effective hardness is less than that of film A. This is attributed to the more

significant substrate effect on the contact pressure resulting from the higher displacement-to-thickness ratio determined at the peak contact pressure for film B than for film A. The reduced modulus of both media decreases with the increase of the maximum displacement approaching that of the substrate. Similar to the mean contact pressure and effective hardness, the substrate effect on the reduced modulus is more pronounced for the thinner film B. Considering the in-plane modulus (150 GPa) and hardness (~8 GPa) of the Si(100) substrate, the results shown in Figure 2.6 demonstrate a significant enhancement of both surface elastic stiffness and penetration resistance by the thin *a*-C films, illustrative of the high-quality films produced by dc arc deposition in the presence of the plasma-stabilizing magnetic-field mechanism of the present FCVA system.

### **2.3 SUMMARY**

The effectiveness of the dc FCVA system presented in Chapter 1 was demonstrated by results of the microstructure and nanomechanical properties of *a*-C films deposited on Si(100) under unbiased and optimum pulsed bias conditions. XRD, RBS, Raman, and XPS analyses yielded insight into the bonding structure of *a*-C films produced by dc arc discharge. The high  $sp^3$  content (>50% without bias and >70% with optimum pulsed bias), high density (3.33 g/cm<sup>3</sup> with optimum pulsed bias and 2.92 g/cm<sup>3</sup> without bias), and high hardness of the deposited *a*-C films illustrate the importance of the magnetic-field mechanism that stabilized the plasma in the dc arc system of this study.

## **Chapter 3**

### **FCVA Treatment of Silicon Surfaces**

Silicon is the most widely used semiconductor material and the main structural material in microelectromechanical systems (MEMS) technology. Surface treatment of silicon devices used in semiconductor and MEMS applications is complicated by scale effects. Carbon films have been used as protective overcoats in numerous industrial and scientific applications due to their high hardness and elastic modulus and excellent corrosion resistance [34-36]. In view of a continuing scale-down trend in silicon-based technologies, there is a need to reduce the overcoat film thickness while preserving its protective properties. However, the smallest carbon film thickness that can be deposited on silicon and the associated FCVA conditions have not been determined yet.

One of the main objectives of this study was to examine if the good properties of carbon overcoats synthesized under  $\sim 120$  eV carbon ion energy can be preserved while decreasing the process time, which is linearly related to the ion fluence, to obtain uniform carbon films of minimum thickness on silicon substrates. The FCVA conditions corresponding to the ultrathin carbon film region were studied by fixing the process time and tuning the substrate bias. X-ray photoelectron spectroscopy (XPS) was used to systematically examine carbon bonding changes in terms of the implantation ion fluence and the substrate bias. Film thickness and composition depth profiles were determined from T-DYN simulations and X-ray reflectivity (XRR) measurements. The film roughness, measured with an atomic force microscope (AFM), was interpreted in terms

of atomic carbon bonding and carbon atom diffusion at the film surface. The nanomechanical properties of the films were investigated with a surface force microscope (SFM). The results of this chapter provide insight into carbon bonding formation and growth mechanisms of ultrathin carbon films synthesized by the FCVA method on silicon surfaces.

### **3.1 SUBPLANTATION MECHANISM OF ENERGETIC CARBON ION BOMBARDMENT**

#### **3.1.1 T-DYN Simulations of Ion Implantation**

For a film thickness of only a few nanometers, compositional variations could be significant due to the effect of interfaces. Ion implantation simulations have provided means of examining stoichiometric distributions. Important insight has been gained from calculations of energetic atom displacements in solids and simulations of ion trajectories [52-57]. The TRIM code, one of the most common Monte Carlo ion trajectory simulation programs that initially accounted only for ion interactions with the virgin target [58], was modified to include the effects of ion backscattering, resputtering, target atom displacement, and phonon/electron excitations, hence enabling dynamic simulations involving ion cascades and continuously changing composition [59, 60]. T-DYN is a dynamic simulation code based on TRIM, which has been verified by experimental results of atomic mixing [61], depth profile [25, 26, 62], and sputtering yield [63, 64].

Binary atom collisions during the FCVA process were simulated by the classical-trajectory method using the T-DYN software (version 4.0) to obtain composition profiles. The experimentally measured ion energy and flux rate were used as the input parameters in the T-DYN simulations, which were performed to a depth of 20 nm from the top

surface layer in 100 evenly split channels. Details of the conditions and logarithms are given elsewhere [61]. The binding energy for Si and C were set at 2.32 and 2.27 eV, respectively, and the corresponding surface binding energies at 4.7 and 7.41 eV, respectively. These are standard values for solid-state silicon and graphite. The impinging ion energy was set equal to the summation of the initial carbon ion energy of 20 eV (the statistically most likely value [3]) and the energy due to substrate biasing (in the range of 0–300 eV). All ions were assumed to impinge onto the substrate surface in the normal direction.

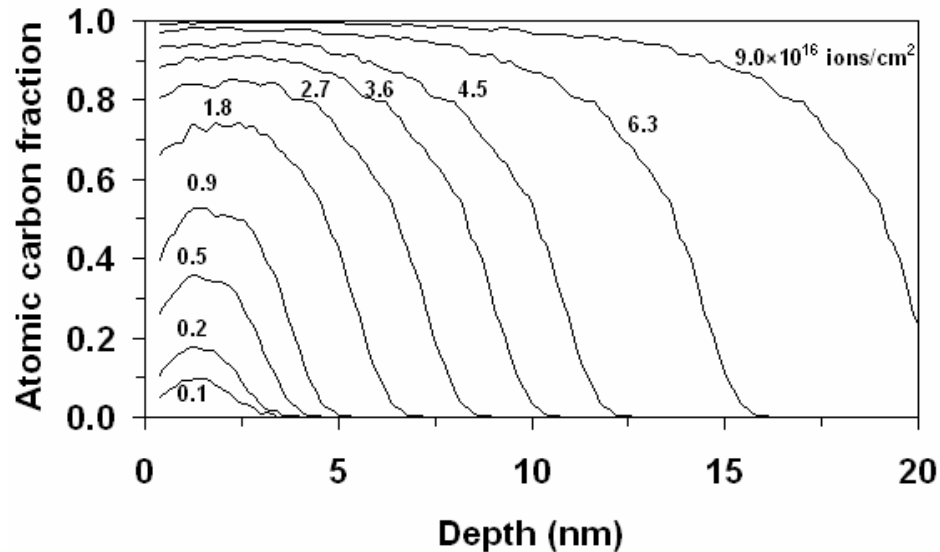


Figure 3.1 Carbon depth profiles simulated with the T-DYN code for 120 eV kinetic energy of carbon ions impinging perpendicular to a silicon substrate surface.

Earlier studies have shown that the highest  $sp^3$  content and best mechanical properties of relatively thick carbon films corresponded to a carbon ion energy of ~120 eV [2, 19, 35, 40]. Therefore, T-DYN simulations were first performed for carbon ion energy of 120 eV. Figure 3.1 shows carbon depth profiles in silicon for carbon ion fluence in the range of  $(0.1–9.0) \times 10^{16}$  ions/cm<sup>2</sup>. It can be seen that the increase of the ion

fluence enhanced the near-surface carbon concentration, but also caused the carbon profile to extend deeper into the silicon substrate.

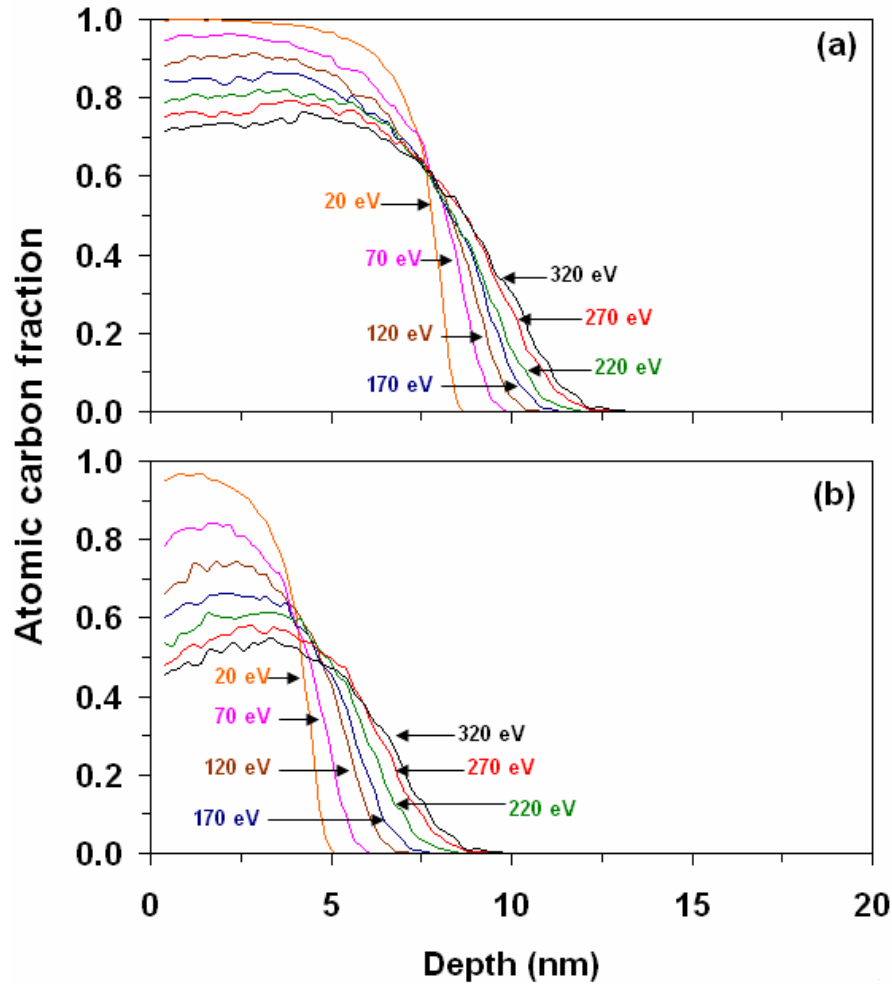


Figure 3.2 Carbon depth profiles simulated with the T-DYN code for 20–320 eV kinetic energy of carbon ions impinging perpendicular to a silicon substrate surface and carbon ion fluence equal to (a)  $3.6 \times 10^{16}$  and (b)  $1.8 \times 10^{16}$  ions/cm<sup>2</sup> corresponding to 0.4 and 0.2 min process time.

For low ion fluence ( $<1.0 \times 10^{16}$  ions/cm<sup>2</sup>), the maximum carbon concentration occurs at a distance of  $\sim 1.5$  nm below the surface, which is the average stopping range of 120-eV carbon ions in silicon. Although a fluence of  $1.8 \times 10^{16}$  ions/cm<sup>2</sup> yielded a high carbon fraction of  $\sim 75$  at.% at the surface, the carbon profile extended to a depth of  $\sim 6$  nm. For ion fluence above  $6.3 \times 10^{16}$  ions/cm<sup>2</sup>, uniform and high carbon concentration ( $\sim 90$  at.%) profiles were obtained up to depths of  $\sim 10$  nm. The compositional gradients in

the depth profiles suggest that prescribing a unique film thickness for a given ion fluence is subjective. Therefore, it is preferred to use the composition profile for each FCVA process rather than the film thickness.

Figure 3.2 shows T-DYN simulation results revealing the effect of carbon ion energy (or substrate bias) under fixed ion fluence on the carbon depth profile. The ion fluence of  $3.6$  and  $1.8 \times 10^{16}$  ions/cm<sup>2</sup> corresponds to a process time of  $0.4$  and  $0.2$  min, respectively. A comparison of Figures 3.2(a) and 3.2(b) indicates that the surface carbon concentration increases with the ion fluence and decreases with the increase of the ion kinetic energy, while the thickness of the carbon-modified surface layer increases with the ion kinetic energy and the ion fluence. The shallowest carbon profile ( $\sim 5$  nm) of high surface carbon content ( $\sim 95$  at.%) is achieved for  $\sim 20$  eV ion kinetic energy and  $1.8 \times 10^{16}$  ions/cm<sup>2</sup> ion fluence, i.e.,  $0.2$  min process time without substrate bias. High ion energy enhances the implantation range of the carbon ions, resulting in the broadening of the carbon depth profile. Therefore, a low ion kinetic energy is necessary to synthesize a carbon ( $\sim 95$  at.% C) film of minimum thickness ( $\sim 2$  nm).

### **3.1.2 FCVA Deposition of Ultrathin Carbon Films**

Synthesis of carbon films on Si(100) substrates was accomplished with the dc FCVA system presented in Chapter 1. The substrate was pulsed biased at a frequency of  $25$  kHz with a voltage of time-averaged value in the range of  $0$  to  $-300$  V. All of the FCVA experiments were performed on 4-inch-diameter Si(100) wafers that were first sputter-cleaned in-situ for  $3$  min with a  $500$ -eV,  $16$ -mA Ar<sup>+</sup> ion beam at a  $60^\circ$  incidence angle. During sputter cleaning and FCVA processing, the substrate holder was rotated at  $60$  rpm to obtain an etched layer and a carbon film of uniform thickness. A cryogenic

pump was used to obtain a base pressure of less than  $3 \times 10^{-7}$  Torr in all of the film depositions.

Since a uniform ion impinging energy was assumed in the T-DYN simulations and chemical reactions, diffusion, and atomic bond formation were neglected, the simulation results are applicable for a low ion fluence under which the previous mechanisms can be neglected as producing insignificant localized effects on the film composition. The T-DYN results were validated by XRR measurements obtained with a commercially available apparatus (X'Pert PRO MRD, PANalytical, The Netherlands) with an Cu-K $\alpha$  X-ray tube that produced an X-ray wavelength of 0.154052 nm. The generator current and voltage were set at 40 mA and 45 kV, respectively, the step size at  $0.005^\circ$ , and the step time at 0.5 s. The intensity of the reflected X-ray depends on the surface and near-surface electron density [65]. The depth at which the carbon fraction decreases sharply controls the intensity of the reflected X-ray.

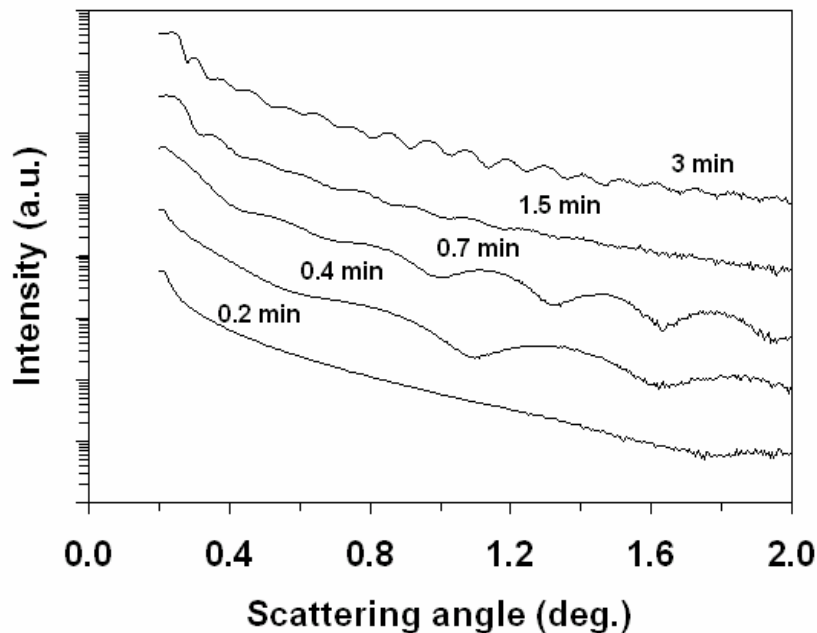


Figure 3.3 XRR results for 0.2–3 min process time,  $\sim 120$  eV carbon ion kinetic energy ( $-100$  V bias voltage of 25 kHz frequency) and  $\sim 1.48 \times 10^{15}$  ions/cm $^2$ ·s ion flux.

Figure 3.3 shows XRR curves for  $\sim 120$  eV ion kinetic energy, i.e.,  $-100$  V pulsed substrate bias. The periodic fringe patterns can be related to the X-ray travel length through the sample surface [43, 50]. From a Fast Fourier Transform (FFT) of the periodic curves [66, 67], the calculated depth of the X-ray reflection was found equal to 40.2, 27.1, 12.5, 6.7, and 2.3 nm for process time equal to 3.0, 1.5, 0.7, 0.4, and 0.2 min, respectively. The 2.3, 6.7, and 12.5 nm depth values are close to the shoulder edge of the T-DYN simulation profiles for ion fluence equal to 1.8, 3.6, and  $6.3 \times 10^{16}$  ions/cm<sup>2</sup> (Figure 3.1). The critical angle in the XRR curves decreased with the ion fluence, suggesting a decrease in the density of the surface layer [43]. However, density calculations based on the critical angle were avoided in the absence of a uniform composition profile.

### **3.2 CHEMICAL BONDING ANALYSIS BY X-RAY PHOTOELECTRON SPECTROSCOPY (XPS)**

The synthesized carbon films were characterized by XPS using the system described in Chapter 2. In the case of ultrathin films, bonding of the film to the substrate and ambient adsorbents cannot be neglected. In addition, XPS has a detection depth of  $\sim 10$  nm and, therefore, is suitable for surveying the overall bonding state of films with thickness less than 10 nm.

Figure 3.4 shows a deconvoluted XPS C1s peak corresponding to  $\sim 170$  eV ion kinetic energy ( $-150$  V pulsed substrate bias voltage of 25 kHz frequency) and 0.4 min process time, which is representative of the C1s peaks obtained from most FCVA experiments. Six Gaussian profiles of characteristic binding energies were fitted to the C1s peak. Details of the deconvolution and interpretation of each profile can be found in Chapter 2. Peaks C1s-4, C1s-5, and C1s-6 correspond to carbon bonding to surface

adsorbents [20, 24], which, hereafter, will be referred to as satellite peaks. The sum of the satellite peak areas indicates the percentage of surface adsorbent-related carbon bonding. The formation of  $sp^3$  hybridizations (C1s-3 profile) in carbon films has been attributed to various mechanisms explained by different models, such as subplantation [25, 27, 34, 35], carbon-carbon atomic probabilistic collision [23], and compressive stress [68, 69] models. However, these mechanisms are applicable for relatively thick carbon films synthesized under conditions of high ion fluence.

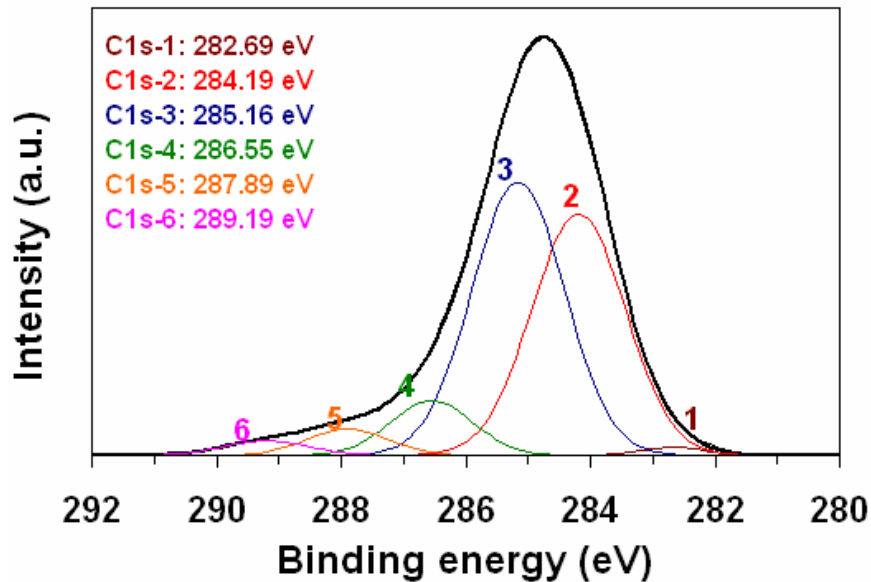


Figure 3.4 C1s XPS spectrum of C1s core level peak for  $\sim 170$  eV carbon ion kinetic energy ( $-150$  V bias voltage of 25 kHz frequency) and 0.4 min process time ( $3.6 \times 10^{16}$  ions/cm<sup>2</sup> ion fluence). The spectrum was fitted with six Gaussian curves after inelastic background subtraction.

A dramatic change in carbon hybridization was observed with the decrease of the ion fluence. For an ion kinetic energy of  $\sim 120$  eV, the binding energies corresponding to  $sp^1$ ,  $sp^2$ , and  $sp^3$  hybridizations exhibited marginal changes with the variation of the process time, except for very short process times, i.e., very shallow depth profiles [Figure 3.5(a)]. The higher binding energies obtained for relatively short process times (i.e.,  $< 0.5$  min) correlate with a significant change in  $sp^2$  and  $sp^3$  hybridizations [Figure 3.5(b)]. This result is in qualitative agreement with the reported low  $sp^3$  fraction of thin carbon

films [33]. According to the subplantation model [25-27], energetic carbon ions penetrate the substrate up to some depth, and the resulting carbon densification in the subsurface leads to a higher  $sp^3$  content compared to that in the near-surface region ( $<1.5$  nm). Thus, the enhancement of  $sp^3$  hybridization is driven by a subsurface mechanism that requires a minimum thickness of high carbon concentration of  $\sim 1.5$  nm. Another plausible explanation is the presence of a tensile stress in the tail of the carbon profile, as proposed for carbon/silicon interfaces where carbon atom bonding to the silicon surface gives rise to a tensile stress [21]. Although this tensile stress can be relaxed by diffusion, a low  $sp^3$  fraction is not favored in the carbon-silicon interfacial layer.

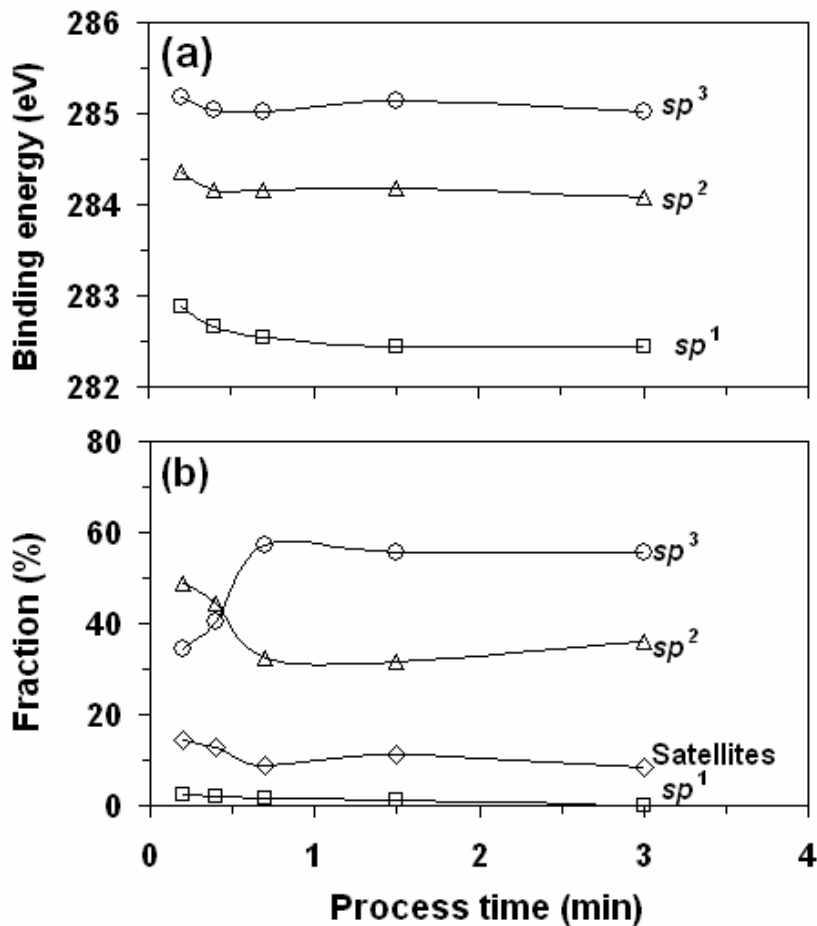


Figure 3.5 (a) Binding energies of characteristic Gaussian fits of C1s core level peak and (b) fraction of carbon constituents of deconvoluted C1s core level peak versus process time for  $\sim 120$  eV carbon ion kinetic energy ( $-100$  V bias voltage of 25 kHz frequency).

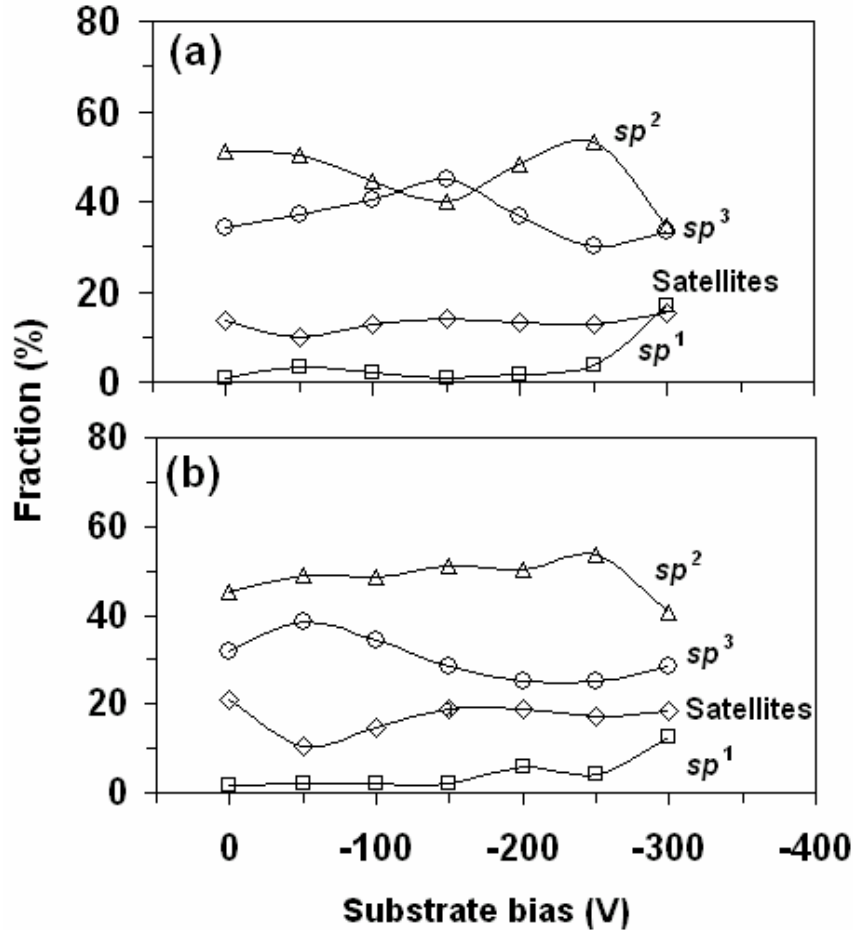


Figure 3.6 Carbon constituents of deconvoluted C1s core level peak versus substrate bias voltage of 25 kHz frequency for (a) 0.4 and (b) 0.2 min process time corresponding to  $3.6$  and  $1.8 \times 10^{16}$  ions/cm<sup>2</sup> ion fluence.

Low-ion-fluence FCVA was further studied with XPS by varying the substrate bias. Figure 3.6 shows the variation of different carbon bonding with the substrate bias for short process time. As mentioned earlier, the satellite fractions are related to physical adsorption of airborne contaminants, depending on the film microstructure and surface carbon bonding, i.e., unstable carbon at the surface may easily react with ambient contaminants. These reactions can cause a decrease in the  $sp^3$  content [70]. The highest  $sp^3$  content (~45%) was obtained with -150 V substrate bias voltage for process time fixed at 0.4 min [Figure 3.6(a)]. The decrease of the process time to 0.2 min to produce a shallower carbon profile necessitated a bias voltage of -50 V in order to obtain a

maximum  $sp^3$  content of ~40% [Figure 3.6(b)]; however, these FCVA process conditions do not appear to be as conducive to  $sp^3$  formation as those of the previous case. According to the subplantation model, substrate penetration by low-energy ions induces a compressive stress and promotes  $sp^3$  hybridization [25, 27]. Any excess of ion energy can cause stress relaxation, atomic diffusion, and a decrease in  $sp^3$  bond formation [22, 40]. The high  $sp^1$  and low  $sp^2$  contents obtained under a substrate bias voltage of  $-300$  V can be attributed to a chemical reaction between C and Si. X-ray diffraction revealed the formation of nanocrystalline SiC at the carbon-silicon interface (Chapter 2). For carbon bonded with silicon, a significant  $sp^1$  peak (C1s-1 position) has been observed in the deconvoluted XPS C1s peak [71-73]. It is likely that for an average ion kinetic energy of  $\sim 320$  eV, a significant portion of the ion energy distribution was above the activation energy of SiC and, therefore, the  $sp^1$  hybridization is related to both carbon-carbon and carbon-silicon linear bonding.

### 3.3 SURFACE ROUGHNESS EVOLUTION DUE TO FCVA TREATMENT

The root-mean-square (RMS) surface roughness of the carbon films was measured with an AFM (Dimension 3100, Veeco Digital Instruments) using  $1 \times 1 \mu\text{m}^2$  scan areas. The AFM was operated in the tapping mode, using a drive frequency of 259.332 kHz and a scan rate of 2 Hz.

The roughness data shown in Figure 3.7 provide information for the initial stage of surface modification and additional evidence of  $sp^3$  formation. In general, lower  $sp^3$  content is accompanied by higher surface roughness [27]. However, for ultrathin films the surface roughness is controlled by the silicon substrate [74]. The data point at zero process time corresponds to the  $\text{Ar}^+$  sputter-cleaned silicon substrate. Carbon atom

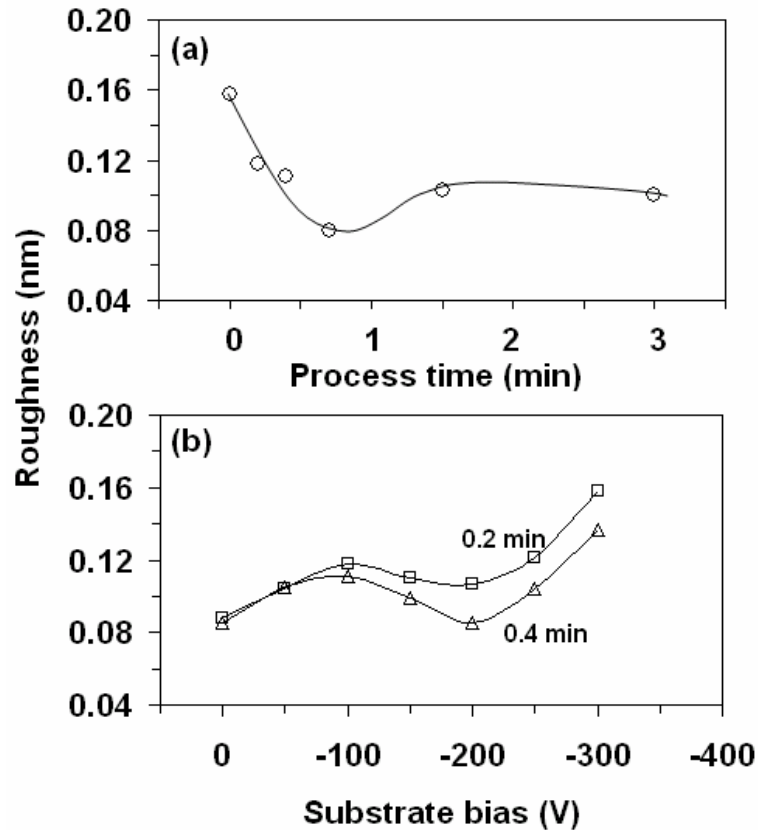


Figure 3.7 (a) Surface roughness versus process time for  $\sim 120$  eV ion kinetic energy ( $-100$  V bias voltage of 25 kHz frequency) and (b) surface roughness versus substrate bias voltage of 25 kHz frequency for 0.4 and 0.2 min process time corresponding to  $3.6$  and  $1.8 \times 10^{16}$  ions/cm<sup>2</sup> ion fluence. The zero-time data point in (a) corresponds to the roughness of the Ar<sup>+</sup> sputter-cleaned Si(100) substrate surface.

adsorption and bonding at the sputter-roughened silicon surface is a spontaneous and highly exothermic process [75], presumably resulting in the decrease of the initial roughness. The  $\sim 0.7$  min process time may correspond to the transition from relatively low to high carbon concentration profile and the greatest effect of surface smoothing by carbon atom adsorption. The roughness values for the longer process time correspond to carbon profiles with increased  $sp^3$  contents. The decrease of the surface roughness with the increase of the process time may be related to the increase of the ion fluence, which promoted surface smoothing through the increase of the amount of carbon delivered to the surface. The low surface roughness for 0 and  $-50$  V bias voltage shown in Figure

3.7(b) may be attributed to a greater affinity of carbon atoms to adsorb and diffuse at the substrate surface, resulting in a smoothing effect. A local roughness peak is reached at a  $-100$  V bias voltage due to deeper ion penetration and less carbon species at the surface resulting from the higher ion energy. The decrease in surface roughness for bias voltage between  $-100$  and  $-200$  V can be associated with the lower  $sp^3$  content of the film profiles, causing a slight increase in resputtering and surface smoothing by low-degree surface diffusion. The significant roughening due to bias voltage above  $-200$  V is attributed to the intense bombardment of carbon ions that induced excessive atomic diffusion and surface damage [22, 25, 27, 40].

### **3.4 NANOMECHANICAL PROPERTIES OF FCVA-TREATED SILICON SURFACES**

The surface nanomechanical properties of the carbon films were studied with a SFM consisting of an AFM (Nanoscope II, Digital Instruments) retrofitted with a force transducer (Hysitron, Minneapolis, MN) having a sharp diamond tip of nominal radius equal to  $\sim 67$  nm. A triangular loading function with both loading and unloading times equal to 2 s was used in all the nanoindentations.

Figure 3.8(a) shows a representative nanoindentation response for a sample processed at  $\sim 120$  eV ion kinetic energy and 3 min process time. The small residual displacement after unloading and the force hysteresis defined by the loading and unloading paths of the nanoindentation response illustrate the resistance of the surface to plastic deformation. The significantly larger force hysteresis of the original silicon substrate demonstrates the marked enhancement of the surface resistance to plastic deformation in the presence of the carbon film. Using such force versus displacement

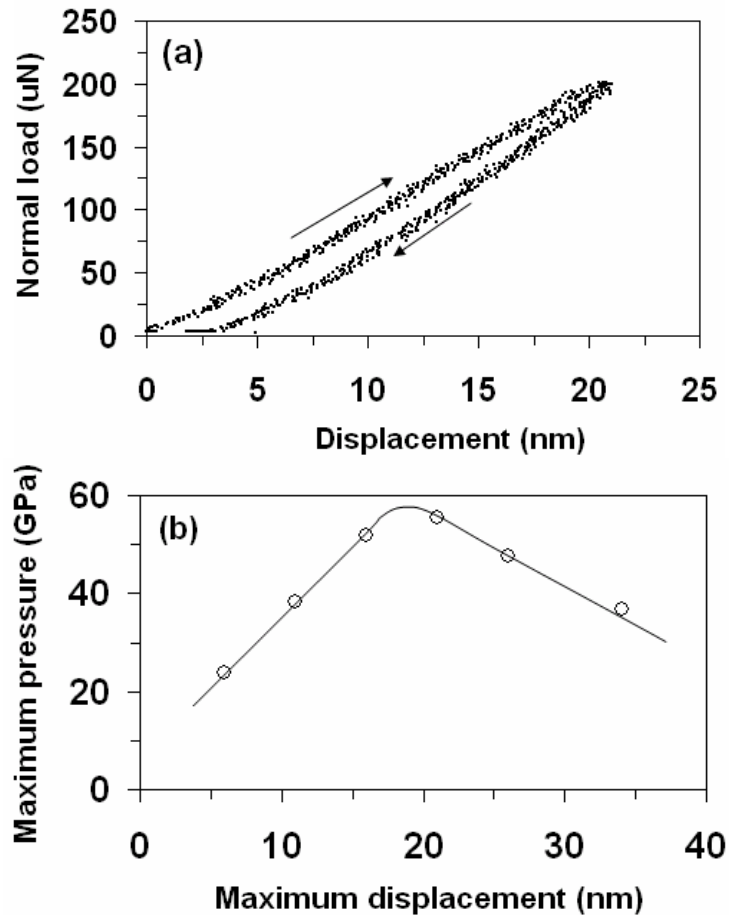


Figure 3.8 (a) Representative nano-indentation curve and (b) maximum contact pressure vs maximum displacement for a sample processed at  $\sim 120$  eV ion kinetic energy ( $-100$  V bias voltage of 25 kHz frequency) and 3 min process time.

curves, the maximum contact pressure was calculated by dividing the maximum indentation load by the projected area, determined from the tip shape function at the maximum displacement. Figure 3.8(b) shows that the variation of the maximum pressure with the maximum displacement comprises two regions, as explained in detail in Chapter 2. The peak of the maximum contact pressure represents the effective hardness of the processed material. The term effective hardness is used because the measured hardness depends on both the carbon film and substrate properties and reflects the surface resistance against plastic flow [19, 39, 49, 50].

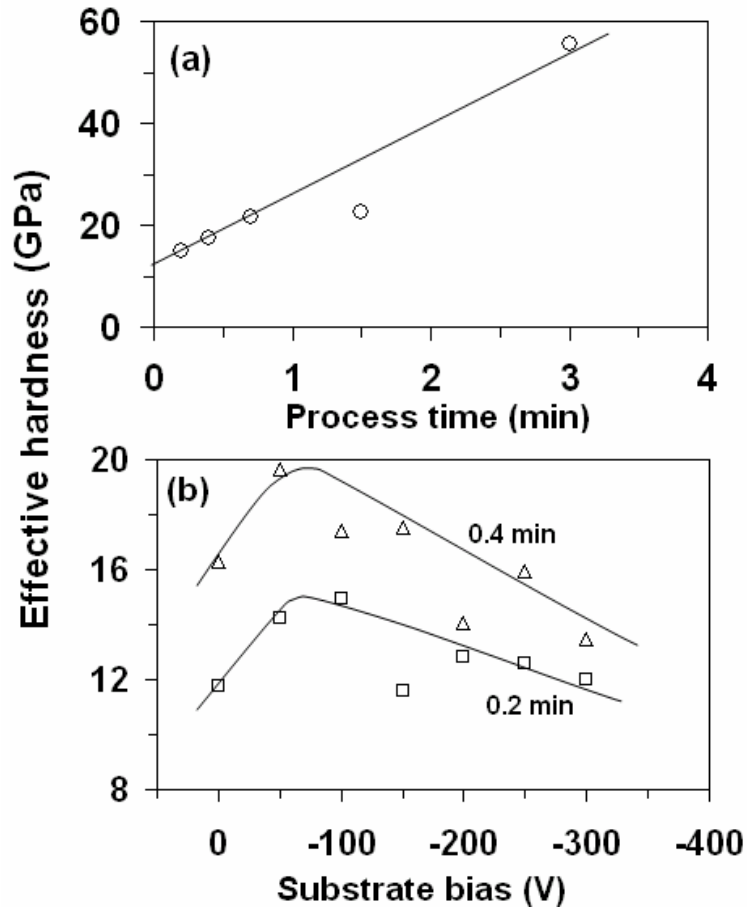


Figure 3.9 (a) Effective hardness versus process time for  $\sim 120$  eV ion kinetic energy ( $-100$  V bias voltage of 25 kHz frequency), and (b) effective hardness vs substrate bias voltage of 25 kHz frequency for 0.4 and 0.2 min process time corresponding to  $3.6$  and  $1.8 \times 10^{16}$  ions/cm<sup>2</sup> ion fluence.

The dependence of the effective hardness on process time and substrate bias is shown in Figure 3.9. For fixed ion kinetic energy ( $\sim 120$  eV), the effective hardness increased with the process time [Figure 3.9(a)]. This trend can be mostly attributed to the substrate effect, which is more significant for thinner films. For process time equal to 0.2 and 0.4 min, the highest effective hardness was obtained for bias voltage between  $-50$  and  $-100$  V [Figure 3.9(b)]; however, higher effective hardness values were produced for 0.4 than 0.2 min process time due to the substrate effect. In addition to the substrate effect,  $sp^3$  carbon hybridization may also affect the nanomechanical properties. For fixed carbon ion fluence, the  $sp^3$  fraction was found to correlate to the effective hardness

(Figures 3.6 and 3.9(b)). While high  $sp^3$  fraction results in high effective hardness, low carbon concentration due to deep penetration of high-energy carbon ions decreases the effective hardness. The trends shown in Figure 3.9(b) are manifestations of two competing effects, namely  $sp^3$  carbon hybridization and carbon-silicon intermixing.

### 3.5 SUMMARY

Ultrathin carbon films were synthesized onto silicon substrates using the FCVA technique. Carbon films with different compositions, roughness, and nanomechanical behaviors were obtained by varying the carbon ion kinetic energy (substrate bias) and ion fluence (process time). Carbon film profiles were simulated with the T-DYN code and validated by XRR measurements. XPS, AFM, and SFM analyses yielded insight into the microstructure, roughness, and nanohardness of the synthesized carbon films and mechanisms of carbon atom hybridization. Carbon films synthesized without substrate bias ( $\sim 20$  eV ion energy) were characterized by high carbon concentrations at the surface but relatively low  $sp^3$  contents, while high ion kinetic energies ( $>200$  eV) degraded the film strength and increased the surface roughness. In the case of ultrathin films ( $<5$  nm), i.e., 0.4 and 0.2 min process time, the highest  $sp^3$  content was obtained for substrate bias voltage of  $-150$  and  $-50$  V, respectively. The surface roughness was found to depend on the surface carbon concentration, and was influenced by two competing mechanisms – surface diffusion that induced surface smoothening and intense ion bombardment that caused surface damage. The effective hardness for relatively short process time (i.e., 0.2 and 0.4 min) was affected by the substrate deformation,  $sp^3$  fraction, and carbon-silicon intermixing.

## Chapter 4

### FCVA Treatment of the Magnetic Medium Surface

#### 4.1 OVERCOAT-FREE MAGNETIC MEDIUM FOR ULTRAHIGH MAGNETIC RECORDING

Magnetic recording relies on the storage of information in the form of bits in a magnetic layer (typically a Co-based alloy) of a thin-film disk [35, 38, 76-78], coated by a thin carbon film for protection against mechanical wear and corrosion. A lubricant monolayer adsorbed on the carbon film surface provides an additional barrier against corrosion and maintains low friction (adhesion) between the surfaces of the magnetic head and the hard disk. Since the data storage density increases exponentially with the decrease of the magnetic spacing, i.e., the distance between the magnetic write/read element embedded in the trailing edge of the head and the magnetic layer of the hard disk [33, 35, 38, 74, 77-79], decreasing the thickness of the carbon overcoat to less than 2 nm while preserving the corrosion resistance and mechanical/tribological properties of the surface is of paramount importance. Despite the remarkable increase in storage densities to a few hundreds of Gbit/in<sup>2</sup> [35, 38, 74, 78], it is projected that future recording densities will approach the 10 Tbit/in<sup>2</sup> level, implying a carbon film thickness of less than 1 nm. However, continuous carbon overcoats of such small thickness cannot be synthesized by traditional sputter deposition techniques. Therefore, new coating technologies must be developed for the magnetic storage density to be increased by an order of magnitude.

In this study, the near-surface region of the magnetic medium of hard disks was modified by energetic  $C^+$  ions using the FCVA method. The modification of the surface topography, structure, and nanomechanical properties of the magnetic medium by FCVA treatment under  $C^+$  plasma conditions of zero and  $-100$  V pulsed substrate bias were examined by Monte Carlo (T-DYN code) simulations, x-ray photoelectron spectroscopy (XPS), atomic force microscopy (AFM), and surface force microscopy (SFM). Representative results from these studies are presented to demonstrate that the efficacy of the FCVA technique to produce overcoat-free magnetic media with increased mechanical strength and good oxidation resistance.

#### **4.2 SPUTTER-ETCHING OF PREEXISTING CARBON OVERCOAT**

Unlubricated thin-film hard disks of diameter equal to 3.5 in. were cut into  $10 \times 10$  mm<sup>2</sup> pieces. To prevent oxidation of the magnetic medium, the hard-disk pieces were loaded onto the specimen stage of the FCVA system, and the  $\sim 4$ -nm-thick carbon overcoat was removed *in situ* by  $Ar^+$  ion sputter etching under a working pressure of  $\sim 2.4 \times 10^{-4}$  Torr. Monte Carlo simulations using the T-DYN code (version 4.0) and etch thickness measurements were used to determine the  $Ar^+$  ion etching time to completely remove the carbon overcoat.

T-DYN simulations (introduced in Chapter 3) were used to study the removal of the preexisting carbon film by  $Ar^+$  ion sputtering. All simulations were performed under the assumptions of ion impingement perpendicular to the medium surface, constant ion energy, and no  $Ar^+$  ion implantation. The surface binding energies of carbon and cobalt were set equal to 7.41 and 4.43 eV and their binding energies equal to 2.27 and 8.80 eV, respectively. These values are typical of solid-state graphite and cobalt.

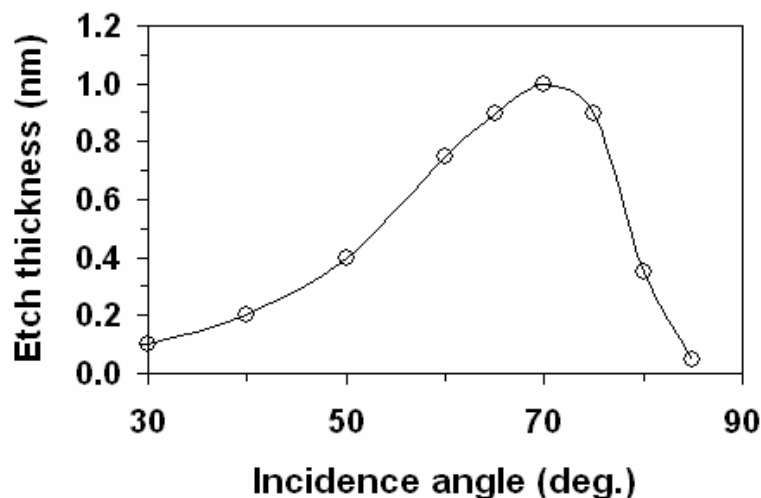


Figure 4.1 T-DYN simulation of etch thickness of graphitic carbon versus incidence angle of  $\text{Ar}^+$  ion beam (ion energy = 500 eV; ion dose =  $1 \times 10^{16}$  ions/cm<sup>2</sup>).

T-DYN simulation results of the thickness of carbon etched off by bombarding  $\text{Ar}^+$  ions as a function of incidence angle is shown in Figure 4.1 for an ion dose of  $1 \times 10^{16}$  ions/cm<sup>2</sup>. The data show that the maximum thickness of etched carbon corresponds to an incidence angle of  $\sim 70^\circ$ . Therefore, to minimize the time to remove the preexisting carbon overcoat from the hard-disk specimens, the incidence angle of the  $\text{Ar}^+$  ion beam was set at  $60^\circ$ . Surface profilometry and XPS measurements were used to confirm the removal of the  $\sim 4$ -nm-thick carbon overcoat. For 4, 6, and 8 min of  $\text{Ar}^+$  ion sputtering, the etch thickness was found equal to 3.3, 4.5, and 7.3 nm, respectively. Because of the binding energy of cobalt is less than that of carbon, a higher etching rate was observed upon the removal of the carbon overcoat. XPS results confirmed that 8 min of  $\text{Ar}^+$  ion sputter etching resulted in the complete removal of the carbon overcoat. Figures 4.2(a) and 4.2(b) show XPS survey spectra obtained before and after 8 min of  $\text{Ar}^+$  ion sputter etching, respectively. The O1s peak is attributed to the adsorption of oxygen upon the specimen exposure to the ambient. The Co2p, Cr2p, Pt4d, and Pt4f peaks and the significant intensity decrease of the C1s peak in the XPS spectrum shown in Figure

4.2(b) confirm the exposure of the magnetic medium due to the removal of the carbon overcoat. The low-intensity C1s peak seen in Figure 4.2(b) is also due to the adsorption of ambient carbon.

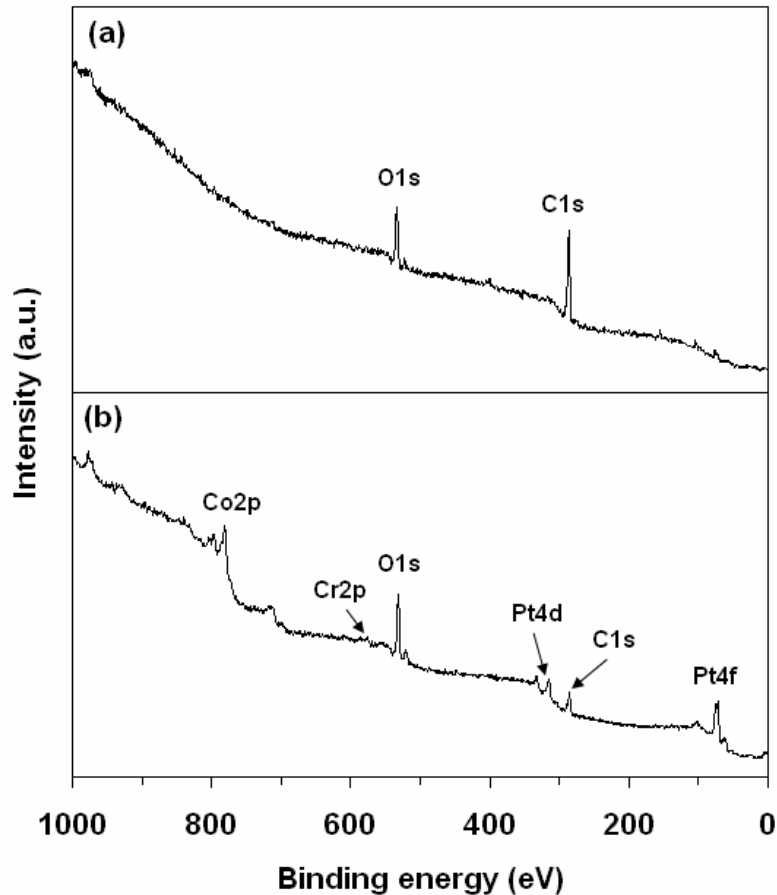


Figure 4.2 XPS spectrum of a hard-disk specimen with a  $\sim 4$ -nm-thick carbon overcoat obtained (a) before and (b) after sputter etching for 8 min with an  $\text{Ar}^+$  ion beam of  $60^\circ$  incidence angle.

### 4.3 FCVA TREATMENT OF THE MAGNETIC MEDIUM

The magnetic medium exposed under high vacuum was subjected to filtered cathodic vacuum arc (FCVA) treatment, which was introduced in Chapter 1. Two series of treatments were performed, i.e., zero and  $-100$  V pulsed substrate bias of 25 kHz frequency.

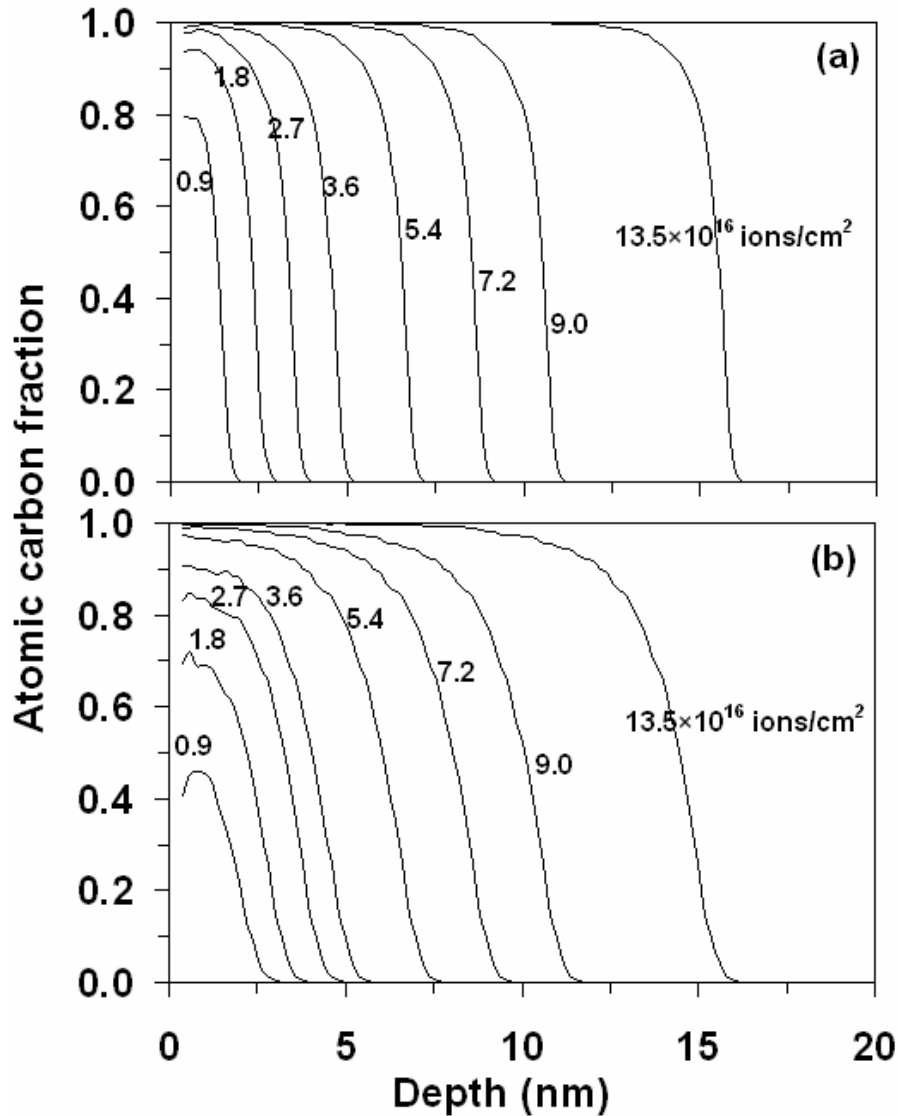


Figure 4.3 Carbon depth profiles due to  $C^+$  ion impingement perpendicular to a cobalt surface simulated with the T-DYN code for (a) 0 and (b)  $-100$  V/25 kHz pulse frequency substrate bias (ion flux  $\approx 1.5 \times 10^{15}$  ions/cm $^2$ ·s).

Figure 4.3 shows carbon depth profiles in cobalt medium obtained from the T-DYN analysis for 0 and  $-100$  V substrate bias and  $C^+$  ion dose in the range of  $(0.9\text{--}13.5) \times 10^{15}$  ions/cm $^2$  (corresponding to treatment time in the range of 6–90 s). The results shown in Figure 4.3 as well as all subsequent figures are for a  $C^+$  ion flux perpendicular to the medium surface equal to  $\sim 1.5 \times 10^{15}$  ions/cm $^2$ ·s. The impinging ion energy was set equal to the sum of the initial ion energy ( $\sim 20$  eV for zero substrate bias) and the energy due to

substrate biasing. It can be seen that substrate biasing tends to decrease the carbon fraction at the surface and increase the thickness of the implantation profile.

A mechanical stylus profilometer (3030 Surface Profiler, Dektak) with a 0.1-nm height resolution was used to measure the relative height difference between treated and untreated (covered) surface regions. Figure 4.4 shows surface profilometry results of the surface elevation versus  $C^+$  treatment time for zero and  $-100$  V substrate bias voltage. An etch thickness of 7.3 nm was subtracted from all the measurements. The very small or slightly negative values obtained for short treatment time (i.e.,  $<20$  s) are due to resputtering by energetic carbon ions, especially in the presence of substrate biasing. The surface elevation values for treatment times longer than 20 s are in fair agreement with the thickness of the carbon implantation profiles obtained from the T-DYN simulations (Figure 4.3).

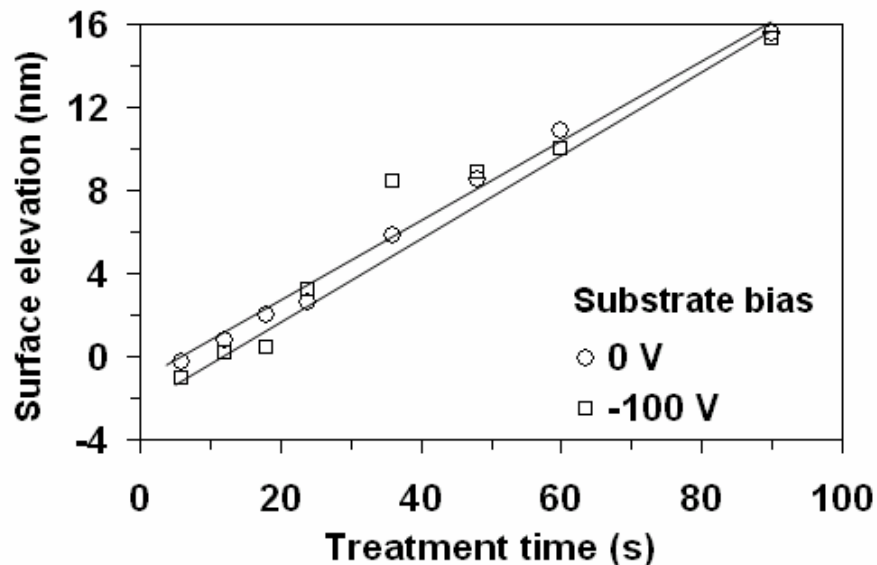


Figure 4.4 Surface elevation determined from surface profilometry measurements versus treatment time (substrate bias = 0 and  $-100$  V/25 kHz pulse frequency; ion flux  $\approx 1.5 \times 10^{15}$  ions/cm<sup>2</sup>·s).

## 4.4 SURFACE CHEMICAL ANALYSIS OF THE FCVA-TREATED MAGNETIC MEDIUM

### 4.4.1 Oxidation Behavior

Figure 4.5 shows XPS window spectra of the Co2p core-level peak obtained before and after treatment of the magnetic medium. The significant broadening of the Co2p<sub>3/2</sub> peak in the spectrum of the untreated magnetic medium [Figure 4.5(a)] is due to the oxidation of cobalt [77, 81]. The much narrower Co2p<sub>3/2</sub> peak in the spectrum of the treated magnetic medium [Figure 4.5(b)] suggests that FCVA treatment for 6 s with a C<sup>+</sup> ion dose of  $\sim 0.9 \times 10^{16}$  ions/cm<sup>2</sup> enhanced the oxidation resistance of the magnetic medium.

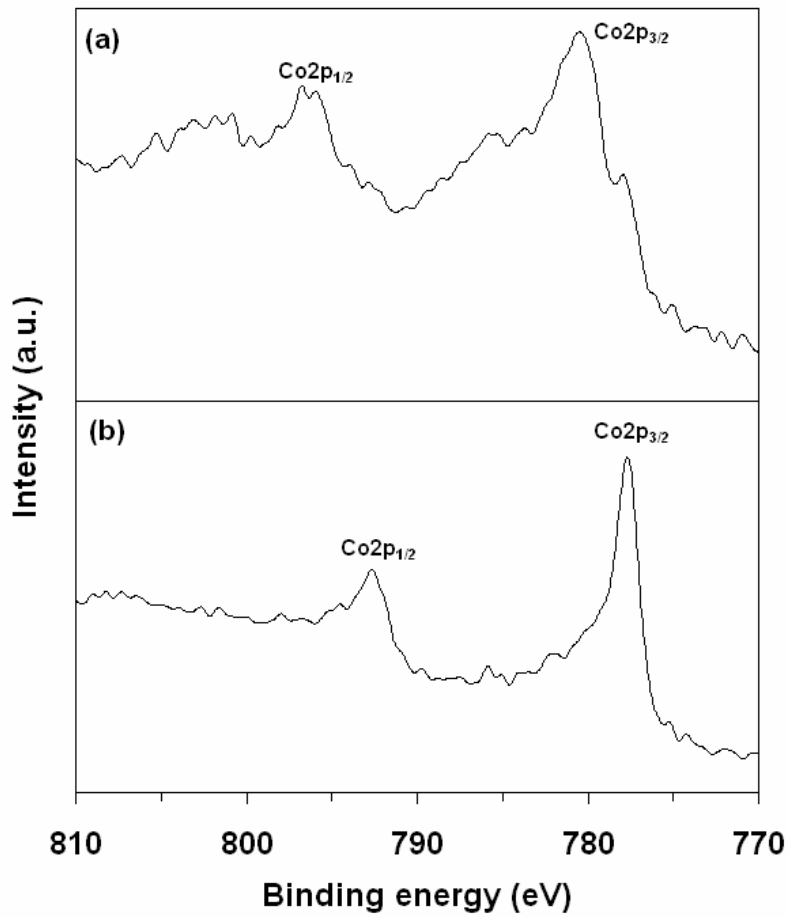


Figure 4.5 Co2p XPS spectra of magnetic medium obtained (a) before and (b) after FCVA treatment (substrate bias = 0 V; ion flux  $\approx 1.5 \times 10^{15}$  ions/cm<sup>2</sup>·s; treatment time = 6 s).

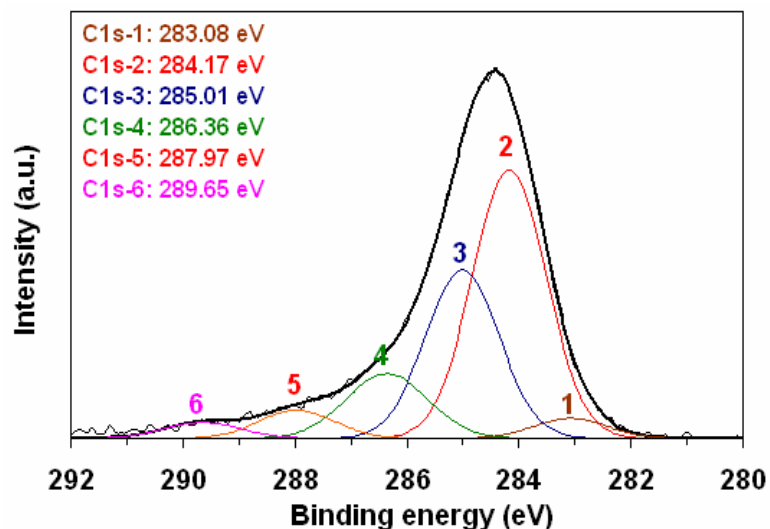


Figure 4.6 C1s XPS spectrum of FCVA-treated magnetic medium (substrate bias = 0 V; ion flux  $\approx 1.5 \times 10^{15}$  ions/cm<sup>2</sup>·s; treatment time = 12 s). The spectrum was fitted with six Gaussian distributions at characteristic binding energies after inelastic background subtraction.

#### 4.4.2 Carbon Bonding Evolution With Treatment Time

The XPS window spectrum of the C1s peak of a treated magnetic medium with characteristic Gaussian fits is shown in Figure 4.6. Although this spectrum is for a treatment time of 12 s and zero substrate bias, it is representative of the C1s XPS spectra obtained for different FCVA conditions. After inelastic background subtraction [46], the C1s spectrum was fitted with six Gaussian distributions at characteristic binding energies. The details of the deconvolution method can be found elsewhere [24]. Distributions referred to as C1s-1, C1s-2, and C1s-3 correspond to  $sp^1$ ,  $sp^2$ , and  $sp^3$  carbon hybridizations, respectively. The fraction of each type of carbon bonding was estimated from the deconvolution of the C1s XPS spectrum, as suggested in earlier studies [47, 48]. Distributions denoted by C1s-4, C1s-5, and C1s-6 are assigned to carbon atoms bonded to surface adsorbents from the ambient [20, 24] and hereafter will be referred to as

satellite peaks. Thus, the sum of the satellite peak areas indicates the fraction of carbon bonding with surface adsorbents.

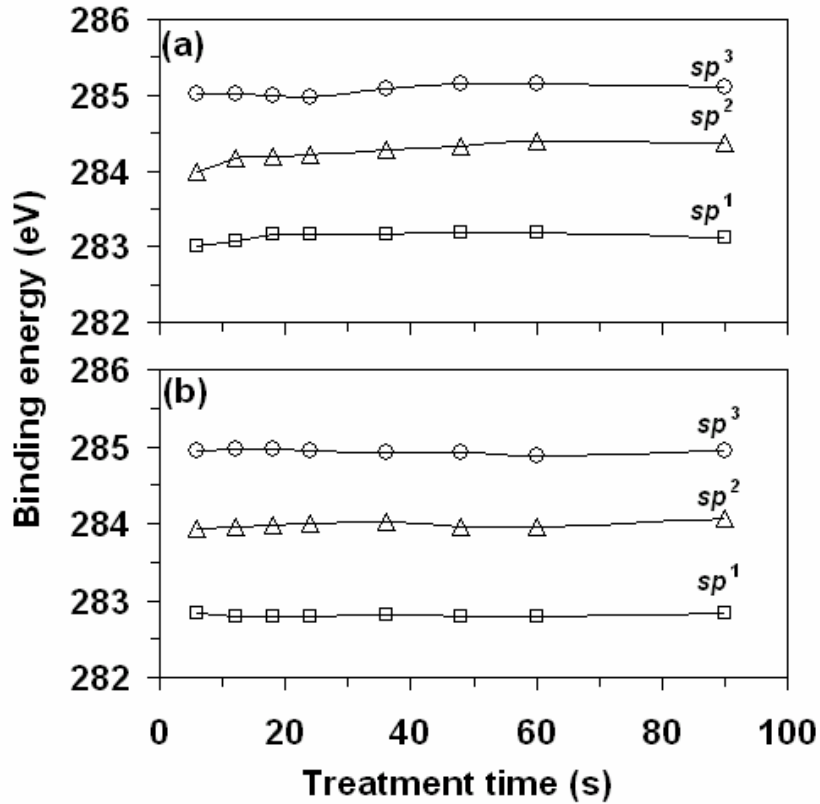


Figure 4.7 Binding energies of  $sp^1$ ,  $sp^2$ , and  $sp^3$  Gaussian fits to C1s XPS spectra versus treatment time for (a) 0 and (b) -100 V/25 kHz pulse frequency substrate bias (ion flux  $\approx 1.5 \times 10^{15}$  ions/cm<sup>2</sup>·s).

The binding energy and the fraction of  $sp^1$ ,  $sp^2$ , and  $sp^3$  carbon hybridizations versus treatment time are shown in Figure 4.7 and 4.8, respectively. It has been reported that the binding energies of carbon species depend on the stress state [24]. The relatively constant  $sp^1$ ,  $sp^2$ , and  $sp^3$  binding energy levels in Figure 4.7 indicate a constant stress in the carbon species for treatment time in the range of 6–90 s. Therefore, the nanomechanical properties of the FCVA-treated magnetic medium (presented below) were not affected by internal stress variations. The lower binding energies for -100 V substrate bias [Figure 4.7(b)] compared to those for zero substrate bias [Figure 4.7(a)] may be attributed to the higher compressive stress caused by the higher  $C^+$  ion energy in the treatments involving

substrate biasing [24]. Figure 4.8 shows the variation of  $sp^1$ ,  $sp^2$ ,  $sp^3$ , and satellite fractions with treatment time. For both zero and  $-100$  V substrate bias, the curves of the  $sp^2$  and  $sp^3$  fractions cross over at a treatment time of  $\sim 24$  s, in qualitative agreement with the low  $sp^3$  fraction reported for shallow implantation thickness [33].

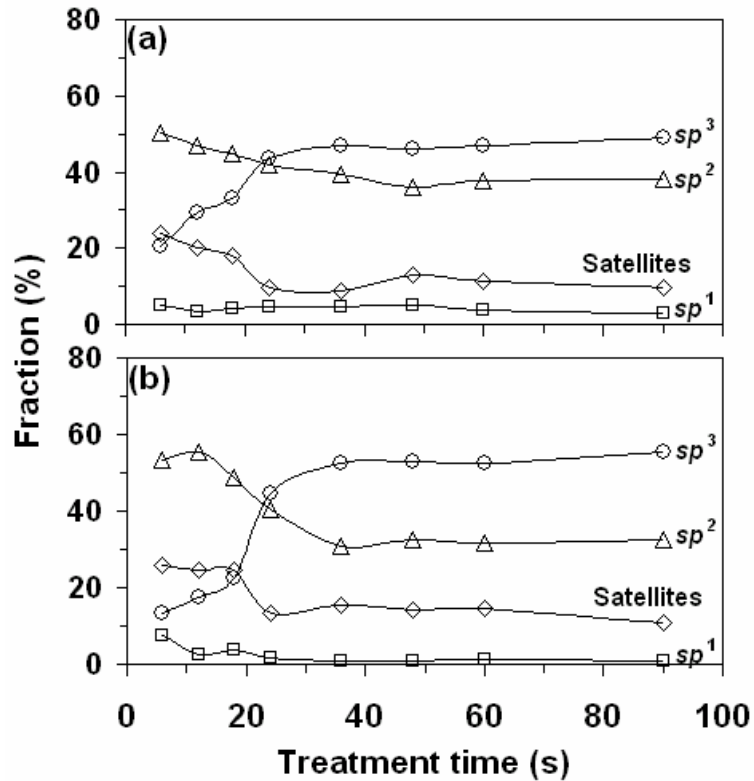


Figure 4.8 Fractions of carbon constituents obtained from the deconvoluted  $C1s$  XPS spectra versus treatment time for (a) 0 and (b)  $-100$  V/25 kHz pulse frequency substrate bias (ion flux  $\approx 1.5 \times 10^{15}$  ions/cm<sup>2</sup>·s).

According to the subplantation model, the energetic carbon ions penetrate into the substrate up to some depth [26-28] resulting in subsurface densification which is conducive to  $sp^3$  hybridization [27, 70]. Thus,  $sp^3$  hybridization depends on the formation of a carbon-rich surface layer. However, carbon hybridization in FCVA treatment differs from that in conventional implantation because the low ion dose affects significantly the near-surface carbon concentration. While zero substrate bias yielded a higher  $sp^3$  fraction for short treatment time (e.g., 6 s), an opposite trend was observed for treatments longer

than ~24 s. This may be attributed to the combined effects of recoil implantation and deeper ion penetration under substrate biasing conditions. The higher satellite fractions for shorter treatment times are attributed to the existence of more surface adsorption sites for ambient carbon adsorbents due to the lower implantation dose [70].

#### **4.5 SURFACE ROUGHNESS OF FCVA-TREATED MAGNETIC MEDIUM**

The root-mean-square (rms) roughness was calculated from  $1 \times 1 \mu\text{m}^2$  surface images obtained with an AFM (Dimension 3100, Veeco Digital Instruments) operated in the tapping mode, using a drive frequency of 259.332 kHz and scan rate of 2 Hz. Figure 4.9 shows the rms roughness of the magnetic medium as a function of treatment time. The rms roughness of the carbon-coated hard disk was equal to ~0.19 nm. The roughness for zero treatment time corresponds to the magnetic medium surface exposed after 8 min of  $\text{Ar}^+$  ion sputter etching. Although  $\text{Ar}^+$  ion etching induced significant surface roughening (rms  $\approx 0.72$  nm), FCVA treatment for 12 s restored the original surface smoothness (rms  $\approx 0.2$  nm). It was reported (in Chapter 3) that FCVA treatment of smooth Si wafers with carbon plasma results in the deposition of ultrathin carbon films of rms  $< 0.1$  nm. Therefore, the ~0.2 nm roughness values shown in Figure 4.9 are attributed to the rougher morphology of the magnetic medium produced from  $\text{Ar}^+$  ion sputter etching. Figure 4.9 also shows that substrate pulsed biasing at  $-100$  V resulted in smoother topographies, presumably due to the enhancement of resputtering that promoted surface smoothing. Carbonaceous adsorbents from the ambient might have also contributed to surface smoothing, particularly for short treatment times, resulting in higher fractions of carbon bonding attributed to ambient adsorbents (satellites), as shown in Figure 4.8. Thus, the lowest surface roughness obtained for 12-s treatment time may be

associated with smoothing primarily due to resputtering and secondarily due to adsorption of carbonaceous substances. The effect of both mechanisms decreased with the increase of the treatment time due to the formation of a more etch-resistant carbon-rich layer of slightly increased roughness for longer treatment times.

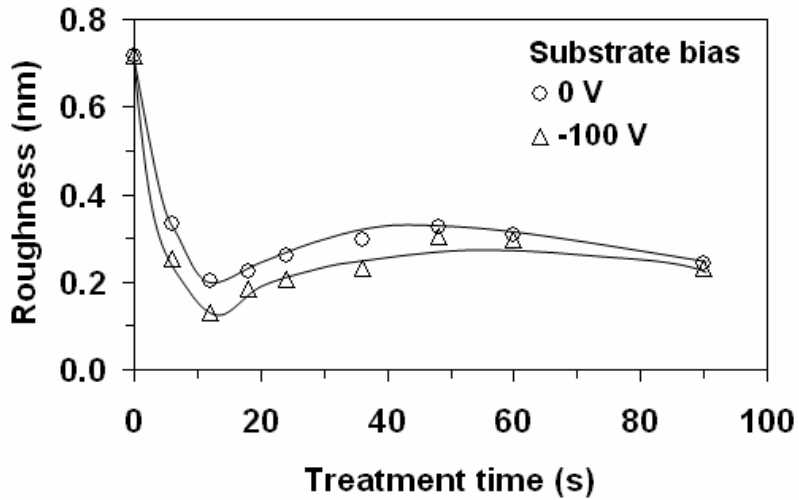


Figure 4.9 Surface roughness versus treatment time (substrate bias = 0 and -100 V/25 kHz pulse frequency; ion flux  $\approx 1.5 \times 10^{15}$  ions/cm<sup>2</sup>·s).

#### 4.6 NANOMECHANICAL PROPERTIES OF FCVA-TREATED MAGNETIC MEDIUM

The nanomechanical properties of the FCVA-modified magnetic medium were evaluated with a SFM consisting of an atomic force microscope (Nanoscope II, Digital Instruments) retrofitted with a capacitive force transducer (Triboscope, Hysitron). All of the SFM experiments were performed with a pyramidal diamond tip with an apex nominal radius of  $\sim 75$  nm. The tip was engaged with the specimen surface under a normal force of 3  $\mu$ N. A triangular loading function with loading and unloading times equal to 2 s was used in all indentations. The shape function of the diamond tip (a polynomial function of the indentation depth) was determined from indentations performed on an ultrasmooth fused quartz sample of in-plane elastic modulus  $E/(1-\nu^2) =$

69.6 GPa, where  $E$  is the elastic modulus and  $\nu$  is the Poisson's ratio. The maximum contact pressure was obtained as the ratio of the applied maximum load to the projected contact area, given by the polynomial tip-shape function at the corresponding indentation depth. The in-plane elastic modulus (referred to as the reduced modulus) was calculated from the stiffness estimated at the maximum tip-displacement point of the unloading curve [49, 50].

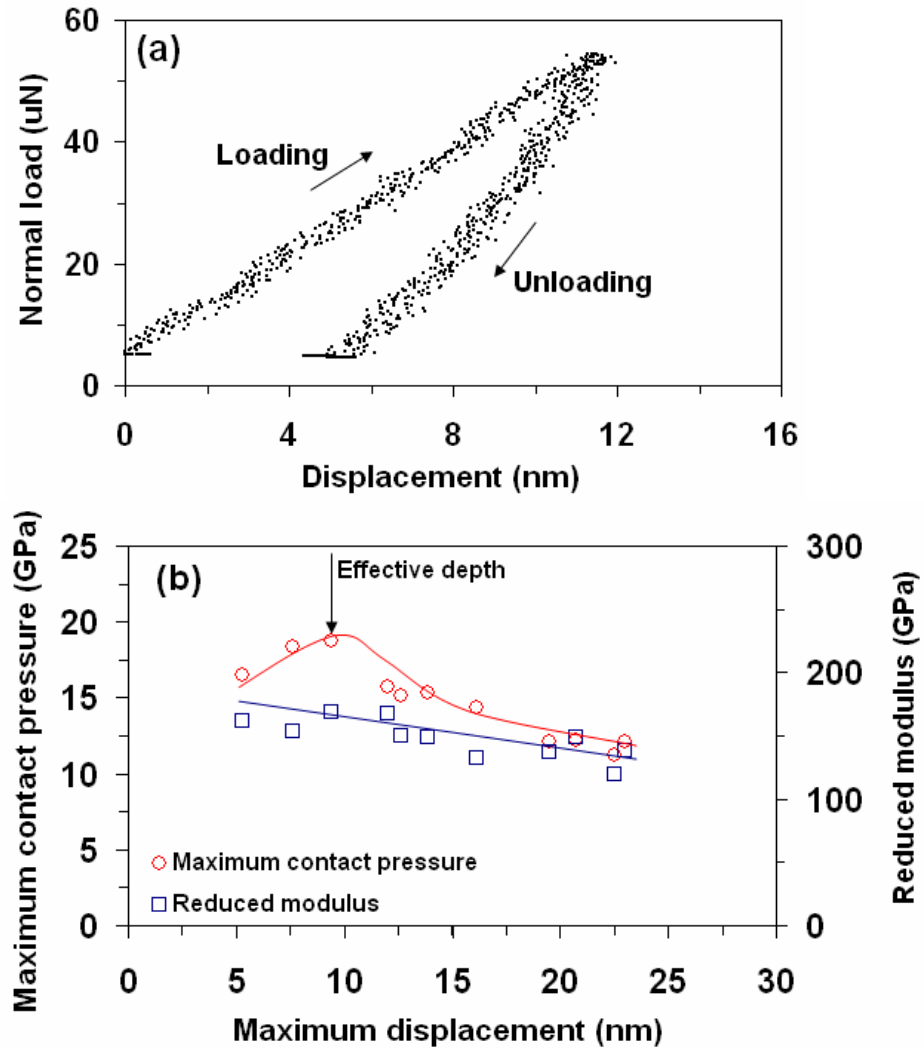


Figure 4.10 (a) Nanoindentation load versus displacement response and (b) maximum contact pressure and reduced modulus versus maximum displacement of FCVA-treated magnetic medium (substrate bias = 0 V; ion flux  $\approx 1.5 \times 10^{15}$  ions/cm<sup>2</sup>·s; treatment time = 48 s).

Figure 4.10 shows representative results of the nanomechanical behavior of the magnetic medium treated by FCVA for 48 s without substrate biasing. The nanoindentation load-displacement response [e.g., Figure 4.10(a)] was used to determine the maximum contact pressure and reduced modulus as functions of the maximum tip displacement [Figure 4.10(b)]. The initial increase of the maximum contact pressure with the maximum displacement is attributed to the gradual evolution of plasticity under the tip [49, 50]. After reaching a peak value, the maximum contact pressure decreased with the increase of the maximum displacement due to the much softer and compliant magnetic medium and other sublayers comprising the hard disk. By definition, the peak value of the maximum contact pressure corresponds to the “effective” hardness, which reflects the material resistance to plastic deformation during indentation loading [49, 51]. The effective depth is defined as the maximum displacement corresponding to the effective hardness. The reduced modulus exhibited a slight decrease with the increase of the maximum displacement above the effective depth. This is attributed to the greater contribution of the more compliant magnetic medium and other sublayers to the elastic contact deformation of the hard disk.

Figure 4.11 shows representative results of the nanomechanical properties of the FCVA-treated magnetic medium for zero and  $-100$  V substrate bias. The nanomechanical properties for short treatment time (low ion dose) are close to those of the unmodified magnetic medium. The increase in the effective hardness with treatment time [Figure 4.11(a)] may be related to the greater amount of implanted carbon that enhanced the surface deformation resistance of the magnetic medium. The higher hardness for  $-100$  V substrate bias is due to the stronger effect of energetic  $C^+$  ion bombardment that resulted

in higher  $sp^3$  content [Figure 4.8] and, presumably, more surface densification that increased the penetration resistance of the magnetic medium, as indicated by the decrease in the effective depth [Figure 4.11(c)]. However, substrate biasing and treatment time exhibited secondary effects on the reduced elastic modulus.

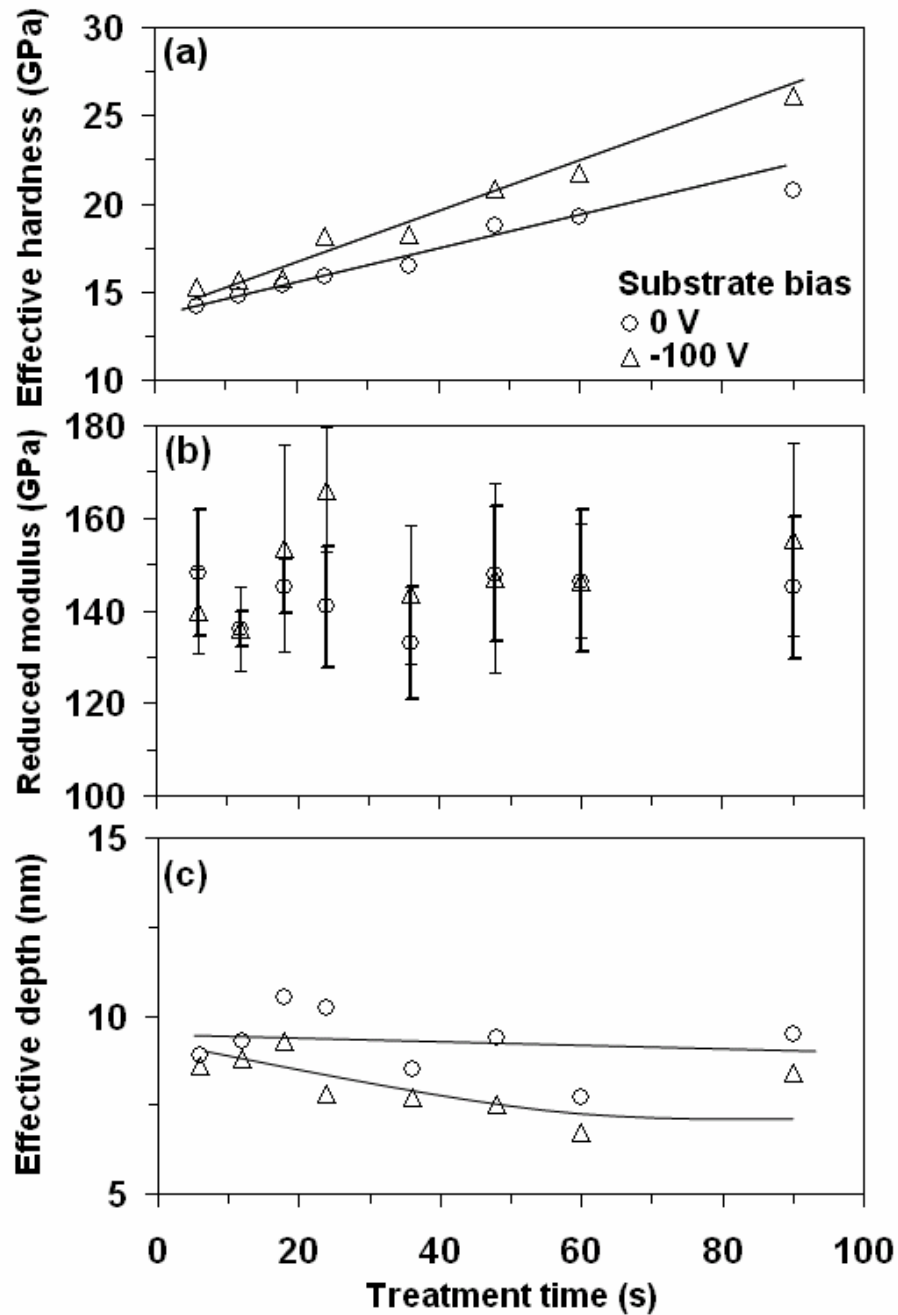


Figure 4.11 (a) Effective hardness, (b) reduced modulus, and (c) effective depth versus treatment time of FCVA-treated magnetic medium (substrate bias = 0 and -100 V/25 kHz pulse frequency; ion flux  $\approx 1.5 \times 10^{15}$  ions/cm<sup>2</sup>·s).

## Chapter 5

# Nanomechanical Response of Single-Crystal Cu-Al-Ni Shape-Memory Alloy

### 5.1 PHASE TRANSFORMATION OF Cu-Al-Ni SHAPE-MEMORY ALLOY

Shape-memory alloys (SMA) have become candidate materials for dynamic microsystems because of demonstrated very large reversible strains (typically ~8%) and controllable mechanical response due to phase transformations that may include multiple phases, such as austenite and martensite of ordered microstructures. Austenite-to-martensite phase transformation in SMA may result from a temperature decrease or an increase in applied stress. Since austenite can transform to different martensite phases, depending on the temperature and applied stress, it is often referred to as the parent phase, whereas the various types of martensite are known as the derivative phases. Martensite-to-martensite phase transformation may also occur under certain conditions of stress and temperature.

Stress-strain responses of various SMA have been studied at different temperatures [82-89]. Among all SMA, single-crystal Cu-Al-Ni exhibits the largest strain recovery (~17%), in addition to high thermal and electrical conductivity and temperature-dependent damping ratio [82, 83, 90]. Materials with high damping ratio are desirable because they can reduce vibrations and noise in high-speed devices containing dynamic contacts. The large strain recovery and adjustable damping ratio are due to four intrinsic martensite phases ( $\alpha'_1$ ,  $\beta'_1$ ,  $\beta''_1$ , and  $\gamma'_1$ ) forming from the parent austenite  $\beta_1$  phase

under different stress and temperature conditions. For example, excessive deformation of the parent  $\beta_1$  phase leads to the formation of  $\beta_1'$  martensite [86, 91-93],  $\gamma_1'$  can be obtained by cooling stress-free  $\beta_1$  [93-96], and  $\beta_1''$  and  $\alpha_1'$  martensitic phases can be produced by stretching the  $\gamma_1'$  phase [83, 84, 86].

## **5.2 PROCESSING AND CHARACTERIZATION OF SINGLE-CRYSTAL Cu-Al-Ni SHAPE-MEMORY ALLOY**

### **5.2.1 Fabrication of Specimens**

Cylinders of diameter equal to 0.635 cm were fabricated from a molten pool of 82% Cu, 14Al, and 4Ni (wt%) by the Czochralski method. After heating to  $\sim 870$  °C, the cylinders were quenched to room temperature to acquire a cubic austenitic microstructure. The cylindrical samples were cut into wires of 0.018 inches in diameter and plates of 0.02 inches in thickness by electrical discharge machining for tensile and nanoindentation testing, respectively. The wire samples were not surface treated, while the plate sample surfaces were first polished with SiC abrasive paper of progressively finer grit size and then with an Al<sub>2</sub>O<sub>3</sub> abrasive paper with grit size equal to 30 and 1  $\mu\text{m}$ .

Phase transformation temperatures were determined from differential scanning calorimetry (DSC) measurements obtained in the range of -50 to 100 °C by heating and cooling a 9.5 mg sample at a rate of 0.5 °C/min. The austenite (*A*) and martensite (*M*) start and finish temperatures were determined to be  $A_s = -36$  °C,  $A_f = -31$  °C,  $M_s = -38$  °C, and  $M_f = -43$  °C (where subscripts *s* and *f* refer to *start* and *finish*). These phase transformation temperatures are in good agreement with experimental results reported in earlier studies [91, 93, 97, 98].

### 5.2.2 Chemical Composition Analysis by Rutherford Backscattering and Particle-Induced X-ray Emission

The chemical composition of the Cu-Al-Ni specimens was determined by Rutherford backscattering spectroscopy (RBS) and particle-induced X-ray emission (PIXE), using energetic  $\text{He}^+$  ion beams generated from a 2.5 MeV electrostatic accelerator. Two silicon detectors oriented at  $165^\circ$  with respect to the incident  $\text{He}^+$  beam were used to collect the backscattered ions. X-ray emission was detected by a Li-drifted silicon detector with two Be windows. Both RBS and PIXE analyses were performed without tilting the specimen.

Figure 5.1(a) shows the PIXE spectrum of the synthesized Cu-Al-Ni alloy. By dividing the area under the Ni-K $\alpha$  peak by the area under the Cu-K $\alpha$  peak, the Ni/Cu atomic ratio was found equal to ~6%. A negligibly small amount of Cr was detected in the specimen. The Ag peak is attributed to the adhesive medium. The Cu escape peak observed to be 1.74 keV below the Cu-K $\alpha$  peak is a computational artifact introduced in the process of eliminating the silicon detector noise. Figure 5.1(b) shows good agreement between experimental and simulation RBS results. The very close positions of the Ni and Cu signals in the RBS spectrum complicate the identification. By dividing the decrease in the Al signal by the sum of the decrease in the Cu and Ni signals and multiplying this ratio by the atomic number factor, the Al/(Cu+Ni) atomic ratio was determined to be ~40%. The simulation result corresponds to  $\text{Cu}_{1.0}\text{Al}_{0.42}\text{Ni}_{0.05}$ , which is close to the composition of the molten pool used to fabricate the alloy cylinders. The small discrepancy between experimental and simulation results for the Cu and Ni drop position is most likely due to the presence of surface oxides.

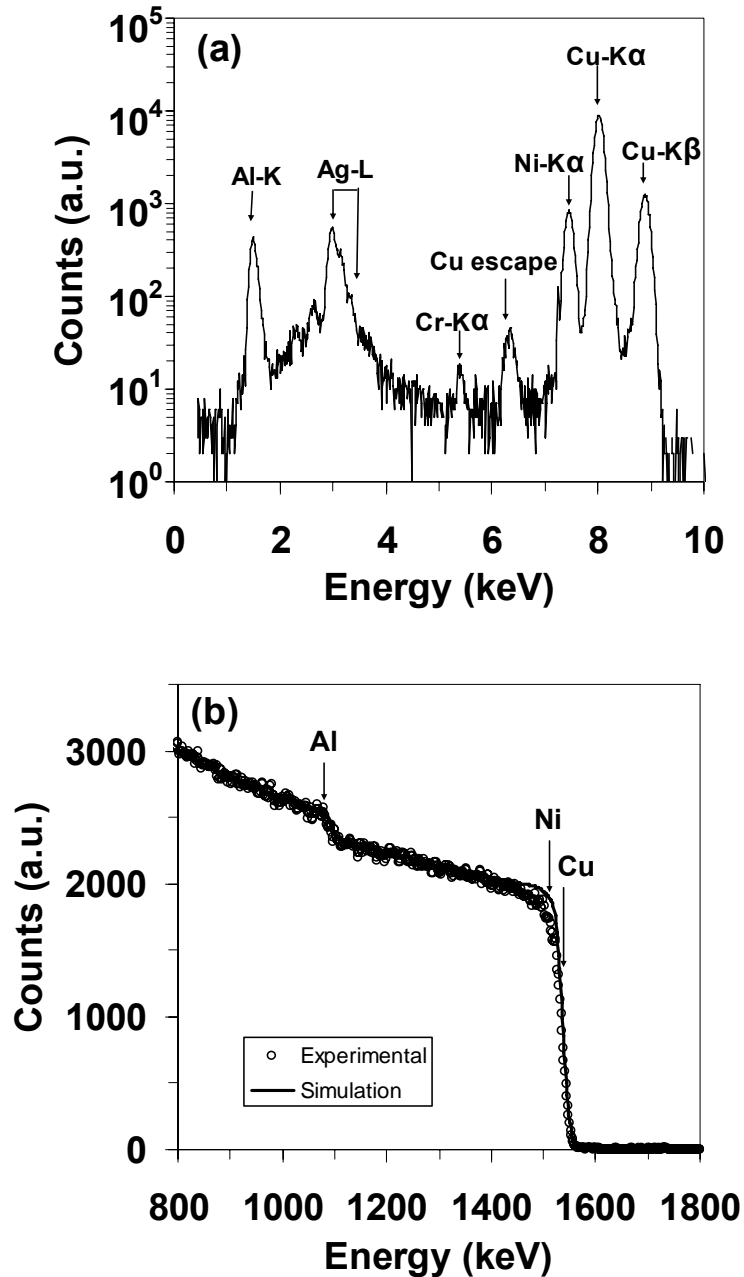


Figure 5.1 (a) PIXE and (b) RBS spectra of single-crystal Cu-Al-Ni alloy.

### 5.2.3 Microstructure Characterization by Transmission Electron Microscopy (TEM)

Transmission electron microscope (TEM) images and selected area diffraction (SAD) patterns were obtained with a JEOL 200CX analytic electron microscope with a side-entry double-tilt goniometer stage operated at 200 kV. The TEM sample was first thinned down to a thickness of  $\sim 20 \mu\text{m}$  by sequential sanding, grinding, and dimpling,

and then ion milled with 5 keV Ar<sup>+</sup> ion beam at an angle of 6° with respect to the specimen surface from both sides for electron transparency.

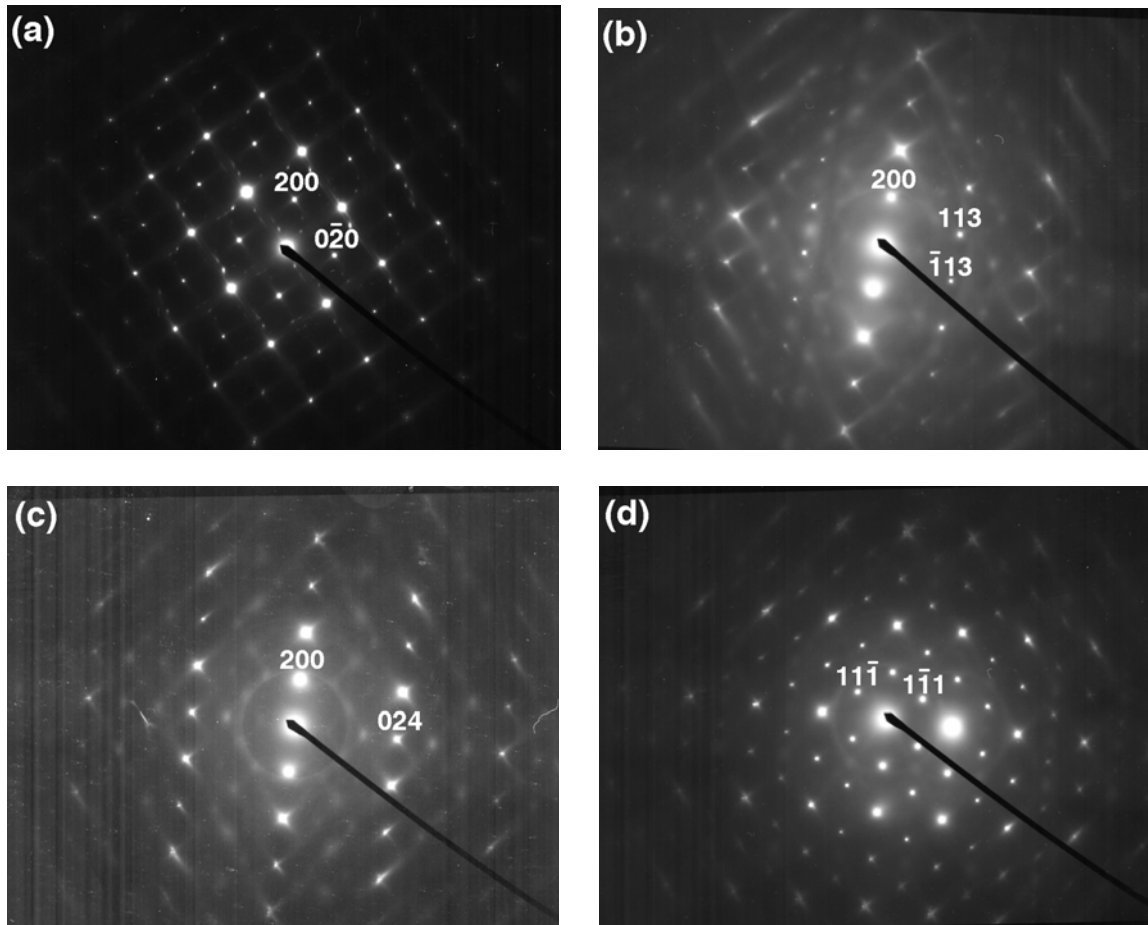


Figure 5.2 TEM selected area diffraction patterns for zone axis (a)  $[001]$ , (b)  $[03\bar{1}]$ , (c)  $[0\bar{2}1]$ , and (d)  $[011]$ .

The alloy microstructure was determined from SAD patterns with a zone axis in the  $[001]$ ,  $[03\bar{1}]$ ,  $[0\bar{2}1]$ , and  $[011]$  directions, shown in Figure 5.2. The SAD patterns indicated the formation of  $\text{Cu}_3\text{Al}$ , i.e.,  $\text{Fe}_3\text{Al}$ -type  $\text{DO}_3$ -structure [99, 100]. It is presumed that some Cu atoms in the lattice structure were randomly replaced by Ni atoms [84]. The dark-field TEM image shown in Figure 5.3(a) demonstrates the formation of numerous anti-phase boundaries (APB) with complex patterns. High-density APB have also been

observed in the  $\{111\}$  and  $\{113\}$  planes and have been classified as  $a/2 \langle 100 \rangle$  type [97, 101]. Figure 5.3(b) shows the formation of closed-loop APB of density much less than those shown in Figure 5.3(a). These closed-loop APB have been classified as  $a/4 \langle 111 \rangle$  type [97, 101-103]. It is believed that both open-structure and closed-loop APB result from the coalescence of excess vacancies generated during quenching [97, 103], which tend to form prismatic loops, especially  $a/2 \langle 100 \rangle$  type APB. In addition, Figure 5.3(b) shows a tweed microstructure which is similar to a dense array of incommensurate shear strain of  $\{110\} \langle \bar{1}\bar{1}0 \rangle$  type [104]. The dark-field TEM image shown in Figure 5.3(c) provides a close-up view of the tweed structure resulting from strain modulations. Both the APB shape and the strain modulations can be associated with the high elastic anisotropy of the  $\beta_1$  parent phase,  $2C_{44}/(C_{11}-C_{22}) \approx 12$ , which causes the single crystal to be soft in the  $\langle 001 \rangle$  direction and hard in the  $\langle 111 \rangle$  direction [82, 91, 94, 97]. APB provide nucleation sites for precipitates and inhibit the movement of phase transformation interfaces, hence restricting martensite transformation [105]. The density and orientation of APB exhibit subtle effects on the macroscopic mechanical response because APB (as any other defect) may locally affect the formation of certain type martensite variants [89, 106].

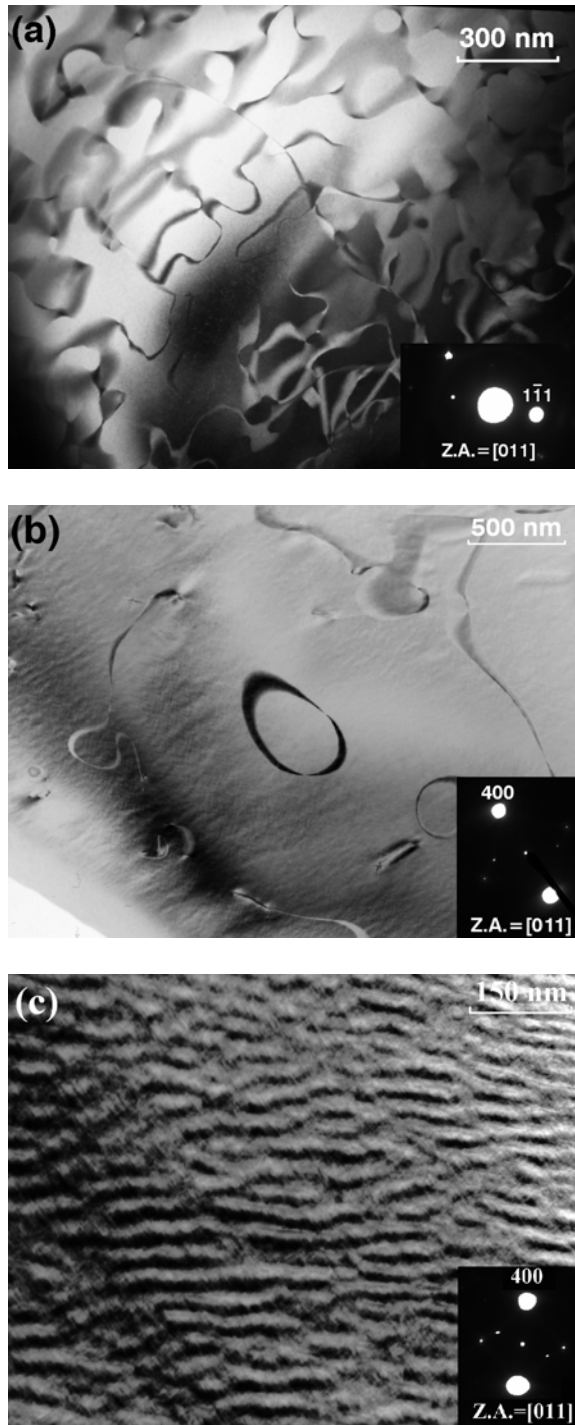


Figure 5.3 (a) Dark-field TEM image obtained under two-beam condition of [011] zone axis and  $(1\bar{1}1)$  imaging beam showing anti-phase boundaries with different patterns, (b) bright-field TEM image obtained by tilting the sample from the [011] zone axis to the (400) plane axis showing closed-loop anti-phase boundaries and strain modulation manifested by a tweed microstructure, and (c) dark-field TEM image from the [011] zone axis to the (400) plane axis showing the tweed microstructure.

## 5.3 NANOSCALE PSEUDOELASTICITY DUE TO CYCLIC INDENTATION

### 5.3.1 Reference Tensile Test

Stress-strain results from cyclic tensile tests are presented first to establish a reference for comparison with cyclic nanoindentation results, as tension and compression are considered roughly symmetric in inducing phase transformation. Strain- and temperature-control experiments were performed with a custom-made tension apparatus. A temperature resolution of about  $\pm 1^\circ\text{C}$  was achieved by using an electrical heating stage and a cold nitrogen gas regulator.

Tensile tests performed by loading austenitic Cu-Al-Ni wires in the [001] direction at room temperature yielded fully reversible strains up to 10% that are attributed to  $\beta_1 \rightarrow \beta'_1$  phase transformation. However, a very different deformation behavior was observed at  $-30^\circ\text{C}$ , i.e., close to  $A_f$ . Figure 5.4 shows tensile stress ( $\sigma$ ) versus strain ( $\varepsilon$ ) curves for four consecutive loading cycles. In the first cycle, the specimen was deformed up to point A and then unloaded to point B to produce a residual strain of 4.3%. Initial loading up to point A resulted in  $\beta_1 \rightarrow \gamma'_1$  phase transformation and, probably, formation of some intermediate  $\beta'_1$  martensite phase [107]. The external stress provided the driving force to produce a martensitic microstructure from austenite and to reduce the crystallographic symmetry [108]. However, reverse phase transformation ( $\gamma'_1 \rightarrow \beta_1$ ) did not occur upon unloading from A to B as evidenced by the significantly higher slope of the subsequent loading path. It is presumed that the low temperature inhibited the movement of the austenite-martensite interfaces, yielding a microstructure consisting of pure  $\gamma'_1$  martensite (point B) [107]. All three subsequent loading cycles (i.e., BCDB,

BCEB, and BCFB) demonstrated a pseudoelastic behavior attributed to fully reversible  $\gamma'_1 \rightarrow \beta_1''$  and  $\beta_1'' \rightarrow \gamma'_1$  transformations commencing at stress levels above 320 MPa (i.e., points D, E, and F) and below 100 MPa, respectively. The removal of the external stress caused the microstructure to reverse to that corresponding to point B in order to minimize the free energy. This produced a large hysteresis area representing the energy dissipated by phase transformation. A comparison of the loading slopes of the pseudoelastic and first-cycle responses shows that the elastic modulus of the microstructure consisting of the  $\gamma'_1$  phase is significantly higher than that of the original austenitic ( $\beta_1$ ) microstructure.

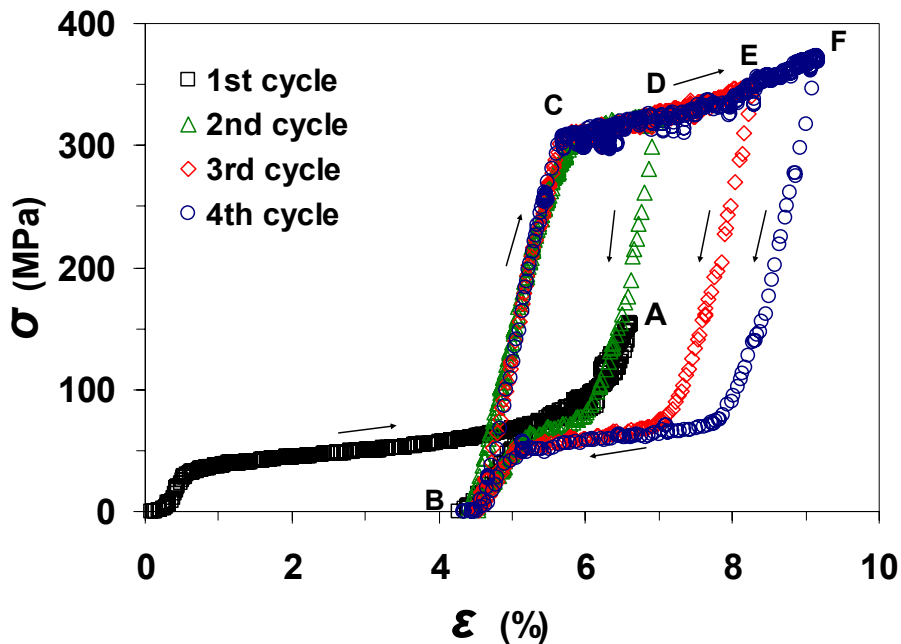


Figure 5.4 Stress-strain response of single-crystal Cu-Al-Ni alloy at  $-30^{\circ}\text{C}$  due to cyclic tensile loading. The first cycle consists of loading up to point A and then unloading to point B. All three consecutive loading cycles begin and end at point B, attaining their corresponding maximum stresses at points D, E and F. These cycles demonstrate the occurrence of a stable pseudoelastic behavior after the first cycle (training period). The arrows indicate the loading and unloading paths of each stress-strain cycle.

### 5.3.2 Correlation of Macroscale and Nanoscale Deformation Behaviors

Nanoindentation experiments were performed with the SFM apparatus introduced in Chapter 2. All nanoindentations were made with a Berkovich diamond tip of nominal radius of curvature equal to  $\sim 290$  nm. A triangular loading function with loading and unloading rates both equal to  $10 \mu\text{N/s}$  was used in all the nanoindentations.

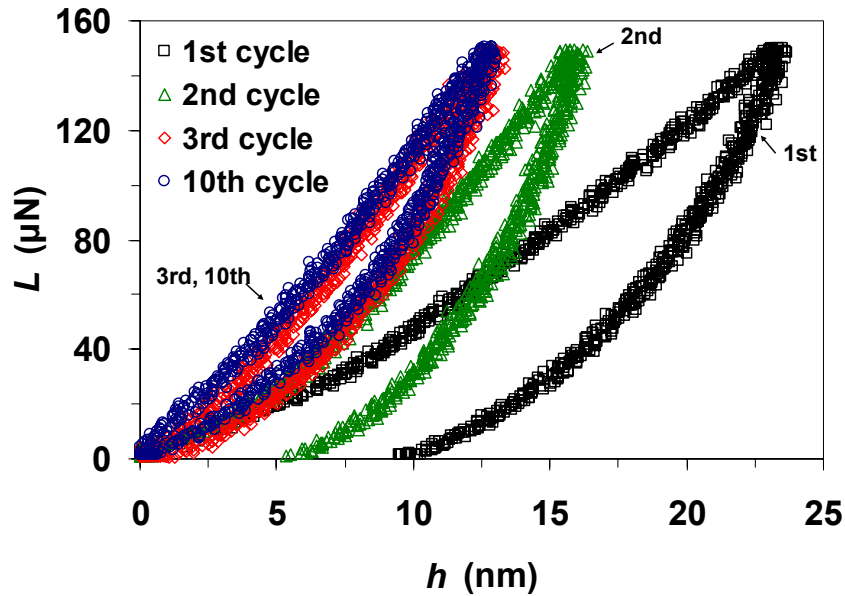


Figure 5.5 Nanoindentation curves of single-crystal Cu-Al-Ni alloy at room temperature illustrating a stable pseudoelastic behavior after three nanoindentation cycles (training period) for a maximum load of  $150 \mu\text{N}$ .

Unlike macroscopic tensile tests, nanoindentation produces a location-dependent stress gradient in the vicinity of the penetrating tip. It was found that fully reversed transformation to the austenite parent phase of Cu-Al-Ni did not occur during the first nanoindentation cycle. However, a pseudoelastic response emerged after a certain number of nanoindentation cycles (training period). Figure 5.5 shows the contact load  $L$  versus tip displacement  $h$  response of austenitic Cu-Al-Ni indented in the  $[001]$  direction at room temperature for  $L_{\text{max}} = 150 \mu\text{N}$ . It can be seen that a steady-state pseudoelastic behavior was attained after three consecutive cycles. Further cyclic indentation yielded overlapping load hystereses. The nanoindentation cycles (training period) for attaining a

stable pseudoelastic behavior increased with the maximum contact load (e.g., five cycles for  $L_{\max} = 300 \mu\text{N}$ ). It is also shown that during the training period the hysteresis area decreased, while the elastic stiffness (reflected by the slope of the unloading curve at  $L_{\max}$ ) increased as the material approached a pseudoelastic state. Stable pseudoelastic behavior was obtained for  $L_{\max}$  in the range of 50-450  $\mu\text{N}$ .

To compare the macroscale and nanoscale deformation behaviors, the nanoindentation force and displacement data were converted to mean stress ( $\sigma_m$ ) and representative strain ( $\varepsilon_r$ ), respectively. The mean stress was calculated by dividing the contact load by the corresponding contact area. To determine the contact area as a function of the tip displacement (contact depth), the Berkovich tip was calibrated by performing indentations on a standard fused quartz sample. This procedure led to the determination of the contact area as a polynomial function of contact depth [109]. The apex of the indenter tip was approximated by a sphere, and the representative strain was obtained as  $\varepsilon_r = 0.2 a/R$ , where  $R$  is the tip-apex radius of curvature and  $a$  is the radius of the contact area corresponding to a certain load (depth) [110]. For a relatively blunt indenter, such as a Berkovich tip with included angle of  $\sim 143^\circ$ , the indentation is controlled by the apex of the spherical tip up to a contact depth on the order of the tip radius. Since the contact depth was less than the nominal tip radius (290 nm),  $\varepsilon_r$  was determined under the assumption of circular impressions produced by a spherical tip of radius equal to 290 nm.

Figure 5.6 shows stress-strain responses derived from cyclic nanoindentation experiments. Data for displacements less than 5 nm are not shown because accurate estimates of the contact area function could not be obtained for such small contact depths.

The effect of the high stress gradients in the vicinity of the tip on the transformation of the austenite phase is analogous to lowering the temperature [82]. Therefore, the behavior

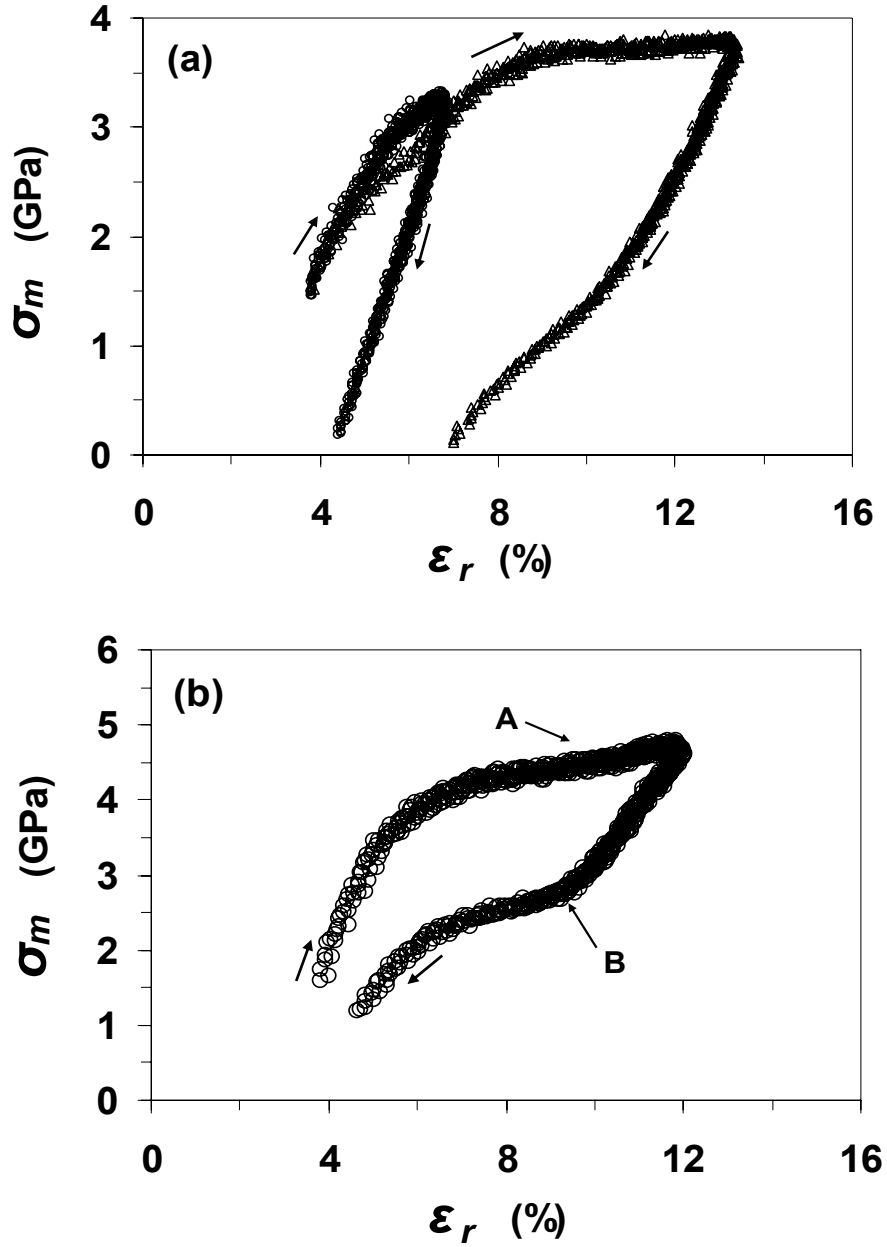


Figure 5.6 Stress-strain responses of single-crystal Cu-Al-Ni alloy at room temperature derived from cyclic nanoindentation results: (a) first-cycle response for a maximum load of 100 and 450  $\mu\text{N}$  revealing changes in the dominant deformation mechanism(s) and (b) stress-strain hysteresis of the stable pseudoelastic behavior obtained after six nanoindentation cycles (training period) for a maximum load of 450  $\mu\text{N}$ . The arrows indicate the loading and unloading paths of each stress-strain cycle.

demonstrated by the first nanoindentation cycle at room temperature can be contrasted with that shown in Figure 5.4. As mentioned earlier, continuous tensile deformation of single-crystal Cu-Al-Ni at  $-30\text{ }^{\circ}\text{C}$  comprised several phase transformations (i.e.,  $\beta_1 \rightarrow \beta'_1 \rightarrow \gamma'_1 \rightarrow \beta''_1$ ). The  $\sigma_m$  versus  $\varepsilon_r$  response shown in Figure 5.6(a) can be used in conjunction with Figure 5.4 to interpret plausible phase transformations due to nanoindentation. For  $\varepsilon_r < 0.08$ , the response resembles that shown in Figure 5.4 for  $\varepsilon < 0.01$  and is attributed to the deformation of the  $\beta_1$  phase. In the range  $0.08 < \varepsilon_r < 0.13$ , the curve levels off and  $\sigma_m$  changes slightly with increasing deformation. This is also similar to the macroscopic behavior encountered at a critical stress resulting in  $\beta_1 \rightarrow \gamma'_1$  transformation (e.g., strain range of 0.01-0.05 in Figure 5.4). It is likely that limited  $\gamma'_1 \rightarrow \beta''_1$  phase transformation also occurred in small regions of high stress gradients adjacent to the contact interface. The unloading curves shown in Figure 5.6(a) reveal differences in both slope and residual strain that may be attributed to variations in the  $\gamma'_1$  and  $\beta''_1$  contents produced by the strain increase. Figure 5.6(a) shows representative  $\sigma_m$  versus  $\varepsilon_r$  curves for a maximum strain of 0.13. Results for  $\varepsilon_r > 0.13$  (not shown here) indicated that the behavior was affected predominantly by plastic deformation, while the effect of phase transformation was secondary. As a consequence, a pseudoelastic behavior was not observed for  $\varepsilon_r > 0.13$ .

The mechanisms affecting the nanoindentation response can be interpreted in terms of the zone-like structure produced under the tip consisting of a plastically deformed zone adjacent to the apex of the tip, a phase transformation zone surrounding the plastic zone, and an outer zone of elastically deformed material [111]. It was found that the nanoindentation cycles leading to stable pseudoelasticity increased with the maximum

strain (load), presumably due to the effect of plastic strain accumulated during the first cycle. Constrained plasticity did not inhibit pseudoelasticity in subsequent indentation cycles provided plastic deformation was localized and, therefore, its effect on the phase transformation mechanisms was negligible.

Figure 5.6(b) shows a stable pseudoelastic response after six nanoindentation cycles for  $L_{\max} = 450 \mu\text{N}$ . In view of the previous results, it is presumed that the material in the tip vicinity consisted mainly of  $\gamma'_1$  martensite. In view of the significant spatial variations of the stresses under the tip, the loading path shown in Figure 5.6(b) is a result of the superimposed effects of elastic deformation of the  $\gamma'_1$  phase and  $\gamma'_1 \rightarrow \beta''_1$  phase transformation, with the contribution of the phase change effect increasing with the increase of the stress. Therefore, it appears that the underlying nanoindentation mechanisms exhibited close similarities with those encountered during loading in the pseudoelastic cycles shown in Figure 5.4. However, the slope increase at point A indicates a change in the local dominant mechanism from  $\gamma'_1 \rightarrow \beta''_1$  phase transformation to deformation of the produced  $\beta''_1$  phase. The reverse phenomenon occurred during unloading to point B. Despite the similar characteristics of the pseudoelastic responses shown in Figure 5.4 and 5.6, significantly higher phase-transformation stresses occurred in the nanoindentation tests. There are several explanations for this difference. First, a compressive stress higher than a tensile stress is required to produce the same strain [112]. It is well known that the phase-transformation stress increases with temperature [113]. Hence, a second reason for the higher stresses in the nanoscale pseudoelastic response is that the nanoindentation experiments were performed at room temperature, whereas the tensile tests were carried out at  $-30 \text{ }^\circ\text{C}$ . A third possible reason for this discrepancy is the

nonuniform distribution of nanoindentation stresses. Large stress gradients in the tip neighborhood resulted in scale-dependent phase transformations. Hence, the stabilization of the  $\gamma'_1$  phase in the nanoindentation experiments required a higher mean stress than that in the tensile tests. Clearly, the stability of the  $\gamma'_1$  phase (attained after the training period) is a precursor for the steady-state pseudoelastic behavior of the Cu-Al-Ni alloy.

## **Chapter 6**

### **Scale-Dependent Nanomechanical Behavior and Anisotropic Friction of Nanotextured Silicon Surfaces**

Basic understanding of nanoscale surface interactions is critical to the reliable operation of many microscopic devices possessing contact interfaces. Continuing trends for device scale-down have increased the importance of surface forces at submicrometer scales. Moreover, because of the very low contact forces and small contact areas, insight into the scale dependence of surface mechanical properties is critical. Surface texturing has been found to be advantageous in various tribological applications. For example, surface texturing of the magnetic storage medium and recording heads has been used to prevent in-plane and out-of-plane head vibrations and provide less lubricant depletion and stable and low coefficient of friction in hard-disk drives [114, 115]. The formation of microscopic dimples by laser surface texturing has been shown to improve the tribological performance of magnetic tape/guide systems [116], reduce friction at piston ring and mechanical seal contact interfaces [117, 118], and prevent stiction in microelectromechanical devices [119]. Advances in nanofabrication techniques and microprobe-based instruments exhibiting high displacement and force sensitivities have provided impetus for nanoengineering surfaces with tailored topographies and properties.

Surface nanotexturing has attracted significant research attention in recent years due to the emergence of technologies where friction control is critical to the component performance and longevity. Analytical and experimental studies were performed to

examine the effect of the ripple wavelength, varied by adjusting the incidence angle and the energy of the ion beam [120], on the electrical conductivity of nanotextured surfaces [121] and the delamination energy of bonded rippled surfaces [122]. Despite progress in surface texturing methods, the effect of nanoscale changes in the surface morphology on the nanomechanical and nanotribological properties of ion-beam textured surfaces has not been investigated, presumably due to the lack of testing devices with sufficient force and displacement resolutions. Therefore, the main objective in this chapter is to elucidate the mechanical and friction behaviors of nanotextured silicon surfaces in the context of nanoindentation and nanoscale friction experiments performed under controlled load and sliding speed conditions.

## **6.1 ION BEAM-ASSISTED SURFACE NANOTEXTURING**

Ion-beam irradiation is a simple technique that enables nanomodification of the surface topography. For example, rippled surfaces with periodic height modulations have been produced by off-normal incidence ion bombardment [121-127] and normal-incidence sputtering [128]. The surface morphology resulting from ion irradiation is controlled by different competing effects, such as surface-curvature-dependent sputtering and diffusion-driven surface smoothening [129]. Therefore, surface nanotexturing is regarded as a self-organizing process [125, 126].

Surface nanotexturing of a Si(100) wafer was accomplished with an Ar<sup>+</sup> ion beam under conditions of 1000 eV ion energy,  $\sim 5 \times 10^{14}$  ions/cm<sup>2</sup>·s flux,  $\sim 1.8 \times 10^{18}$  ions/cm<sup>2</sup> dose, and 60° incidence angle with respect to the surface normal. The topography of the nanotextured surfaces was imaged with an atomic force microscope (AFM) (Dimension

3100, Veeco Instruments) operated in the tapping mode at a driving frequency of  $\sim 211$  kHz and a scan rate of  $\sim 0.83$  Hz.

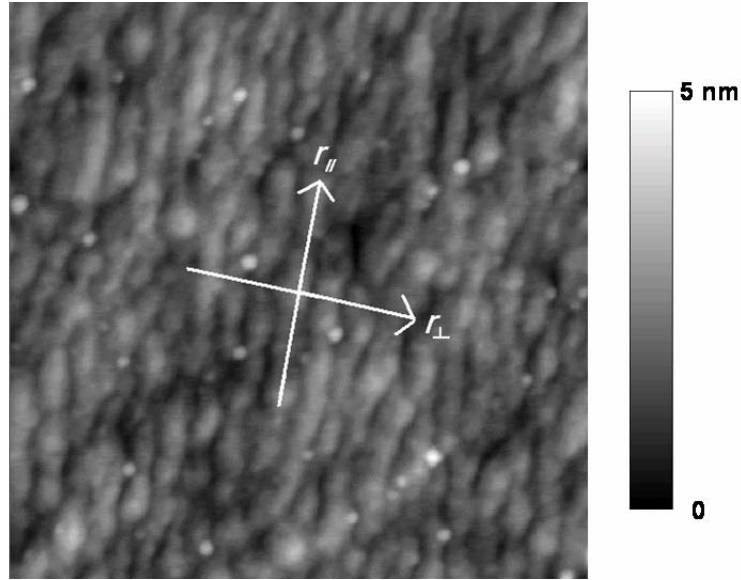


Figure 6.1 AFM image ( $1 \times 1 \mu\text{m}^2$ ) of the topography of a Si(100) surface nanotextured by oblique  $\text{Ar}^+$  ion beam bombardment revealing the formation of dense arrays of periodically ordered ripples.

AFM imaging and roughness calculations revealed that ion beam bombardment produced significant changes in the topography of the silicon surface. The original silicon surface possessed an isotropic topography with a root-mean-square (rms) roughness (determined from  $1 \times 1 \mu\text{m}^2$  AFM images) equal to 0.15 nm. Ion-beam irradiation produced marked changes in the surface morphology. As evidenced from the AFM image shown in Figure 6.1, the topography of the nanotextured surface consists of dense arrays of ordered ripples with an average spacing distance of  $\sim 53$  nm. Arrows labeled by  $r_{\parallel}$  and  $r_{\perp}$  denote directions parallel and perpendicular to the main ripple direction, respectively. The rms roughness calculated from the  $1 \times 1 \mu\text{m}^2$  AFM scan shown in Figure 6.1 is equal to 0.55 nm, which is higher than that of the original surface by a factor greater than 3.5.

Thus, ion-beam irradiation yielded nanoscale roughening characterized by a directional dependence.

## **6.2 SCALE-DEPENDENT NANOMECHANICAL PROPERTIES OF NANOTEXTURED SILICON SURFACES**

Nanoindentation and friction experiments were carried out with the SFM apparatus described in Chapter 2. Conical-spherical diamond tips of nominal radius  $R \approx 1$  and  $20 \mu\text{m}$  were used in the SFM experiments. In the nanoindentation tests, the maximum normal load was varied in the range of  $20\text{--}300 \mu\text{N}$ , while both loading and unloading rates were fixed at  $10 \mu\text{N/s}$ .

Figure 6.2 shows representative nanoindentation responses obtained with relatively sharp ( $R \approx 1 \mu\text{m}$ ) and blunt ( $R \approx 20 \mu\text{m}$ ) diamond tips. Figure 6.2(a) shows the effect of tip radius on the nanoindentation response of the nanotextured surface. For comparison, nanoindentation responses of the original (untextured) silicon surface are shown in Figure 6.2(b), where the relatively blunt tip resulted in nearly fully elastic response, while the sharp tip yielded a force hysteresis upon full unloading, attributed to plastic deformation due to the much higher contact stresses generated by the sharp tip. From the tip contact area at maximum indentation displacement (determined from the tip area function) and the average ripple spacing, the number of contacting ripples for  $R \approx 20$  and  $1 \mu\text{m}$  was found equal to  $\sim 28$  and  $\sim 8$ , respectively. The significant differences in the nanomechanical responses shown in Figure 6.2 are related to surface texturing effects. For  $R \approx 20 \mu\text{m}$ , the nanotextured surface yielded a large force hysteresis, as opposed to the untextured surface that demonstrated elastic behavior. The force hysteresis area represents the energy dissipated to plastically deform mainly the ripples. A small amount

of energy might have also been dissipated as a result of stress-induced phase transformation in the silicon substrate [130-132] and friction losses at tip-ripple interfaces. From the force hysteresis area for  $R \approx 20 \mu\text{m}$ , the total dissipation energy was found equal to  $\sim 1.21 \text{ pJ}$  (i.e.,  $\sim 0.04 \text{ pJ}$  average dissipation energy per contacting ripple). Another difference is that the slope of the loading curve of the nanotextured surface is smaller than that of the untextured surface. This can be attributed to the decrease of the contact area due to nanotexturing that reduced the contact stiffness.

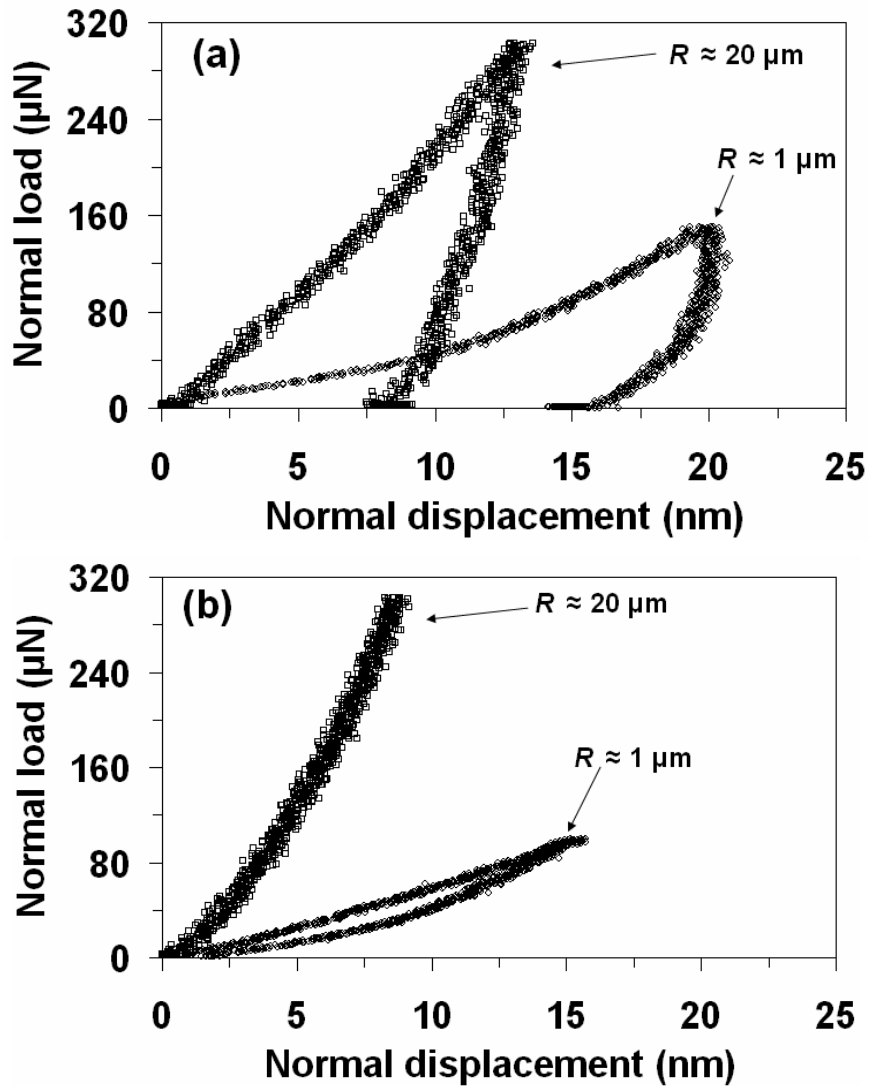


Figure 6.2 Nanoindentation responses of (a) nanotextured and (b) original (untextured) silicon surface for tip radius  $R \approx 1$  and  $20 \mu\text{m}$ .

The nanoindentation curve of the nanotextured surface for  $R \approx 1 \mu\text{m}$  reveals an increase in loading slope for a tip displacement equal to  $\sim 10 \text{ nm}$ , corresponding to  $\sim 5$  ripples in contact with the tip. It is presumed that this slope increase resulted from flattening (most likely irreversible) of these ripples, leading to an increase in the contact area and, in turn, the surface penetration resistance (stiffness). This is supported by the fact that the slope of the loading curve for a tip displacement larger than  $10 \text{ nm}$  is close to that of the untextured surface. The total energy dissipated for  $R \approx 1 \mu\text{m}$  (calculated from the force hysteresis area) was found equal to  $\sim 1.01 \text{ pJ}$ . Hence, for  $\sim 8$  ripples in contact with the tip and maximum tip displacement, the estimated average energy dissipated per ripple is estimated to be equal to  $\sim 0.13 \text{ pJ}$ , which is an order of magnitude higher than that determined from the nanoindentation response for  $R \approx 20 \mu\text{m}$ . The much higher energy dissipation per ripple supports the presumed irreversible flattening of the contacting ripples in the nanoindentation experiment with the sharp tip.

### **6.3 ANISOTROPIC FRICTION BEHAVIOR**

Friction testing was performed under a light normal load  $L$  ( $10$  or  $20 \mu\text{N}$ ) to minimize damage of the nanotextured morphology and a sliding speed of  $0.27 \mu\text{m/s}$ . The friction coefficient was determined as the ratio of the friction force to the applied normal load, known as the engineering coefficient of friction. Each friction test was repeated at least three times, and a friction coefficient was calculated as the average of the mean friction coefficients obtained from these friction tests.

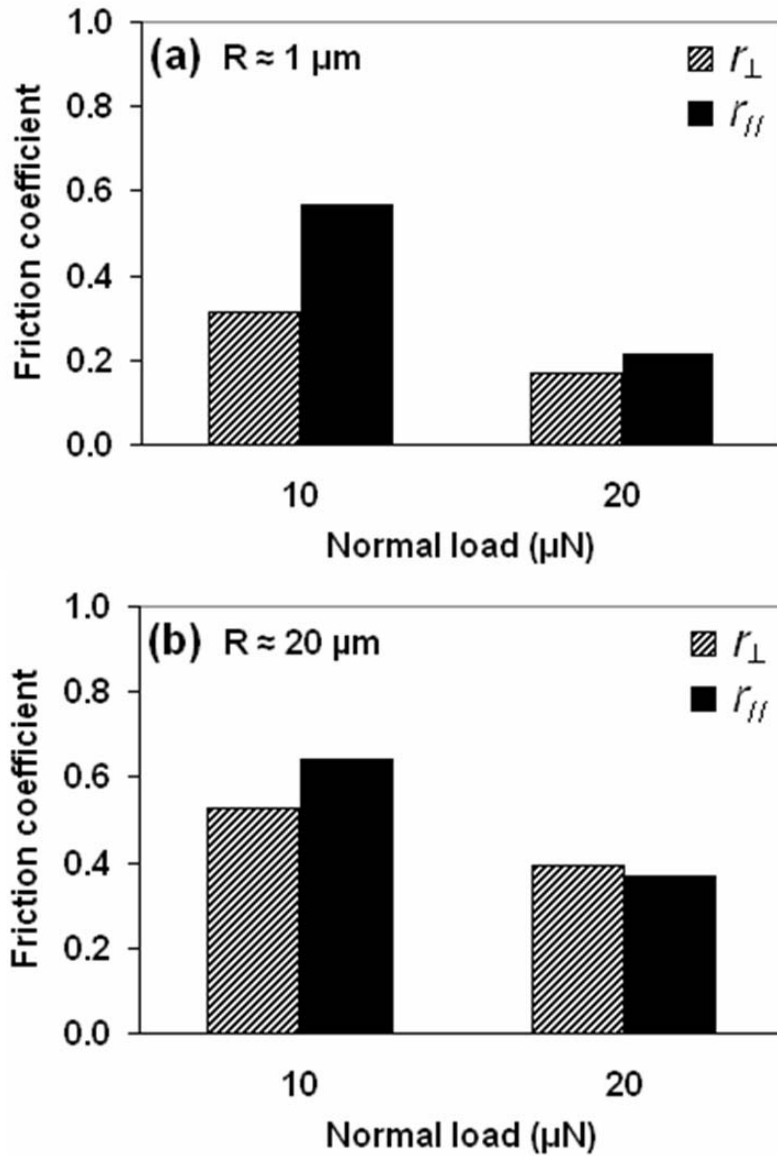


Figure 6.3 Friction coefficient due to sliding of a diamond tip parallel ( $r_{\parallel}$ ) and perpendicular ( $r_{\perp}$ ) to the main ripple direction of a nanotextured silicon surface for tip radius (a)  $R \approx 1 \mu\text{m}$  and (b)  $R \approx 20 \mu\text{m}$ .

Figure 6.3 shows the dependence of the friction coefficient on normal load, tip radius, and tip sliding direction relative to the ripple orientation. For  $R \approx 1 \mu\text{m}$ , the tip penetration depth (determined from nanoindentation) was found to be approximately equal to 3 and 5 nm for  $L = 10$  and  $20 \mu\text{N}$ , respectively, whereas for  $R \approx 20 \mu\text{m}$  it was found to be less than 1 nm for both normal loads. Thus, the ratio of the penetration depth

to the tip radius was less than 0.005 in all of the friction tests, suggesting insignificant contribution of plowing friction to the total friction force. Hence, under the present friction testing conditions, the dominant friction mechanism was adhesion.

The calculation of the friction coefficient based on the engineering definition presumes that the friction coefficient does not depend on the applied normal load. While this is generally true at the macroscale, a nonlinear increase in the friction coefficient is often observed at the microscale with the decrease in the external normal load (pressure) due to increasing contributions from surface adhesion forces to the total normal load [133]. Therefore neglecting the effect of adhesion forces leads to an overestimate of the friction coefficient at the micro-/nanoscale. Thus, the higher friction coefficients obtained in the low-load friction tests may be attributed to the fact that the contribution of adhesion forces to the total normal load was ignored in the friction coefficient calculations. The strong dependence of the friction coefficient on the tip sliding direction for  $L = 10 \mu\text{N}$  provides additional support to the argument that adhesion forces exhibited a significant effect on the magnitude of the friction force under light normal loads. The increase in the friction coefficient with the tip radius demonstrates a scale-dependent friction behavior. Since adhesion was the dominant friction mechanism, the measured friction force was proportional to the contact area. Hence, the lower friction coefficients obtained with the sharp tip can be attributed to smaller contact areas compared to those obtained with the blunt tip for sliding under the same normal load.

Sliding parallel to the main ripple direction resulted in higher friction coefficients for both sharp and blunt tips and  $L = 10 \mu\text{N}$ . The difference between the friction coefficients for sliding parallel and perpendicular to the ripple arrays is more pronounced

for the sharp tip, revealing a scale-dependent anisotropic friction behavior of the nanotextured surface. This frictional anisotropy can be attributed to the significant topography differences in the two orthogonal directions relative to the main ripple orientation (texturing effect) and the friction force dependence on the real contact area, controlled by the external normal load and the tip radius (scale effect). Because more frequent tip-ripple contact separations occurred in the  $r_{\perp}$  direction than in the  $r_{\parallel}$  direction, the real contact area exhibited significant decreases during sliding in the  $r_{\perp}$  direction, which averaged over time imply overall smaller contact area for sliding perpendicular to the ripple arrays. This provides explanation for the anisotropic friction behavior observed under light-load sliding conditions where adhesion was the dominant friction mechanism. This anisotropic friction behavior was not evidenced in the high-load friction tests because the anisotropic topography effect on the friction behavior was secondary due to flattening of the ripples.

## Chapter 7

### Conclusions

A custom-made direct-current FCVA system was presented and its applications in the surface treatment of various materials were studied. Surface characterization and nanomechanical/nanotribological property testing of various materials, including FCVA-treated surfaces, ion-beam textured silicon surface and Cu-Al-Ni shape memory alloy were performed to evaluate the effects of induced surface modifications.

Challenges with FCVA systems, such as arcing spot instabilities and plasma fluctuations, were introduced in Chapter 1. These limitations were overcome with the FCVA system of this study by a special magnetic-field mechanism that stabilized the plasma. This particular magnetic-field mechanism provides a dual effect: it maintains the arc discharge current and also inhibits the migration of the arcing spots on the cathode surface.

The effectiveness of the FCVA system was demonstrated by depositing high-quality amorphous carbon (*a*-C) films, as described in Chapter 2. X-ray diffraction (XRD), Rutherford backscattering spectrometry (RBS), Raman, and X-ray photoelectron spectroscopy (XPS) yielded insight into the bonding structure of the *a*-C films produced by the direct-current arc discharge. The high  $sp^3$  content (>50% without bias and >70% with -100 V average, 25 kHz pulsed bias), high density (3.33 g/cm<sup>3</sup> with -100 V average, 25 kHz pulsed bias and 2.92 g/cm<sup>3</sup> without bias), and high hardness of the deposited *a*-C films illustrate the efficacy of the FCVA system of this study.

Chapter 3 presents results of silicon subjected to different carbon plasma treatments with the present FCVA system. The depth profiles, near-surface chemical composition, carbon atom hybridization, surface roughness, and nanohardness of the synthesized carbon films were determined by Monte Carlo (T-DYN) simulations, X-ray reflectivity (XRR), XPS, atomic force microscopy (AFM), and surface force microscopy (SFM) measurements, respectively. It was found that films with a thickness of only a few nanometers possessed lower  $sp^3$  fractions than much thicker films. The effective hardness was found to depend on the  $sp^3$  fraction and silicon-carbon composition profile. The formation of different carbon atom bonds, film-growth mechanisms, and optimum process conditions for synthesizing ultrathin carbon films were discussed in the context of the obtained T-DYN, XRR, XPS, AFM, and SFM results and interpreted in terms of surface bombardment, adsorption, and diffusion mechanisms.

FCVA surface treatment of cobalt-based magnetic storage medium was presented in Chapter 4. Simulation and experimental results of the carbon-treated surface of the magnetic medium revealed the potential of such treatment to produce overcoat-free media for next-generation disk drives in which the extremely small magnetic spacing precludes the use of a carbon overcoat. Two types of FCVA treatments were performed after the removal of the preexisting carbon overcoat by in-situ  $Ar^+$  ion sputter-etching, namely, one series of carbon treatments with zero substrate bias and another series of carbon treatments with  $-100$  V average substrate bias of 25 kHz frequency. T-DYN simulations and XPS, AFM, and SFM results provided insight into carbon implantation, bonding formation, surface smoothening, residual stress, and nanomechanical characteristics of the surface-treated magnetic storage medium. XPS results indicated that

6-s FCVA-treatment with carbon plasma (i.e.,  $C^+$  ion dose of less than  $0.9 \times 10^{16}$  ions/cm<sup>2</sup>) prevented oxidation of the magnetic medium upon exposure to the ambient. For carbon plasma treatment time of less than 24 s, a higher  $sp^3$  fraction and a thinner modified surface layer of the magnetic medium was obtained for zero than  $-100$  V substrate bias due to shallower ion implantation; however, a smoother surface was obtained with  $-100$  V substrate bias. XPS analysis showed that carbon species did not form chemical compounds in the magnetic medium. SFM experiments yielded a correlation between FCVA treatment conditions and nanomechanical properties of surface-modified magnetic medium.

Phase transformations and the mechanical behavior of a single-crystal Cu-Al-Ni shape memory alloy were examined in Chapter 5. It was shown that this alloy can be trained to exhibit pseudoelastic behavior by cyclic loading up to a certain maximum stress. In view of the similarities of the stress-strain responses obtained from tensile and nanoindentation tests, it was presumed that the training period resulted in the stabilization of the  $\gamma'_1$  martensite phase. Subsequent cyclic loading led to fully reversible martensitic transformations ( $\gamma'_1 \rightarrow \beta''_1$ ). This study also provided insight into the nanoscale pseudoelastic behavior of Cu-Al-Ni. Phase transformation mechanisms were derived from comparisons with known phase transformations occurring under cyclic tensile loading. The intriguing martensite phase transformation and stress-strain response of Cu-Al-Ni are of great importance in the design of microdevices with high dynamic agility. For instance, the prospect of alternating between pseudoelastic responses caused by austenite-martensite and martensite-martensite phase transformations through local

temperature control to achieve nanoscale tuning of the damping ratio is a captivating concept worthy of further investigation.

Finally, nanoscale surface texturing of single-crystal silicon by  $\text{Ar}^+$  ion beam irradiation was examined in Chapter 6. The nanomechanical and nanotribological properties of textured silicon surfaces were studied by the techniques described in previous chapters. AFM imaging revealed that nanoscale texturing by  $\text{Ar}^+$  ion bombardment produces an anisotropic morphology consisting of ordered nanometer-sized ripples. SFM testing demonstrated that the nanotextured surface exhibited scale-dependent nanoindentation behavior, which differed significantly from those of the original (untextured) silicon surface. A strong dependence of the friction coefficient on the tip radius and the sliding direction relative to the ripple orientation was observed in SFM experiments carried out under a light normal load. The experimental trends were interpreted in terms of the applied normal load, tip-ripple interaction scale, ripple orientation, and surface adhesion.

## BIBLIOGRAPHY

- [1] A. Anders, *IEEE Trans. Plasma Sci.* **29**, 393 (2001).
- [2] S. Anders, A. Anders, I. G. Brown, B. Wei, K. Komvopoulos, J. W. Ager III, and K. M. Yu, *Surf. Coat. Technol.* **68-69**, 388 (1994).
- [3] A. Anders, *Surf. Coat. Technol.* **93**, 158 (1997).
- [4] E. Byon and A. Anders, *J. Appl. Phys.* **93**, 1899 (2003).
- [5] A. Anders, *IEEE Trans. Plasma Sci.* **30**, 108 (2002).
- [6] B. Bhushan, *Diamond Relat. Mater.* **8**, 1985 (1999).
- [7] A. Anders and G. Y. Yushkov, *J. Appl. Phys.* **91**, 4824 (2002).
- [8] A. Anders, *Surf. Coat. Technol.* **120-121**, 319 (1999).
- [9] A. Anders and R. A. MacGill, *Surf. Coat. Technol.* **133-134**, 96 (2000).
- [10] G. F. You, B. K. Tay, S. P. Lau, D. H. C. Chua, and W. I. Milne, *Surf. Coat. Technol.* **150**, 50 (2002).
- [11] T. Schülke and A. Anders, *IEEE Trans. Plasma Sci.* **25**, 660 (1997).
- [12] H. Dai, Y. Shen, L. Li, X. Li, X. Cai, and P. K. Chu, *Rev. Sci. Instrum.* **78**, 095103 (2007).
- [13] T. Schuelke, T. Witke, H.-J. Scheibe, P. Siemroth, B. Schultrich, O. Zimmer, and J. Vetter, *Surf. Coat. Technol.* **120-121**, 226 (1999).
- [14] B. Schultrich, P. Siemroth, and H.-J. Scheibe, *Surf. Coat. Technol.* **93**, 64 (1997).
- [15] K. Keutel, H. Fuchs, and C. Edelmann, *Appl. Phys. A* **78**, 687 (2004).
- [16] D. M. Sanders and A. Anders, *Surf. Coat. Technol.* **133-134**, 78 (2000).
- [17] B. F. Coll, P. Sathrum, R. Aharonov, and M. A. Tamor, *Thin Solid Films* **209**, 165 (1992).
- [18] A. Anders, *Surf. Coat. Technol.* **183**, 301 (2004).
- [19] G. M. Pharr, D. L. Callahan, S. D. McAdams, T. Y. Tsui, S. Anders, A. Anders, J. W. Ager III, I. G. Brown, C. S. Bhatia, S. R. P. Silva, and J. Robertson, *Appl. Phys. Lett.* **68**, 779 (1996).
- [20] W. Lu, K. Komvopoulos, and S. W. Yeh, *J. Appl. Phys.* **89**, 2422 (2001).
- [21] P. C. Kelires, M. Gioti, and S. Logothetidis, *Phys. Rev. B* **59**, 5074 (1999).
- [22] D. Wan and K. Komvopoulos, *J. Appl. Phys.* **100**, 063307 (2006).
- [23] D. Wan and K. Komvopoulos, *Appl. Phys. Lett.* **88**, 221908 (2006).
- [24] D. Wan and K. Komvopoulos, *J. Phys. Chem. C* **111**, 9891 (2007).
- [25] Y. Lifshitz, S. R. Kasi, J. W. Rabalais, and W. Eckstein, *Phys. Rev. B* **41**, 10468 (1990).
- [26] Y. Lifshitz, C. D. Roux, K. Boyd, W. Eckstein, and J. W. Rabalais, *Nucl. Instrum. Methods Phys. Res. B* **83**, 351 (1993).
- [27] Y. Lifshitz, G. D. Lempert, and E. Grossman, *Phys. Rev. Lett.* **72**, 2753 (1994).
- [28] R. G. Lacerda, P. Hammer, C. M. Lepienski, F. Alvarez, and F. C. Marques, *J. Vac. Sci. Technol. A* **19**, 971 (2001).
- [29] S. Aisenberg and R. Chabot, *J. Appl. Phys.* **42**, 2953 (1971).
- [30] J. Ishikawa, Y. Takeiri, K. Ogawa and T. Takagi, *J. Appl. Phys.* **61**, 2509 (1987).
- [31] P. Kovarik, E. B. D. Bourdon and R. H. Prince, *Phys. Rev. B* **48**, 12123 (1993).
- [32] B. Petereit, P. Siemroth, H.-H. Schneider, and H. Hilgers, *Surf. Coat. Technol.* **174-175**, 648 (2003).

- [33] D. Liu, G. Benstetter, E. Lodermeier, X. Chen, J. Ding, Y. Liu, J. Zhang, and T. Ma, *Diamond Relat. Mater.* **12**, 1594 (2003).
- [34] J. Robertson, *Mater. Sci. Eng., R.* **37**, 129 (2002).
- [35] J. Robertson, *Thin Solid Films* **383**, 81 (2001).
- [36] B. Schultrich, H.-J. Scheibe, D. Drescher, and H. Ziegele, *Surf. Coat. Technol.* **98**, 1097 (1998).
- [37] H. Han, F. Ryan, and M. McClure, *Surf. Coat. Technol.* **120-121**, 579 (1999).
- [38] P. R. Goglia, J. Berkowitz, J. Hoehn, A. Xidis, and L. Stover, *Diamond Relat. Mater.* **10**, 271 (2001).
- [39] T. A. Friedmann, J. P. Sullivan, J. A. Knapp, D. R. Tallant, D. M. Follstaedt, D. L. Medlin, and P. B. Mirkarimi, *Appl. Phys. Lett.* **71**, 3820 (1997).
- [40] V. S. Veerasamy, G. A. J. Amaratunga, W. I. Milne, J. Robertson, and P. J. Fallon, *J. Non-Crys. Solids* **164-166**, 1111 (1993).
- [41] B. K. Tay, X. Shi, H. S. Tan, H. S. Yang, and Z. Sun, *Surf. Coat. Technol.* **105**, 155 (1998).
- [42] Z. Feng, S. Anders, A. Anders, J. W. Ager III, I. G. Brown, K. Komvopoulos, and D. B. Bogy, *Diamond Relat. Mater.* **5**, 1080 (1996).
- [43] A. C. Ferrari, A. Libassi, B. K. Tanner, V. Stolojan, J. Yuan, L. M. Brown, S. E. Rodil, B. Kleinsorge, and J. Robertson, *Phys. Rev. B* **62**, 11089 (2000).
- [44] M. Yoshikawa, G. Katagiri, H. Ishida, A. Ishitani, and T. Akamatsu, *J. Appl. Phys.* **64**, 6464 (1988).
- [45] M. A. Tamor and W. C. Vassell, *J. Appl. Phys.* **76**, 3823 (1994).
- [46] D. A. Shirley, *Phys. Rev. B* **5**, 4709 (1972).
- [47] S. T. Jackson and R. G. Nuzzo, *Appl. Surf. Sci.* **90**, 195 (1995).
- [48] J. Diaz, G. Paolicelli, S. Ferrer, and F. Comin, *Phys. Rev. B* **54**, 8064 (1996).
- [49] W. Lu and K. Komvopoulos, *J. Tribol.* **123**, 641 (2001).
- [50] W. Lu, K. Komvopoulos, P. Patsalas, C. Charitidis, M. Gioti, and S. Logothetidis, *Surf. Coat. Technol.* **168**, 12 (2003).
- [51] L. Kogut and K. Komvopoulos, *J. Mater. Res.* **19**, 3641 (2004).
- [52] K.-H. Müller, *Surf. Sci.* **184**, L375 (1987).
- [53] M. T. Robinson and I. M. Torrens, *Phys. Rev. B* **9**, 5008 (1974).
- [54] O. S. Oen, D. K. Holmes, and M. T. Robinson, *J. Appl. Phys.* **34**, 302 (1963).
- [55] M. T. Robinson and O. S. Oen, *Phys. Rev.* **132**, 2385 (1963).
- [56] W. D. Wilson, L. G. Haggmark, and J. P. Biersack, *Phys. Rev. B* **15**, 2458 (1977).
- [57] J. Lindhard and M. Scharff, *Phys. Rev.* **124**, 128 (1961).
- [58] J. P. Biersack and W. Eckstein, *Appl. Phys. A* **34**, 73 (1984).
- [59] W. Möller and W. Eckstein, *Nucl. Instrum. Methods Phys. Res. B* **2**, 814 (1984).
- [60] O. Vancauwenberghe, N. Herbots, and O. C. Hellman, *J. Vac. Sci. Technol. B* **9**, 2027 (1991).
- [61] J. Biersack, *Nucl. Instrum. Methods Phys. Res. B* **153**, 398 (1999).
- [62] R. Kosiba and G. Ecke, *Nucl. Instrum. Methods Phys. Res. B* **187**, 36 (2002).
- [63] G. Ecke, R. Kosiba, V. Kharlamov, Y. Trushin, and J. Pezoldt, *Nucl. Instrum. Methods Phys. Res. B* **196**, 39 (2002).
- [64] R. M. Hausner, H. Baumann, and K. Bethge, *Nucl. Instrum. Methods Phys. Res. B* **113**, 176 (1996).
- [65] M. F. Toney and S. Brennan, *J. Appl. Phys.* **66**, 1861 (1989).

- [66] F. Bridou and B. Pardo, *J. X-ray Sci. Technol.* **4**, 200 (1994).
- [67] F. Bridou, J. Gautier, F. Delmotte, M.-F. Ravet, O. Durand, and M. Modreanu, *Appl. Surf. Sci.* **253**, 12 (2006).
- [68] D. R. McKenzie, D. Muller and B. A. Pailthorpe, *Phys. Rev. Lett.* **67**, 773 (1991).
- [69] J. Schwan, S. Ulrich, T. Theel, H. Roth, H. Ehrhardt, P. Becker, and S. R. P. Silva, *J. Appl. Phys.* **82**, 6024 (1997).
- [70] C. A. Davis, K. M. Knowles, and G. A. J. Amaratunga, *Surf. Coat. Technol.* **76-77**, 316 (1995).
- [71] W. Jiang, Y. Zhang, M. H. Engelhard, W. J. Weber, G. J. Exarhos, J Lian, and R. C. Ewing, *J. Appl. Phys.* **101**, 023524 (2007).
- [72] T. N. Taylor, *J. Mater. Res.* **4**, 189 (1989).
- [73] A. Mahmood, S. Muhl, R. Machorro, A. Lousa, J. Esteve, and J. Heiras, *Diamond Relat. Mater.* **15**, 71 (2006).
- [74] D. Liu, G. Benstetter, and E. Lodermeier, *Thin Solid Films* **436**, 244 (2003).
- [75] D. Wan and K. Komvopoulos, *J. Mater. Res.* **19**, 2131 (2004).
- [76] J. Gao, E. Liu, D. L. Butler, and A. Zeng, *Surf. Coat. Technol.*, **176**, 93 (2003).
- [77] P. Bernhard, Ch. Ziethen, R. Ohr, H. Hilfers, and G. Schönhense, *Surf. Coat. Technol.*, **180-181**, 621 (2004).
- [78] A. C. Ferrari, *Surf. Coat. Technol.*, **180-181**, 190 (2004).
- [79] T. Yamamoto and H. Hyodo, *Tribol. Inter.* **36**, 483 (2003).
- [80] P. J. Fallon, V. S. Veerasamy, C. A. Davis, J. Robertson, G. A. J. Amaratunga, W. I. Milne, and J. Koskinen, *Phys. Rev. B*, **48**, 4777 (1993).
- [81] K. S. Kim, *Phy. Rev. B*, **11**, 2177 (1975).
- [82] M. Fremond and S. Miyazaki: *Shape Memory Alloys* (Springer, New York, 1996).
- [83] H. Funakubo: *Shape Memory Alloys*, translated from the Japanese by J. B. Kennedy (Gordon and Breach Science Publishers, New York, 1987).
- [84] K. Otsuka, H. Sakamoto, and K. Shimizu, *Acta Metall.* **27**, 585 (1979).
- [85] K. Otsuka and C.M. Wayman: *Shape Memory Materials* (Cambridge University Press, Cambridge, 1998).
- [86] K. Otsuka, H. Sakamoto, and K. Shimizu, *Scri. Metall.* **10**, 983 (1976).
- [87] Y. Liu, Z. L. Xie, J. Van Humbeeck, and L. Delaey, *Acta Mater.* **47**, 645 (1999).
- [88] H. Sehitoglu, J. Jun, X. Zhang, I. Karaman, Y. Chumlyakov, H. J. Maier, and K. Gall, *Acta Mater.* **49**, 3609 (2001).
- [89] H. Sehitoglu, I. Karaman, R. Anderson, X. Zhang, K. Gall, H. J. Maier, and Y. Chumlyakov, *Acta Mater.* **48**, 3311 (2000).
- [90] W. Huang, *Mater. Des.* **23**, 11 (2002).
- [91] P. Šittner, K. Hashimoto, M. Kato, and M. Tokuda, *Scri. Mater.* **48**, 1153 (2003).
- [92] X. Zhang, Q. Sun, and S. Yu, *J. Mech. Phys. Solids* **48**, 2163 (2000).
- [93] P. Sittner, V. Novák, and N. Zárubová, *Int. J. Mech. Sci.* **40**, 159 (1998).
- [94] P. Šittner and V. Novák, *Int. J. Plast.* **16**, 1243 (2000).
- [95] K. Otsuka, H. Sakamoto, and K. Shimizu, *Scri. Metall.* **9**, 491 (1975).
- [96] V. Novák, J. Malimánek, and N. Zárubová, *Mater. Sci. Eng. A* **191**, 193 (1995).
- [97] N. Zárubová, A. Gemperle, and V. Novák, *Mater. Sci. Eng. A* **222**, 166 (1997).
- [98] R. Gastien, C.E. Corbellani, M. Sade, and F.C. Lovey, *Scri. Mater.* **50**, 1103 (2004).
- [99] M. J. Duggin and W. A. Rachinger, *Acta Metall.* **12**, 529 (1964).
- [100] P. Brezina, *Int. Metals Rev.* **27**, 77 (1982).

- [101] C. H. Chen and T. F. Liu, *Mater. Chem. Phys.* **78**, 464 (2002).
- [102] J. Tan and T. F. Liu, *Scri. Mater.* **43**, 1083 (2000).
- [103] C. H. Chen and T. F. Liu, *Scri. Mater.* **47**, 515 (2002).
- [104] L.E. Tanner, A.R. Pelton, and R. Gronsky, *Journal De Physique*, Colloque C4, supplément n12, **43**, 169 (1982).
- [105] V. Pelosin, M. Gerland, G. Covarel, and A. Rivière, *Eur. Phys. J. App. Phys.* **16**, 175 (2001).
- [106] K. Gall, H. Sehitoglu, Y. I. Chumlyakov, and I. V. Kireeva, *Acta Mater.* **47**, 1203 (1999).
- [107] C. Picornell, J. Pons, and E. Cesari, *Acta Mater.* **49**, 4221 (2001).
- [108] X.-G. Ma and K. Komvopoulos, *Appl. Phys. Lett.* **83**, 3773 (2003).
- [109] J. Thurn and R. F. Cook, *J. Mater. Res.* **17**, 1143 (2002).
- [110] K. L. Johnson, *Contact Mechanics* (Cambridge University Press, Cambridge, UK, 1985).
- [111] G. A. Shaw, D. S. Stone, A. D. Johnson, A. B. Ellis, and W. C. Crone, *Appl. Phys. Lett.* **83**, 257 (2003).
- [112] Y. Liu, Z. Xie, and J. Van Humbeeck, *Mater. Sci. Eng. A* **273-275**, 673 (1999).
- [113] T. W. Duerig, K. N. Melton, D. Stöckel, and C. M. Wayman: *Engineering Aspects of Shape Memory Alloys* (Butterworth-Heinemann, London, 1990).
- [114] L. Zhou, K. Kato, G. Vurens, and F. E. Talke, *Tribol. Int.*, **36**, 269 (2003).
- [115] R. Ranjan., D. N. Lambeth, M. Tromel, P. Goglia, and Y. Li, 1991, *J. Appl. Phys.*, **69**, 5745 (1991).
- [116] B. Raeymaekers, I. Etsion, and F. E. Talke, *Tribol. Lett.*, **27**, 89 (2007).
- [117] Y. Kligerman, I. Etsion, and A. Shinkarenko, *ASME J. Tribol.*, **127**, 632 (2005).
- [118] I. Etsion, 2004, *Tribol. Lett.*, **17**, 733 (2004).
- [119] K. Komvopoulos, *J. Adhes. Sci. Technol.*, **17**, 477 (2003).
- [120] H. Zhou, Y. Wang, L. Zhou, R. L. Headrick, A. S. Özcan, Y. Wang, G. Özeydin, K. F. Ludwig Jr., and D. P. Siddons, *Phys. Rev. B*, **75**, 155416 (2007).
- [121] P. Mishra, P. Karmakar, and D. Ghose, *Nucl. Instr. Meth. Phys. Res. B*, **243**, 16 (2006).
- [122] Z. X. Liu and N. W. Cheung, *Mater. Res. Soc. Symp. Proc.*, **768**, G2.8.1 (2003).
- [123] J. J. Vajo, R. E. Doty, and E.-H. Cirlin, *J. Vac. Sci. Technol. A*, **14**, 2709 (1996).
- [124] P. F. A. Alkemade, and Z. X. Jiang, *J. Vac. Sci. Technol. B*, **19**, 1699 (2001).
- [125] H. X. Qian, W. Zhou, Y. Q. Fu, B. K. A. Ngoi, and G. C. Lim, *Appl. Surf. Sci.*, **240**, 140 (2005).
- [126] K. Oyoshi, S. Hishita, K. Wada, S. Suehara, and T. Aizawa, *Appl. Surf. Sci.*, **100-101**, 374 (1996).
- [127] P. Karmakar and D. Ghose, *Nucl. Instr. Meth. Phys. Res. B*, **230**, 539 (2005).
- [128] G. Costantini, S. Rusponi, F. Buatier de Mongeot, C. Boragno, and U. Valbusa, *J. Phys.: Condens. Matter.*, **13**, 5875 (2001).
- [129] R. M. Bradley and J. M. E. Harper, *J. Vac. Sci. Technol. A*, **6**, 2390 (1988).
- [130] G. M. Pharr, W. C. Oliver, and D. R. Clarke, *Scrip. Metal.*, **23**, 1949 (1989).
- [131] G. M. Pharr, W. C. Oliver, and D. S. Harding, *J. Mater. Res.*, **6**, 1129 (1991).
- [132] M. C. Gupta and A. L. Ruoff, *J. Appl. Phys.*, **51**, 1072 (1980).
- [133] S. J. Timpe and K. Komvopoulos, *J. Microelectromech. Sys.*, **15**, 1612 (2006).